A STUDY ON HOT TEARING IN DIRECT CHILL CASTING OF ALUMINUM ALLOYS USING A MULTI-SCALE APPROACH

BY

NILOUFAR KHODAEI, B.Sc.

A THESIS

SUBMITTED TO THE DEPARTMENT OF MATERIALS SCIENCE AND ENGINEERING

AND THE SCHOOL OF GRADUATE STUDIES

OF MCMASTER UNIVERSITY

IN PARTIAL FULFILMENT OF THE REQUIREMENTS

FOR THE DEGREE OF

MASTER OF APPLIED SCIENCE

© Copyright by Niloufar Khodaei, April 2020

All Rights Reserved

Master of Applied Science — McMaster University

(Materials Science and Engineering) — Hamilton, Ontario, Canada

TITLE: A Study on Hot Tearing in Direct Chill Casting of Aluminum Alloys Using A Multi-scale Approach

AUTHOR: Niloufar Khodaei, B.Sc.

SUPERVISOR: Dr. André Phillion

NUMBER OF PAGES: xxii, 120

Abstract

Hot tearing is one of the most severe defects encountered in direct chill (DC) casting of aluminum alloys and is intimately linked with the constitutive behavior of the alloy in the semi-solid region. The experimental studies in this field are limited due to the high temperature at which hot tears form and the sensitivity of factors that cause hot tearing to the casting geometry; thus, modeling of the DC casting process at the macroscopic scale has become a popular practice in industry. However, such models do not consider the localization of deformation and liquid feeding between the grains that cause cracking. In this study, a new multi-scale approach to predicting the hot tearing defect in DC casting is proposed. In this approach, a thermomechanical model of the DC casting process [1] has been coupled with a meso-scale coupled hydro-mechanical granular model [2]. The thermomechanical model predicts the evolution of temperature distribution and displacement field for all locations within the DC cast billet for three different simulation cases with casting speeds of 46 mm.min^{-1}, 56 mm.min^{-1}, and 66 mm.min^{-1}. Then, its output is used as input to the coupled meso-scale hydro-mechanical granular model to investigate the effect of different parameters on the tensile behavior of the mushy zone. The results show that the multi-scale approach can successfully simulate hot tearing formation at the regions in the DC cast billet which were found to be susceptible to hot tearing. Moreover, hot tearing

susceptibility maps generated by this approach reveal that for the three DC casting simulations performed, the condition for hot tearing formation is favorable above the bottom block and near the centerline of the billet and as the casting speed increases, this region shifts to lower heights in the billet and a greater region becomes prone to hot tearing.

To the loving memory of my grandmothers

To my adorable parents for their endless support

To my lovely brother

Acknowledgements

I would like to express my unlimited gratitude to a number of people who supported me to accomplish this work. First and foremost, I have to thank my supervisor, Dr. André Philion, for his endless support and kind attitude. My gratitude also goes to all faculty and staff members of the department of Materials Science and Engineering at McMaster University for their incredible support and kindness. I would like to especially acknowledge Mary-Anne Bechamp, graduate administrator of our department, for her positive energy, supportive attitude, and caring disposition during the past two years. Additionally, I would like to extend my gratitude to my fellow colleagues in our friendly research group, SIM3P, for their support and the productive time and discussions we have shared. I wish all of them success in their future endeavors. I am particularly grateful to Natural Sciences and Engineering Research Council of Canada for the financial support of this study. I would like to thank Amir Arsalan Jameei and Roham Akbarian for the encouragement and help they have tirelessly given. Last but not least, my wholehearted gratitude goes to my lovely parents and kind brother for their unconditional support. Non of this would have been possible without their support and words cannot express my gratefulness toward them.

Contents

Abstract **iii**

Acknowledgements **vi**

List of Symbols **xvii**

1 Introduction **1**

1.1 Aluminum Alloys 1

1.2 Direct Chill Casting of Aluminum Alloys 3

1.3 Solidification Defects in DC Casting 6

1.4 Simulation of DC Casting Process 8

2 Literature Review **10**

2.1 Hot Tearing 10

2.2 Hot Tearing Mechanism 13

2.3 Hot Tearing in DC Casting 16

2.3.1 Parameter Sensitivity 17

2.3.1.1 Alloy Parameters 17

2.3.1.2 Processing Parameter 19

2.4 Hot Tearing Criteria 20
2.4.1 Nonmechanical Criteria 20
2.4.2 Mechanical Criteria 23
2.4.3 Combined Criteria 25
2.5 Multi-physics Models 32
2.6 Thermomechanical Modeling of the DC Casting Process 35
2.7 Summary 38

3 Scope and Objectives **40**

4 Numerical Methods **42**
4.1 Introduction 42
4.2 The Macro-scale Model 43
4.2.1 Boundary Conditions 44
4.2.2 Materials Data 46
4.2.3 Constitutive Models 48
4.3 The Meso-scale Model 53
4.3.1 Solidification Segment 54
4.3.2 Fluid Flow Segment 56
4.3.3 Semi-solid Deformation Segment 57
4.3.4 Failure Segment 58
4.3.5 Hydro-mechanical Coupling 60
4.4 Multi-scale Approach to Hot Tearing 61
4.4.1 Application of The Pore Fraction Model 63
4.4.2 Application of The Meso-scale Model 66

4.5 Summary 67

5 Results and Discussion **69**

5.1 Introduction 69

5.2 Macro-scale Model 69

5.3 The Meso-scale Model 75

5.4 Multi-scale Approach 80

5.4.1 Pore Fraction Model 80

5.4.2 Characteristics of Susceptible Locations 85

5.4.3 Application to Meso-scale Model 90

5.4.4 Hot Tearing Susceptibility Map 96

5.5 Summary 97

6 Conclusion and Perspectives **99**

Appendix **109**

List of Figures

1.1 Simple layout of a typical vertical direct chill casting setup [8]. 4

1.2 A schematic of aluminum billet DC casting process. 5

2.1 Examples of hot tearing in aluminum alloys; (a) extruded billet, (b) rectangular ingot [25, 26]. 11

2.2 Schematic of the semi-solid region showing factors affecting hot tearing [30]. 12

2.3 Schematic of typical microstructure correspond to four stages of solidification: (a) mass feeding, (b) interdendritic feeding, (c) interdendritic separation, and (d) interdendritic bridging [32]. 13

2.4 Schematic representation of (a) a binary phase diagram with a eutectic point, and (b) the corresponding hot tearing tendency curve as a function of alloy composition [50]. 18

2.5 Schematic representation of the relative position of elongation to failure (ε_p) and linear shrinkage (ε_{sh}) in the brittle temperature range [59]. . 25

2.6 Schematic showing the variation of liquid pressure as a function of distance from the root of the dendrites and localization of straining at the roots in a columnar dendritic structure [60]. 26

2.7 Schematic representation of a small volume element on which the mass balance equation is performed [60]. 27
2.8 Predicted shrinkage and deformation pore fraction in Al-3wt.%Cu alloys (a) as a function of the dimensionless Niyama criterion with an applied strain rate of 10^{-3} s^{-1}, and (b) as a function of strain rate with a Niyama criterion value of 100 K $s^{0.5}m^{-1}$ [62]. 31
2.9 Schematic of the 2-D semi-solid structure with regular arrangement of grains and the tensile deformation of the semi-solid medium as a result of a constant applied strain rate with different strain values [67]. . . . 33
2.10 Schematic of a 2-D mushy zone at $g_s = 0.92$ subjected to a strain rate of 0.004 s^{-1} [68]. 34
2.11 Evolution in the semi-solid microstructure during tensile deformation of a notched Al-2wt.%Cu specimen as predicted by GMS-3D at (a) $t = 405$ s, (b) $t = 729$ s, and (c) $t = 1215$ s after the start of the simulation [70]. 35
2.12 X-ray tomography of the cross-section showing the evolution in the semi-solid microstructure during the tensile deformation of a notched Al-2wt.%Cu after (a) $t = 486$ s, (b) $t = 729$ s, and (c) $t = 1215$ s from the beginning of the experiment [71]. 35
2.13 Hot cracking susceptibility in the vertical cross-section of an Al-4.5wt% Cu billet computed using different hot tearing criteria for a varying casting speed [73]. 38
4.1 Schematic of (a) the actual DC cast billet and (b) the computational domain in the macro-scale model. 44

4.2 Solidification path of AA5182 used in the macro-scale model [78]. . . 46
4.3 Schematic of semi-solid stress-strain response used in the simulation at various solid fractions for the grain size of 150 μm, and strain rate of 10^{-3} s^{-1}. 51
4.4 Schematic of semi-solid stress-strain response used in the simulation for various grain sizes at solid fraction of 0.98 and strain rate of 10^{-3} s^{-1}. 52
4.5 A breakdown of the RVE representing solid-liquid geometry in 3-D; (a) the entire model domain, (b) a polyhedral grain, (c) a pyramid volume element, and (d) a single tetrahedral element showing both the solid portion (gray) and liquid portion (clear) [84]. 55
4.6 (a) The domain of the granular semi-solid model containing 27 ($3 \times 3 \times 3$) grains, (b) the network of the triangular liquid elements in between the polyhedral grains, and (c) a schematic of the liquid control volume and its location in relation to the facets of two neighboring grains. . . 57
4.7 Schematic representation of crack initiation in the liquid channel located in between two solid grains. 59
4.8 Flow chart of the multi-scale approach. 62
4.9 Schematic of a DC cast billet and a 2-D domain of the semi-solid region. 65
4.10 Schematic of a representative volume element (RVE) at solid fraction of 0.98. 66
5.1 Location of points a, b, and c within the DC cast billet. 70
5.2 Evolution of temperature with time at three different locations in the billet shown in Fig. 5.1 for case A. 72

5.3 Evolution of hoop stress as a function of time at three different locations shown in 5.1 for case A. 73
5.4 Evolution of temperature with time along the surface of the billet at different heights for case A. 73
5.5 Evolution of temperature with time along the centerline of the billet at different heights for case A. 74
5.6 Contour plots representing (a) grain size, (b) temperature, and (c) the hoop stress at the end of the simulation for case A. 75
5.7 Cross-section of the representative volume element (RVE) generated by the solidification segment of the meso-scale model at three solid fractions of (a) 0.5, (b) 0.7, and (c) 0.9. 76
5.8 Variation of permeability of the mushy zone with solid fraction for three different grain sizes of 100 μm, 200 μm and 300 μm. 77
5.9 Contour plots of the liquid pressure drop for an RVE with 7 grains per side at solid fractions of (a) 0.5, (b) 0.7, and (c) 0.9. 78
5.10 Average stress-strain behavior of the RVE subjected to a strain rate of 0.001 s^{-1} for different solid fractions of 0.94, 0.96, 0.98 79
5.11 Evolution of the deformation pore fraction along the centerline of the billet at solid fraction of 0.98 for the macro-scale simulation cases A, B, and C. 82
5.12 Evolution of the strain rate parallel with the thermal gradient ($\dot{\varepsilon}_{px}$) along the centerline of the billet at solid fraction of 0.98 for the macro-scale simulation cases A, B, and C. 83

5.13 Evolution of the strain rate perpendicular to the thermal gradient ($\dot{\varepsilon}_{py}$) along the centerline of the billet at solid fraction of 0.98 for the macro-scale simulation cases A, B, and C. 84
5.14 Variation in the strain perpendicular to the thermal gradient as a function of distance from the bottom block along the centerline of the billet at solid fraction of 0.98 for the macro-scale simulation cases A, B, and C. 84
5.15 Evolution of the deformation pore fraction as a function of distance from the centerline of the billet at solid fraction of 0.98 for the macro-scale simulation cases A, B, and C. 85
5.16 Evolution of grain size in radial direction at solid fraction of 0.98 for the macro-scale simulation cases A, B, and C at the heights specified in Table 5.2. 87
5.17 Evolution of bulk strain rate in radial direction at solid fraction of 0.98 for the macro-scale simulation cases A, B, and C at the heights specified in Table 5.2. 87
5.18 Variation in feeding coefficient with solid fraction for thermal gradients of 2500 K.m^{-1}, 3500 K.m^{-1}, 5500 K.m^{-1} and a constant grain size of 220 μm. 89
5.19 Evolution of thermal gradient in radial direction at solid fraction of 0.98 for the macro-scale simulation cases A, B, and C at the heights specified in Table 5.2. 89
5.20 Simulated (a) stress-strain curves and (b) pressure-strain curves of the RVE with liquid feeding for simulation cases X, Y, and Z. 91

5.21 Simulated stress-strain and stress-pressure curves for simulation case Y. 92
5.22 Contour maps of maximum principal strain for three strain values defined in Fig. 5.21 corresponding to case Y. 93
5.23 Simulated stress-strain behavior of the RVE for various feeding coefficients and bulk strain rates. 94
5.24 Contour map of stress at fracture as a function of bulk strain rate and grain size for a constant feeding coefficient of 0.007 μm.Pa^{-1}.s^{-1}. . . . 95
5.25 Hot tearing susceptibility map for simulation cases a) A with casting speed of 66 mm.min^{-1}, b) B with casting speed of 56 mm.min^{-1}, and c) C with casting speed of 46 mm.min^{-1}. 96
C.1 Schematic of a DC cast billet and a 2-D domain of the semi-solid region. 105

List of Tables

1.2 The standard designation for cast aluminum alloys [3] 2

1.3 The standard designation for wrought aluminum alloys [3] 3

4.1 Thermophysical properties of AA5182 alloy used in the macro-scale model [79] 47

4.2 Mechanical properties of AA5182 used in the macro-scale model [79] . 48

4.3 Parameters of the modified Ludwik equation [80] 49

4.4 Data for calculating Q [83] 51

4.5 List of parameters used in the calculations of the meso-scale model [74] 61

5.1 List of the macro-scale simulation cases 70

5.2 Locations within the billet for which the semi-solid geometries are generated, x is the distance from the centerline and y is the distance from the bottom block. 86

5.3 Characteristics of nodes demonstrating the highest deformation pore fraction at solid fraction of 0.98 88

List of Symbols

Latin Symbols

A	Strain rate in the local coordinate
C_l	Liquid composition
C_s	Solid composition
c	Tortuosity constant
$c_{0,i}$	Composition of element i
D_s	Diffusion coefficient
d	Grain size
E	Young's modulus
f_l	Feeding coefficient
$f_{p,de,\varepsilon x}$	Fraction of porosity associated with deformation parallel with thermal gradient
$f_{p,de,\varepsilon y}$	Fraction of porosity associated with deformation perpendicular to thermal gradient
$f_{p,sh}$	Fraction of porosity associated with shrinkage
G	Temperature gradient
g	Gravitational constant

g_l	Volume fraction of liquid
g_s	Volume fraction of solid
$g_{l,cr}$	Critical liquid fraction
$g_{p,sh}$	Fraction of porosity associated with shrinkage
$g_{p,d}$	Fraction of porosity associated with deformation
h	Distance to the melt surface,Heat transfer coefficient
h_t	Thickness of the liquid channel
$I_{sh(g_{l,cr})}$	Shrinkage related term
$I_d(g_{l,cr})$	Deformation related term.
K	Material's constant, Permeability of the mushy zone
k_i	Binary partition coefficient of element i
K_l	Bulk module of the liquid
L	Length of semi-solid network
L_x, L_y, L_z	Length of the RVE along the x, y, and z directions
m	Stratin rate sensitivity coefficient
m_i	Liquidus gradient of element i
N_y^*	Dimensionless Niyama criterion
n	Strain hardening coefficient
n_{ss}	Strain hardening parameter
P_0	Atmospheric pressure
P_m	Metallostatic pressure
P_s	Effective feeding pressure
P_c	Capillary pressure
p_r	Reserve of plasticity

Q	Growth restriction factor
q	Heat flux
q_l	Microscopic flux
R	Transformation matrix
R'	Transpose matrix of R
S	Area between the ε_{fr} and ε_{sh}
S_v^{sl}	Intrinsic specific solid-liquid interfacial area
T	Temperature
T_{coal}	Mechanical coalescence temperature
T_l	Liquidus temperature
T_s	Solidus temperature
T_∞	Ambient temperature
Tol	Tolerance value
$\dot{T}$	Cooling rate
t	Time
t_R	Relaxation time
t_V	Vulnerable time interval
V	Volume element of the mushy zone
V_{lx}	Fluid velocity parallel to thermal gradient
V_{ly}	Fluid velocity perpendicular to thermal gradient
V_{sx}	Solid velocity parallel with thermal gradient
V_{sy}	Solid velocity perpendicular to thermal gradient
v_T	Casting velocity
v^*	Velocity of solid-liquid interface

x^*	Actual position of interface
x, y, z	Global Cartesian coordinates

Greek Symbols

α	Coefficient of thermal expansion
β	Shrinkage factor
γ_{gb}	Energy of the grain boundary
γ_{sl}	Energy of solid-liquid interface
γ_{SL}	Interfacial energy between solid and liquid
ΔP_{ε}	Pressure drop associated with deformation
ΔP_{sh}	Pressure drop associated with shrinkage
ΔP_c	Critical cavitation pressure
ΔT_b	Coalescence undercooling
ΔS_f	Entropy of fusion per unit volume
δ_{sl}	Diffuse solid-liquid interfacial thickness
ε_{app}	Apparent strain
ε_{free}	Free thermal contraction strain
ε_{fr}	Elongation to failure
ε_{int}	Internal strain
ε_{sh}	Linear shrinkage
ε_p	Total plastic strain
ε_{p0}	Constants value used to avoid convergence issues
ε^*	Characteristic strain

$\dot{\varepsilon_p}$	Equivalent plastic strain rate
$\dot{\varepsilon}_{ij}$	Strain rate tensor in the global coordinate
$\dot{\varepsilon}_{pH}$	Hoop strain rate
λ	Surface tension
λ_2	Secondary dendrite arm spacing
μ_l	Liquid viscosity
ρ_l	Liquid density
ρ_s	Solid density
$\bar{\rho}$	Average density of the mushy zone
σ	Stress
σ_s	Solid flow stress

Abbreviations

ASTM	American Society for Testing and Materials
BTR	Brittle Temperature Range
DC	Direct Chill
HCS	Cracking Sensitivity Coefficient
HDC	Horizontal Direct Chill
RVE	Representative Volume Element
SPV	Speisungsvermögen (maximum volumetric flow rate)
SRG	Schrumpfungsgeschwindigkeit (volumetric solidification shrinkage)
VDC	Vertical Direct Chill

Chapter 1

Introduction

1.1 Aluminum Alloys

Aluminum is the most widespread metal in nature, and it makes up more than 8 percent of the earth's crust. There is no source of pure aluminum and it can only be found in combination with oxygen and other elements. Production of aluminum from its ore, known as bauxite, is based on the use of electrical energy and costs a lot of money. In the 19th century, due to the difficulty of refining aluminum, it was considered even more scarce and valuable than gold! However, as time passed, the price of aluminum dropped owing to the invention of the Hall-Héroult process in 1886, and the advancement of renewable energy resources. In the 21st century, aluminum is the second most widely used metal after steel and is a part of the ongoing development of many industries such as transportation, construction, electronics, and packaging [3, 4]. The addition of alloying elements significantly alters the microstructure and mechanical properties of pure aluminum, providing its alloys with valuable properties. Aluminum alloys are lightweight, corrosion resistant, formable

and highly conductive to heat and electricity. All these properties make aluminum alloys an essential part of our everyday life. One of the most important characteristics of aluminum alloys is their recyclability. Since aluminum is corrosion resistant, it can be easily remelted and used again and again. Recycling of aluminum products such as automotive parts and beverage cans needs less than 10 percent of the energy required to produce aluminum from its ore [5].

Aluminum alloys are categorized into two main groups, cast alloys and wrought alloys. Cast aluminum alloys are used when the aim of the process is to cast near-net shape products. In such processes, the molten metal is poured into a mold, which can be made of sand, an alloy with much higher melting temperature, foam, etc. According to the American Society for Testing and Materials (ASTM), cast alloys are shown with a four-digit number with a decimal point before the fourth digit. The first digit indicates the major alloying element, the second and third digits are arbitrary, and the decimal indicates whether the product form is casting or ingot. Table 1.2 lists the standard designation for cast aluminum alloys [3].

Table 1.2: The standard designation for cast aluminum alloys [3]

Series	**Alloying elements**
1xx.x	Unalloyed compositions
2xx.x	Copper
3xx.x	Silicon plus copper and/or magnesium
4xx.x	Silicon
5xx.x	Magnesium
6xx.x	Not used
7xx.x	Zinc
8xx.x	Tin
9xx.x	Other elements

Wrought aluminum alloys are used to produce large rectangular ingots or cylindrical billets, which are subjected to further fabrication processes such as extrusion, rolling, forging, drawing, etc. The most important advantage of wrought aluminum alloys is their combination of high workability and ability to fabricate different products like sheet, tube, rod, wire, extrusions and so on. As shown in Table 1.3, the American Society for Testing and Materials (ASTM) has classified wrought aluminum alloys based on the main alloying element into 9 main groups. In this designation system, each alloy is identified by a four-digit number [3].

Table 1.3: The standard designation for wrought aluminum alloys [3]

Alloy	**Main alloying element**
1xxx	Mostly pure aluminum; no major alloying additions
2xxx	Copper
3xxx	Manganese
4xxx	Silicon
5xxx	Magnesium
6xxx	Magnesium and silicon
7xxx	Zinc
8xxx	Other elements (e.g., iron and silicon)
9xxx	Unassigned

1.2 Direct Chill Casting of Aluminum Alloys

In the mid 1930s, the main process of fabricating large extrusion billets and rolling ingots was permanent mold casting in which the molten metal was poured into a large mold. However, with the increasing demand for larger castings as well as structural issues including a low heat extraction rate, air gap formation, and turbulence during

pouring, a new process-the direct chill casting process- was invented [6]. Based on the mold orientation, the DC (direct chill) casting process is classified into two groups of HDC (horizontal direct chill) casting process and VDC (vertical direct chill) casting, which is the predominant method [7].

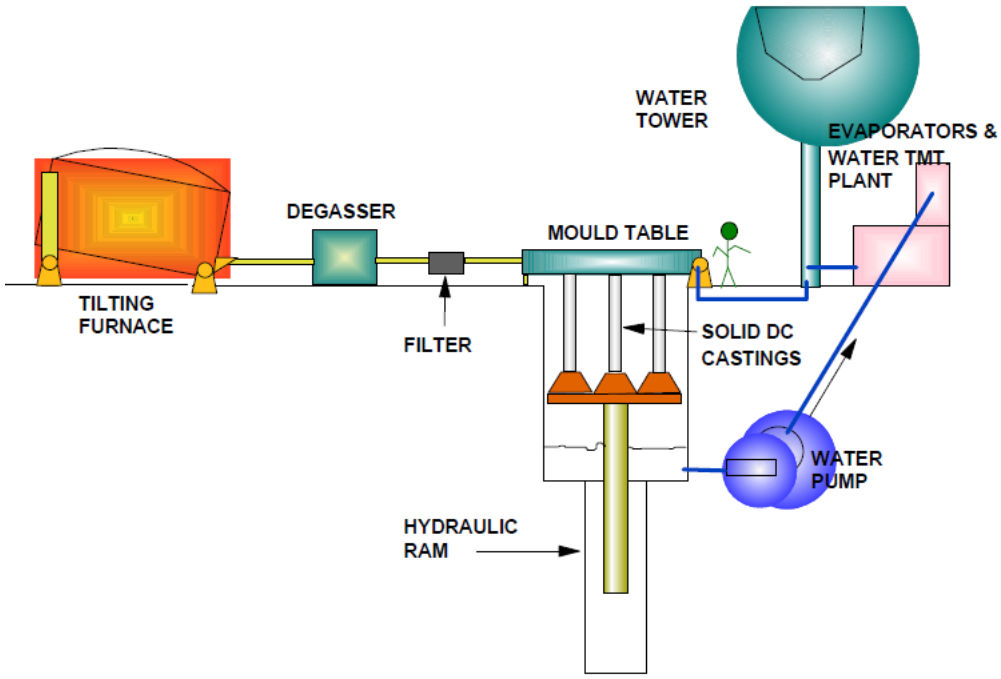

Figure 1.1: Simple layout of a typical vertical direct chill casting setup [8].

As schematically shown in Fig. 1.1, VDC casting installation mainly consists of a bottomless water-cooled mold having a desired cross-section and a bottom block connected to a hydraulic ram. At the beginning of the process, the bottom block and the mold create a closed space. The superheated alloy is melted in a resistance tilting furnace, then directed to flow through a degasser and a filter to get rid of the dissolved hydrogen and solid impurities, respectively, before entering the mold [8]. The superheated alloy is continuously poured into the mold from the top with a

specified rate and loses heat in contact with the mold and bottom block. The outer part of the alloy solidifies and creates a solid shell. When the solid shell is strong enough to hold the metal in the center that is not solidified yet, the bottom block moves downward at a prescribed rate, known as casting speed. The part of the casting that is not in contact with the mold anymore is cooled down by water sprays impinging directly on the surface of the billet. When the billet reaches the desired height, liquid feeding from the top is stopped and the billet is removed from the casting setup. The operation is then repeated for the next casting [9, 10]. A schematic of the DC casting process is illustrated in Fig. 1.2.

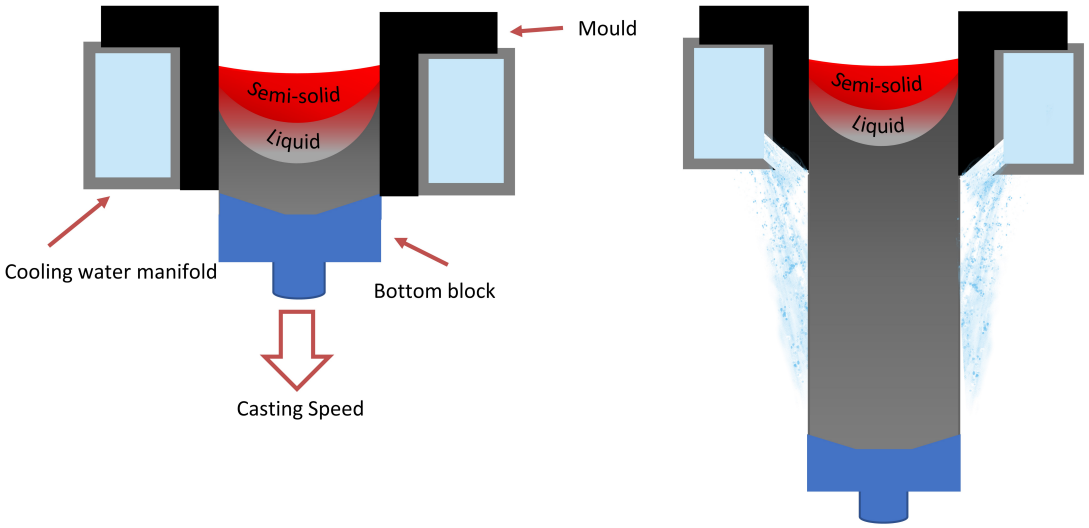

Figure 1.2: A schematic of aluminum billet DC casting process.

During the DC casting process, the metal is subjected to different cooling conditions. First, the metal is chilled in contact with the water-cooled mold as well as the bottom block, known as primary cooling. As the bottom block moves downward, the

metal is cooled down directly via water sprays bellow the mold, known as secondary cooling. The water sprays remove 80 to 95 percent of the heat during the casting. Although primary cooling is only responsible for extracting 5 to 20 percent of the total heat, it is a critical step toward ensuring that the casting itself can contain the liquid metal below the mold exit [11, 10].

From the perspective of heat flow, the DC casting process can be divided into three phases. The "start-up" phase starts with the beginning of the DC casting process; it is relatively short (several minutes) with respect to the total casting time and is characterized as having temperature fields that vary with both time and position. When the bottom block has moved far enough from the mold so that the billet has reached 0.5 to 1 metre in height, the "steady state" region is achieved [12, 13]. In this region, the thermal and mechanical field quantities remain rather constant with respect to the cast length. Finally, when the bottom block movement and molten metal feeding from the top are stopped, the casting experiences a transient condition again called "end phase" [14]. It is required to distinguish between different phases due to the fact that the temperature distribution determines the final quality of the casting, as it controls the position of solidification front, as well as the cooling rate, stress and strain evolution within the casting [8].

1.3 Solidification Defects in DC Casting

Although the DC casting process might sound straightforward in principle, many production problems associated with the process have been observed, which can affect the quality of the final product. Hence, it is essential to pay a special attention to controlling process parameters, namely, casting speed, cooling water flow rate,

pouring temperature, cast dimensions, and mold design. The start-up phase of the DC casting is the most critical phase because of its transient nature. During the start-up phase, different parts of the billet are exposed to variable cooling condition, which gives rise to the formation of several defects.

DC cast products exhibit two types of cracks. Hot tears, which initiate if the restricted feeding of molten metal is combined with the tensile stresses and strains generated in the billet due to inhomogeneous contraction in the start-up phase before the solidification ends. This defect will be extensively addressed in Chapter 2. Cold crack is another type of crack, which also occurs due to high thermal stresses, but after the alloy is fully solidified and in lower temperatures [15].

When the molten metal first solidifies in contact with the bottom block, it shrinks and lifts off the bottom block. The phenomenon that deforms the bottom of the billet is known as "butt curl" and results in reduced rigid standing or instability of the billet. As butt curl occurs, the solidified shell loses its support from the bottom block and the mold; therefore, the molten metal will tear up the billet shell due to high temperature of the liquid pool and the metallostatic pressure and causes "bleed-out" or "run-out". If the molten metal comes into contact with cooling water as a result of bleed-out, explosion can occur [16, 8].

One of the other major defects associated with DC casting of aluminum alloys, which has a detrimental effect on mechanical properties and especially fatigue resistance is microporosity. During solidification of aluminum alloys, porosity is formed due to two reasons. Firstly, since hydrogen is 10 times less soluble in solid aluminum than liquid aluminum, reduction of hydrogen solubility in aluminum melt as the temperature drops causes the dissolved hydrogen to get trapped in interdendritic

or granular regions and give rise to gas porosity. Nonmetallic inclusions, oxide films, solidification conditions, the initial hydrogen content, and alloy composition all influence the formation of gas porosity. For instance, the addition of some alloying elements affects the percentage porosity in DC cast billets due to the fact that they change the hydrogen uptake in aluminum melt. Microporosity can also be attributed to volume change occurring during solidification and lack of liquid feeding in interdendritic regions [17, 18].

Another important defect occurring during the DC casting process is variation in composition with position known as segregation. Unlike pure metals, which solidify at a constant temperature, solidification of alloys occurs over a range of temperatures and compositions. The difference between the solubility of the alloying elements in solid and liquid causes chemical inhomogeneity. If the variation in composition occurring in a casting ranges from several millimeters to meters, it is called macrosegregation; however, nonhomogeneous structure can also occur on the scale of grains, which is known as microsegregation [19].

1.4 Simulation of DC Casting Process

The DC casting technology has been studied for a long time; however, many challenges associated with the process still exist. As briefly explained in the previous section, the process is susceptible to the formation of several types of defects, which have detrimental effects on the mechanical properties of semi-fabricated and finished products. In addition, the modification of defects during downstream processing operations is not an easy task. Therefore, it is vital to control the cast structure as well as prevent the formation of defects during the casting process. Several process

variables such as casting speed, cooling water flow rate, melt temperature, the cast alloy, and bottom block geometry contribute to the final product quality; thus, the optimization of the process with the purpose of improving product quality, productivity and cost-efficiency is of great importance. From the processing standpoint, many defects arising during the course of solidification are related to the casting geometry and may not be observed in lab-scale experiments. Over the past few years, computer-based modeling has provided a valuable means to improve the DC casting process in terms of process optimization and prediction of defects. As the computational models mature, more process details can be simulated and consequently the trend toward implementing computer simulation rather than conducting experimental studies increases. Prediction of hot tearing using numerical methods has attracted considerable attention due to the severity of the issue, which can cause the whole casting to be rejected. This master's thesis focuses on predicting hot tear formation in DC casting of aluminum alloys by implementing an elaborate computational modeling technique. In the next chapter, a review of the relevant literature will be presented [20, 21, 22].

Chapter 2

Literature Review

2.1 Hot Tearing

Hot tearing, also known as hot shortness, hot cracking or hot brittleness, is one of the most severe and unrecoverable defects encountered in casting operations and can be seen inside or on the surface of DC cast billets and ingots. Hot tearing is a serious quality issue in the DC casting of aluminum alloys, which can cause the DC cast round billets and rectangular ingots to be entirely rejected or large amounts of scrap to be remelted [23, 22].

As explained by Campell [24], a hot tear is a branching crack and it consists of a main tear and several minor offshoots that can be seen on intergranular paths using optical microscopy. Hot tears develop in locations where strain is highly concentrated within the casting. There is no certain condition for the formation of hot tears and for different castings with the same conditions, it is not guaranteed that hot tears would initiate and propagate in all them. Schematics of hot cracks at the central region of an extrusion billet and a cracked rectangular ingot are shown Fig. 2.1 (a)

and (b), respectively.

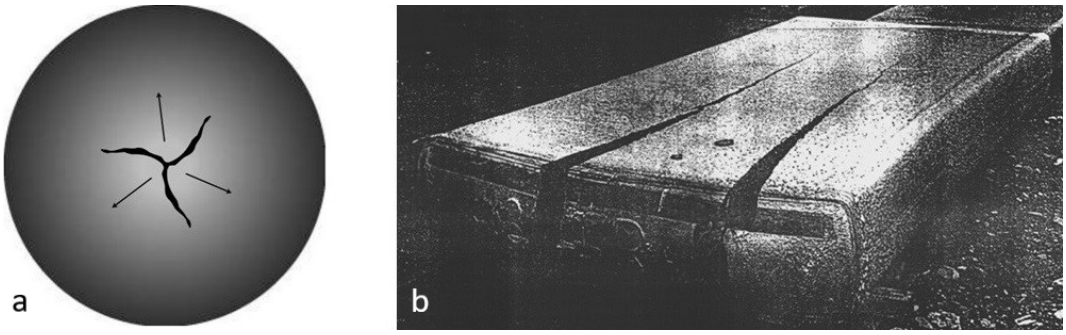

Figure 2.1: Examples of hot tearing in aluminum alloys; (a) extruded billet, (b) rectangular ingot [25, 26].

While pure metal solidifies at a constant temperature, alloys solidify over a range of temperatures known as solidification range or freezing range. In other words, during the solidification of alloys, there is a region in which solid and liquid phase coexist. The alloy in such region is described as "semi-solid", which is classified into two types of "slurry" and "mush". At lower solid fractions, solidified grains are suspended in liquid which is called slurry. Below a specific temperature, known as "coalescence temperature", solid grains come into contact with each other and the semi-solid material develops certain strength. The semi-solid below this temperature is known as mush. Based on the morphology of solid particles, the transition from the slurry to the mush occurs between 0.25-0.6 solid fraction [27, 28].

Hot tears initiate during the transient start-up phase in the mushy zone at high solid fractions after the coalescence temperature has been reached. It is generally believed there are two main reasons behind the formation of hot tears. First, due to uneven cooling condition in the start-up phase, different regions of the casting experience a non-uniform contraction, which causes the billet to be subjected to

tensile stresses and strains generated by thermally-induced deformation. Second, because of the solidification shrinkage, it is difficult for liquid to flow in interdendritic regions at high solid fractions. Consequently, dry intergranular regions will tear apart as a result of tensile deformation [4, 29]. Fig. 2.2 illustrates a schematic description of hot tearing formation in the semi-solid region.

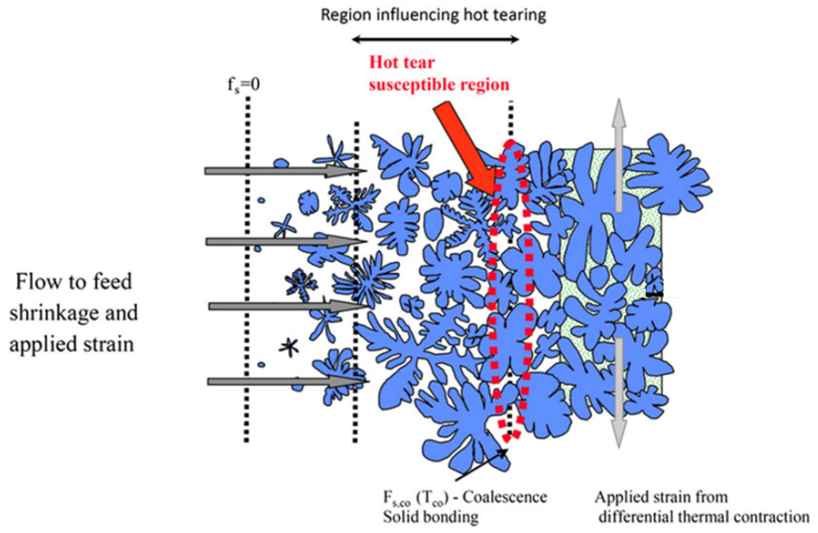

Figure 2.2: Schematic of the semi-solid region showing factors affecting hot tearing [30].

In order to explain hot tearing, an alloy's behavior in the semi-solid region should be understood. Considering permeability of the solid structure to be the governing factor, Clyne and Davis [31] divided the solidification process into four stages as shown in Fig. 2.3:

a Mass feeding: in this stage, which corresponds to liquid fraction of slurry, solid particles and liquid are both free to move.

b Interdendritic feeding: in this stage, which occurs at higher solid fractions than mass feeding stage, a continuous dendritic network is formed; therefore, the solid is no longer free to move, but liquid has to flow through the dendritic network to compensate for stress accumulation.

c Interdendritic separation: in this stage, the semi-solid is susceptible to hot tear or pore formation, the solid fraction is high and thus the low permeability of the solid skeleton prevents the liquid flow. Therefore, further thermal contraction of the solid results in hot tear or pore initiation.

d Interdendritic bridging: in this stage, the structure has developed moderate strength and solid state creep compensates for further contraction.

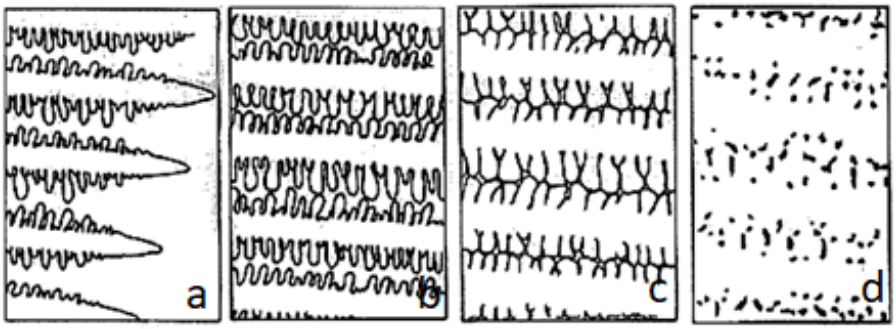

Figure 2.3: Schematic of typical microstructure correspond to four stages of solidification: (a) mass feeding, (b) interdendritic feeding, (c) interdendritic separation, and (d) interdendritic bridging [32].

2.2 Hot Tearing Mechanism

Hot tearing is a complicated defect attributed to the combination of different transport phenomena, i.e. fluid flow, mass flow and heat flow in the mushy zone. Therefore,

a good understanding of the behavior of the as-cast material is necessary. Many authors have studied the phenomenon and proposed different mechanisms addressing the problem of hot tearing. Moreover, in order to predict hot tearing formation, various criteria have been developed [33]. In the following, the most important hot tearing theories are discussed.

Hot tearing investigations date to the 1920's when Korber and Schitzkowski [34] carried out a study addressing hot tearing in carbon steels. It is a widely held view that the occurrence of hot tearing is due to development of shrinkage as well as thermally and mechanically driven deformation during the solidification of alloys. However, there is no agreement on the parameter controlling this defect. Some researchers believe that the stress is the main parameter. On the other hand, other researchers consider strain, strain rate, or other factors as the most significant determinants accounting for the phenomenon [35].

In 1936, Verö [36] reported that hot tearing in aluminum alloys is a consequence of the formation of a coherent dendritic network in the last stage of solidification leading to stress accumulation as solidification proceeds. In addition, Verö proposed that the remaining eutectic liquid is capable of healing the primary tears.

In 1948, Pumphrey et al. [37] studied hot cracking in welding processes. They brought up a new term called "brittle temperature region", i.e. the range between the temperature at which a coherent dendrite network is developed and the solidus temperature. They proposed that hot tear formation is due to the thermal contraction and stress accumulated in the material and is likely to occur in this region as a result of little ductility of the material near the end of solidification. They also stated that the development of hot tears is linked to the remaining residual liquid.

After studying hot tear formation in Al-Cu alloys using X-ray radiography and thermal analysis, Pellini (1952) [38] suggested that the initiation of hot cracks is a strain controlled phenomenon and occurs above the solidus temperature, where the remaining liquid is as low as it creates a thin continuous liquid film covering the solid skeleton. In his theory that is based on the strain localization in intergranular regions, hot tears will develop when the accumulated strain in a liquid film exceeds a critical value. Moreover, Pellini noted the importance of strain rate and liquid film life on the occurrence of hot tears.

In 1960, Rosenberg et al. [39] considered the lack of liquid feeding between the grains at high solid fraction as the main reason for hot tearing occurrence. Later, a number of porosity and hot tearing criteria, which are described in Section 2.4 of this chapter were developed. These criteria are based on pressure depression in the mushy zone associated with hindered feeding of the solid phase by the liquid [40, 41].

In 1962, Prokhorov [42] suggested that hot tearing is a strain rate-controlled phenomenon. He believed that if a certain amount of time is given to the material in the semi-solid state, it can accommodate strain by different mechanisms. Therefore, if the material is subjected to deformation at a high rate, hot tears would develop.

In 1991, Campbell [24] believed that hot tearing occurrence is a result of uni-axial tensile stresses and theories based on lack of liquid feeding are unable to explain the phenomenon. In his view, feeding difficulties cause tri-axial stress, which leads to porosity formation.

In 2005, Fredriksson et al. [43] postulated that hot tearing results form the supersaturation of vacancies occurring during solidification processes. They proposed that

the energy level of the solidified alloy is significantly higher than providing equilibrium values, which can be explained by the formation of vacancies and lattice defects during solidification. Consequently, any stress or strain accumulation would cause the condensation of vacancies leading to crack initiation and growth [44].

Among the above-mentioned mechanisms proposed to explain the hot tearing phenomenon, in recent years, mechanisms based on limited feedability of the mushy zone in combination with deformation of the semi-solid skeleton have been widely accepted by several researchers. However, the main concern of the casting industry, i.e. quantitatively predicting hot tearing formation in different casting processes, remains.

2.3 Hot Tearing in DC Casting

Hot tears are known to develop in the hot spots of the casting, where the casting is about to finish solidifying and tensile strains are localized. If we want to classify hot tears associated with the DC casting process based on their location, three types of cracks, namely, internal, surface, and butt cracks, have been observed. Internal cracks occur because the solidified shell keeps the entire billet from contracting; consequently, shrinkage in the central part of the billet experiences tensile stresses which results in crack formation. The formation of the air gap reduces the heat transfer rate at the surface of the casting; therefore, as a result of high melt temperature, the solidified shell might melt and create a hot spot, which becomes in tension due to the secondary cooling and gives rise to surface crack initiation. Butt cracks are caused by the thermal stresses associated with the heat extraction through the mold and the bottom block [45, 46].

2.3.1 Parameter Sensitivity

There are several parameters critical to the formation of hot tearing in DC casting. However, all parameters can be divided into two major groups of Alloy Parameters and Processing Parameters. In the following, the most important parameters of each group are briefly discussed.

2.3.1.1 Alloy Parameters

As reported by several systematic studies carried out since the 1930s, the alloy chemistry affects hot tearing in different ways [36]. Grain morphology and its size are among alloy parameters affecting hot tearing. Many studies suggested that grain refinement has a positive impact on hot tearing resistance in general. The study conducted by Warrington et al. [47] on DC cast aluminum 7050 and 7010 alloys showed that the addition of grain refiners changes the grain structure from columnar to equiaxed-dendritic grains and consequently decreases hot cracking vulnerability. However, by adding more grain refiner, more cracks appeared, which was explained to be due to the decrease in the permeability of the mushy zone [48].

According to the study conducted by Pumphrey et al. [49] on six aluminum binary alloys, i.e. Al-Mg, Al-Cu, Al-Fe, Al-Si, Al-Zn, and Al-Mn using the ring casting test, the amount of alloying element influences the length of the cracks appearing on the ring surface. They observed that the crack length for all mentioned systems, first increased and then decreased by further addition of the alloying element to pure aluminum. It was noted that the chemistry determines the grain morphology; increasing the amount of alloying elements changes the grain morphology from columnar to

equiaxed, which is less prone to cracking [49]. Fig. 2.4 (a) and Fig. 2.4 (b) illustrate schematic representation of a binary phase diagram with a eutectic point and the corresponding hot tearing susceptibility curve. As can be seen, hot tearing tendency as a function of alloy composition in binary eutectic systems, tends to follow a lambda-shaped curve (λ) [50, 51], meaning that hot tearing susceptibility increases with the weight percent of alloying element until it reaches a maximum value and then is followed by a decrease with further addition of alloying element. Moreover, larger freezing range leads to a greater vulnerability to hot tearing as the alloy spends a longer time in susceptible regions [35].

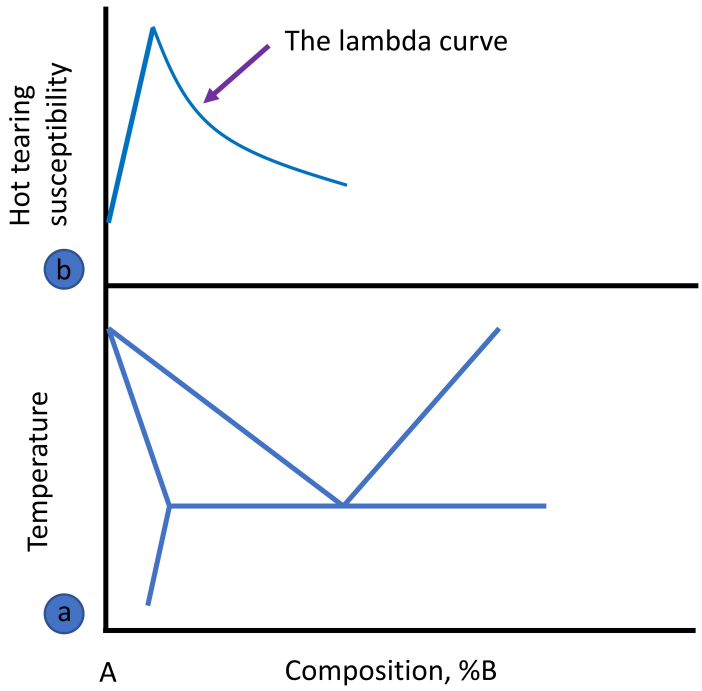

Figure 2.4: Schematic representation of (a) a binary phase diagram with a eutectic point, and (b) the corresponding hot tearing tendency curve as a function of alloy composition [50].

It has been also demonstrated that there is a relation between the amount of eutectic and hot tearing propensity. Rosenberg et al. [39] reported that the microstructure in which the primary grains are surrounded by thicker eutectic phase exhibits more hot tearing resistance since the eutectic phase improves healing phenomenon or in other words the liquid feeding [52].

2.3.1.2 Processing Parameter

Hot tearing tendency has also been studied in terms of processing parameters including casting speed, melt temperature, and cooling water flow rate since all these parameters influence melt flow and cooling conditions, which affect the stress induced by thermal contraction and solidification shrinkage.

Although several studies have been conducted to examine the effect of melt superheat on hot tearing defects in different casting alloys, contrary opinions have been expressed in the literature [35]. However, in the case of aluminum alloys, most researchers have agreed that the cracking tendency increases with the melt temperature. High melt temperature increases the thermal gradient during the solidification, which promotes the growth of columnar dendritic grains with lower hot tearing resistance compared to equiaxed globular grains. Furthermore, high melt temperature causes thicker liquid film leading to higher susceptibility to hot cracking [53, 54].

In agreement with industrial experience and experimental studies, hot tearing is more likely to happen at high casting speeds due to several reasons. Larger casting speed provides higher solidification rate and deeper mushy zone; both increase the chance of hot tearing initiation [55]. Zheng et al. [56] observed larger columnar grains and increasing amount of macrosegregation as a result of higher casting speed; both

are assumed to be detrimental factors for hot tearing resistance.

Cooling water controls the heat extraction from the mold. High cooling water flow rate causes uneven thermal contraction, meaning that the surface cools down faster than the center which lead to accumulation of stresses and strains and consequently hot tearing development [15].

2.4 Hot Tearing Criteria

Based on the mechanisms presented in Section 2.2, several criteria have been proposed to predict hot tearing. There are various classifications of hot tearing criteria. Here we divide hot tearing criteria into three main groups of non-mechanical criteria, mechanical criteria, and criteria combining both mechanical and non-mechanical features. In the following, a few important examples of each category are reviewed.

2.4.1 Nonmechanical Criteria

Feurer′s [41] nonmechanical criterion considered the lack of liquid feeding through the semi-solid body as the main cause of hot tearing. He suggested that the main cause of hot tearing can be explained by considering the competition between liquid feeding, which is restricted due the difficulty of fluid flow through the semi-solid body in the last stage of solidification, and solidification shrinkage. In this theory, two terms are calculated. First, the SPV term which stands for maximum volumetric flow rate in the interdendritic region and is defined as:

$$SPV = \frac{{g_l}^2 \lambda_2^2 P_s}{24\pi c^3 \mu_l L^2}, \tag{2.1}$$

where g_l is the volume fraction of liquid, λ_2 is the secondary dendrite arm spacing, P_s is the effective feeding pressure, c is the tortuosity constant, μ_l is the viscosity of the liquid, and L is the length of the network. The P_s term requires further equations, i.e.:

$$P_s = P_0 + P_m - P_c, \tag{2.2}$$

with:

$$P_m = \bar{\rho} g h, \tag{2.3}$$

$$\bar{\rho} = \rho_l g_l + \rho_s g_s, \tag{2.4}$$

$$P_c = \frac{4\gamma_{SL}}{\lambda_2}. \tag{2.5}$$

In Eq. 2.2, P_0, P_m, and P_c are the atmospheric, metallostatic, and capillary pressure, respectively. In Eq. 2.3, $\bar{\rho}$ is the average density of the mushy zone, g is the gravitational constant, and h is the distance to the melt surface. In Eq. 2.4, ρ_l and ρ_s are liquid and solid phase densities and g_l and g_s are volume fraction of liquid and solid, respectively. In Eq. 2.5, γ_{SL} is the interfacial energy between solid and liquid.

Second, the SRG term which indicates volumetric solidification shrinkage, is formulated as:

$$SRG = (\frac{\partial \ln V}{\partial t}) = -\frac{1}{\bar{\rho}} \frac{\partial \bar{P}}{\partial t}, \tag{2.6}$$

where V is the volume element of the mushy zone with constant mass and t is the time. Based on Feurer's theory, two conditions may occur; if $SPV > SRG$, it means that

there is sufficient volumetric liquid feeding through the mushy zone and hot tearing is impossible, and if $SPV < SRG$, it means that liquid feeding cannot compensate for solidification shrinkage and hot tearing is possible.

Clyne and Davis [57] proposed their hot tearing criterion based on the 4 stages of solidification processes explained in Section 2.1 and stated that hot cracking is due to the opening of the mushy zone in response to the strain applied during the interdendritic separation stage. They believed that cracks forming in the last stage of solidification cannot be healed because it is difficult for liquid to move freely to interdendritic regions. They divided the mushy zone into two regions; mass/liquid feeding zone ($0.4 < g_s < 0.9$) and interdendritic separation zone ($0.9 < g_s < 0.99$). As shown in Eq. 2.7, the Hot Cracking Sensitivity coefficient (HCS) introduced by Clyne and Davies is given by the ratio of the vulnerable time interval (t_V), where hot tearing may develop and the time interval spent by the mushy zone to relief stress or relaxation time (t_R):

$$HCS = \frac{t_V}{t_R} = \frac{t_{99} - t_{90}}{t_{90} - t_{40}}. \tag{2.7}$$

Katgerman [58] derived his criterion by combining theoretical assumptions of Feurer and of Clyne and Davies to calculate hot cracking tendencies as a function of alloy composition, casting speed and ingot diameter in DC casting of aluminum alloys. Considering cylindrical coordinates, he applied a simple heat flow model of DC casting to propose a criterion as shown below:

$$HCS = \frac{z_{99} - z_{cr}}{z_{cr} - z_{40}}, \tag{2.8}$$

where z_{cr} is the distance along the ingot axis where feeding is not allowed anymore and is given by the height at which $SPV = SRG$ using Feurer's criterion and z_{40} and z_{99} are the distances where solid fractions are 0.4 and 0.99, respectively.

2.4.2 Mechanical Criteria

Prokhorov [42] proposed a criterion by assuming that the development of strain is caused by geometrical configuration as a result of solidification shrinkage. As the geometry gets more complicated, the strain experienced by the material increases. He suggested that during the solidification process there is a temperature range between the coherency temperature and the solidus temperature known as Brittle Temperature Range (BTR) in which the semi-solid body possesses low ductility or, in other words, low deformation capacity. Prokhorov defined the balance condition for strain as:

$$\varepsilon_{app} = \varepsilon_{free} + \varepsilon_{int}, \tag{2.9}$$

where ε_{app} is the apparent strain, ε_{free} is the free thermal contraction strain, and ε_{int} is the internal strain due to configuration of the solidifying body and shrinkage. He introduced a term called the reserve of strength, ε_{res}, which can be written as:

$$\varepsilon_{res} = D_{min} - (\varepsilon_{free} + \varepsilon_{app}), \tag{2.10}$$

where D_{min} is the minimum ductility; if each term is divided by the brittle temperature range (ΔT_{br}), it reads:

$$\frac{\varepsilon_{res}}{\Delta T_{br}} = \frac{D_{min}}{\Delta T_{br}} - \frac{\varepsilon_{free}}{\Delta T_{br}} - \frac{\varepsilon_{app}}{\Delta T_{br}}, \tag{2.11}$$

i.e.:

$$\alpha_{res} = \alpha_{min} - \alpha_{free} - \alpha_{app}. \tag{2.12}$$

where α is the strain or ductility rate in terms of temperature dependence. If one multiplies Eq. 2.12 by cooling rate ($\dot{T} = \frac{\partial T}{\partial t}$), it becomes:

$$\dot{\varepsilon}_{res} = \dot{\varepsilon}_{min} - \dot{\varepsilon}_{free} - \dot{\varepsilon}_{app}, \tag{2.13}$$

Prokhorov suggested that hot tearing develops if $\dot{\varepsilon}_{res} \leq 0$, which means:

$$\dot{\varepsilon}_{min} - \dot{\varepsilon}_{free} \leq \dot{\varepsilon}_{app}. \tag{2.14}$$

Novikov [59] suggested a criterion based on the ductility of semi-solid non-ferrous alloys. He proposed a term called "reserve of plasticity", p_r, which is defined as the area between the elongation to failure (ε_p), and the linear shrinkage (ε_{sh}) over the brittle temperature range (ΔT_{br}). Fig. 2.5 (a) and (b) show schematic of ε_p and ε_{sh} as a function of temperature in a semi-solid body. Based on the relative position of the two curves, p_r reads:

$$p_r = \frac{S}{\Delta T_{br}}, \tag{2.15}$$

where S is the area between between ε_p and ε_{sh} in Fig. 2.5 (a). However, if the two curves intersect as depicted in Fig. 2.5 (b), p_r is defined as:

$$p_r = \frac{S_1 - S_2}{\Delta T_{br}}, \tag{2.16}$$

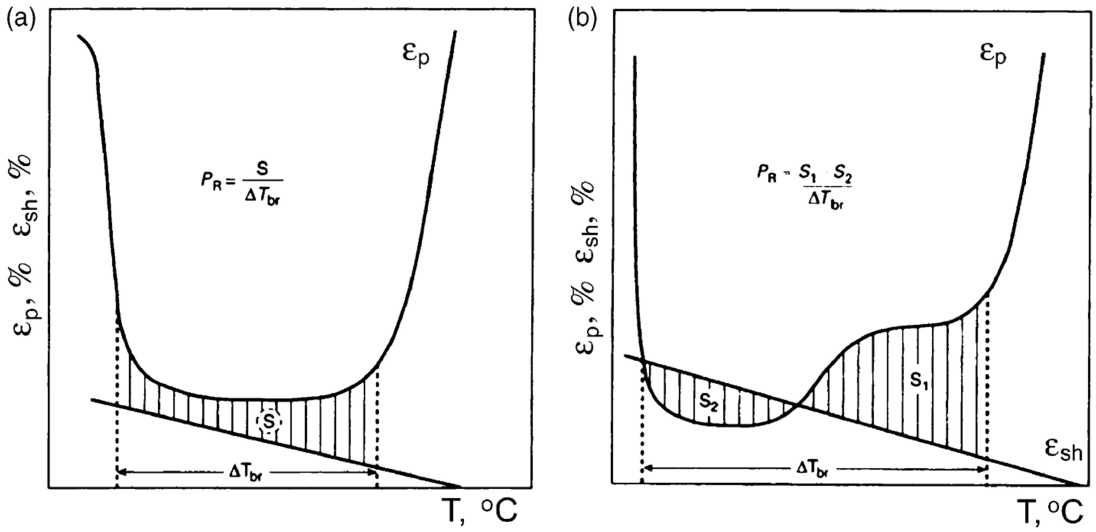

Figure 2.5: Schematic representation of the relative position of elongation to failure (ε_p) and linear shrinkage (ε_{sh}) in the brittle temperature range [59].

2.4.3 Combined Criteria

In 1999, Rappaz, Drezet, and Gremaud [60] proposed a simple two-phase model by relating the tensile deformation of the mushy zone as well as the lack of liquid feeding to hot tearing formation. At high solid fractions, due to non-uniform thermal contraction, the dendritic network is subjected to tensile or shear stresses, which can increase the distance between the dendrite arms. In the early stage of solidification, liquid flow can compensate for such regions; however, at high solid fractions due to small permeability of the mushy zone, it is not easy for the remaining liquid to fill the gap, which gives rise to hot tearing formation. Rappaz et al. formulated their idea by considering the liquid pressure drop, defined as the difference between the metallostatic pressure (P_m) near the dendrite tips and the local pressure in the mush as the main cause of crack formation. As schematically shown in Fig. 2.6, liquid pressure decreases from its initial value at the tip to a lower value near the root of

the dendrites. Two terms are considered to account for pressure drop in the mushy

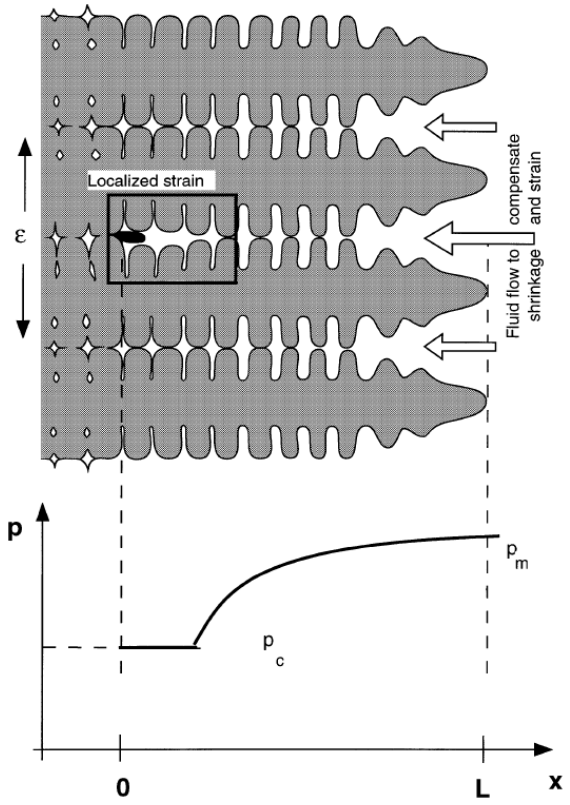

Figure 2.6: Schematic showing the variation of liquid pressure as a function of distance from the root of the dendrites and localization of straining at the roots in a columnar dendritic structure [60].

zone, i.e. pressure drop associated with deformation (ΔP_ε) and the contribution of shrinkage to pressure drop (ΔP_{sh}). The local pressure in the mush can then be expressed as:

$$P_l = P_m - \Delta P_\varepsilon - \Delta P_{sh}. \tag{2.17}$$

In order for hot tears to occur, the local pressure needs to fall below a critical cavitation pressure (ΔP_c), which is taken as 2 kPa by Rappaz et al. based on the work

by Ampuero et al. [61]. The model determines the shrinkage and deformation contributions to pressure drop by performing a mass balance on a small volume element of the mush shown in Fig. 2.7.

$$\mathrm{div}\langle \rho v \rangle - v_T \frac{\partial \langle \rho \rangle}{\partial x} = 0. \tag{2.18}$$

By assuming that liquid flows is in direction parallel with thermal gradient and the

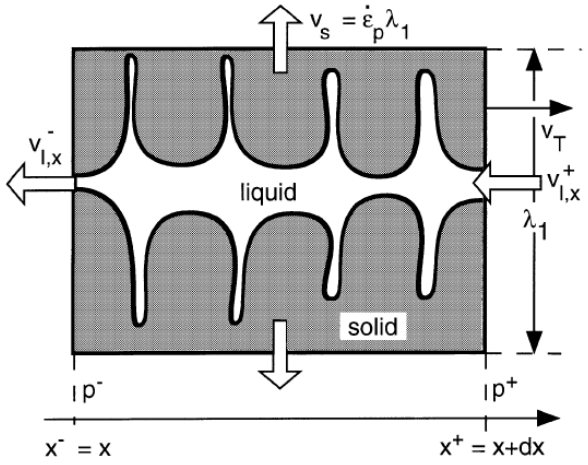

Figure 2.7: Schematic representation of a small volume element on which the mass balance equation is performed [60].

solid only deforms in the perpendicular direction to the thermal gradient, Eq. 2.18 can be written as:

$$\frac{\partial(\rho_l g_l v_{l,x})}{\partial x} + \frac{\partial(\rho_s g_s v_{s,y})}{\partial y} - v_T \Big[\frac{\partial(\rho_s g_s)}{\partial x} + \frac{\partial(\rho_l g_l)}{\partial x} \Big] = 0. \tag{2.19}$$

In this model the velocity of liquid in the mushy zone can be derived as:

$$g_l v_{l,x} = -(1+\beta)E(x) - v_T \beta g_l, \tag{2.20}$$

where β is the shrinkage factor, $E(x)$ represents the integration of $g_s.\dot{\varepsilon}$ over the length of the mushy zone, i.e. $\int g_s \dot{\varepsilon} dx$, and v_T is the casting velocity. The velocity of the liquid is related to the pressure gradient using Darcy equation:

$$g_l v_{1x} = -\frac{K}{\mu_l}\frac{dp}{dx}, \tag{2.21}$$

where v_{lx} represents the velocity of liquid in x direction, μ_l is liquid viscosity, and K is the permeability of the mushy zone, which is defined as Carman-Kozney equation:

$$K = \frac{\lambda_2^2}{180}\frac{(1-g_s)^3}{g_s^2}, \tag{2.22}$$

where λ_2 is the secondary dendrite arm spacing. Finally the pressure drop associated with shrinkage and deformation between the tip and the root of a dendrite can be calculated as Eq. 2.23, in which the first and the second terms are the deformation and the shrinkage contribution to the pressure drop, respectively.

$$\begin{aligned} p_L - p_0 = \Delta p_\varepsilon + \Delta p_{sh} = \frac{180}{\lambda_2^2}\frac{(1+\beta)\mu}{G}\int_{T_S}^{T_L}\frac{E(T)g_s(T)^2}{(1g_s(T))^3}dT + \\ \frac{180}{\lambda_2^2}\frac{v_T\beta\mu}{G}\int_{T_S}^{T_L}\frac{g_s(T)^2}{(1-g_s(T))^2}dT \end{aligned} \tag{2.23}$$

From Eq. 2.23, Rappaz et al. derived the maximum deformation rate that the mushy zone can withstand prior to nucleation of hot tears.

Although the RDG criterion has attracted much attention in recent years, Monroe and Beckermann [62] believed that the RDG approach has some limitations to be used for low thermal gradient situations, when shrinkage porosity is more probable to form than hot tears since in the formulation of the RDG criterion, hot tearing is

predicted without considering any imposed strain rate. They reformulated the RDG criterion based on the previous work by Carlson et al. [63] that used a dimensionless form of the well-known Niyama criterion to predict the amount of shrinkage porosity that forms in the casting of metallic alloys. Niyama et al. [64] defined the shrinkage porosity index as $\frac{G}{\sqrt{\dot{T}}}$, where G, the temperature gradient, and $\dot{T}$, the cooling rate are evaluated at a temperature near the end of solidification. Niyama proposed that for different casting alloys, there is a threshold Niyama value below which shrinkage porosity can be observed, which implies that as the thermal gradient decreases and cooling rate increases the condition for shrinkage porosity formation is more favorable. The Niyama criterion is one of the simulation outputs reported by all metal casting simulation packages; however, it is only used qualitatively and specifies regions in a casting that are more prone to contain shrinkage porosity. Also, it is only based on thermal parameters and solidification characteristics and properties of the casting alloy are not taken into account. In order to overcome such limitations, Carlson et al., developed the dimensionless Niyama criterion (N_y^*) expressed as:

$$\Delta P_{cr} = \frac{\beta \mu \Delta T_f}{\lambda_2^2} \frac{\dot{T}}{G^2} I_{g_{l,cr}}, \tag{2.24}$$

$$N_y^* = \sqrt{\frac{\Delta P_{cr} \lambda_2^2}{\beta \mu \Delta T_f}} \frac{G}{\sqrt{\dot{T}}} = \sqrt{I(g_{l,cr})}, \tag{2.25}$$

$$I_{g_{l,cr}} = \int_{g_{l,cr}}^{1} \frac{(1-g_l)^2}{g_l^2} \frac{d\theta}{dg_l} dg_l. \tag{2.26}$$

N_y^* can be found from Eq. 2.25; therefore the value of $I(g_{l,cr})$ is known and the integration limit in Eq. 2.26, can be inversely determined from the value of $I(g_{l,cr})$.

Once the critical liquid fraction is determined, the final pore volume fraction (g_p) is approximated using the following relation:

$$g_p = \beta' g_{l,cr}, \tag{2.27}$$

where $\beta' = \beta/\beta + 1 = (\rho_s - \rho_l)/\rho_s$ and β is shrinkage factor considering that the density of solid, ρ_s, and the density of liquid, ρ_l, are constant but not equal during solidification. ($\beta = (\rho_s - \rho_l)/\rho_l$). In order to investigate hot tearing, Monroe and Beckermann added a second term to Eq. 2.24 addressing the effect of deformation in accelerating the pressure drop:

$$\Delta P_{cr} = \frac{\beta \mu \Delta T_f}{\lambda_2^2} \frac{\dot{T}}{G^2} I_{sh(g_{l,cr})} + \frac{\mu_l (1+\beta) \Delta T_f^2}{\lambda_2^2} \frac{\dot{\varepsilon}}{G^2} I_d(g_{l,cr}), \tag{2.28}$$

where $I_{sh(g_{l,cr})}$ is the shrinkage related term, and $I_d(g_{l,cr})$ is the deformation related term. In this approach, instead of calculating the pressure drop across the entire mushy zone as suggested in the RDG criterion, the critical liquid fraction at which liquid flow ceases ($g_{l,cr}$), and dimensionless Niyama criterion (N_y^*) are found respectively. Then, mass conservation is applied to find the fraction of porosity resulting from shrinkage ($g_{p,sh}$) and deformation ($g_{p,d}$):

$$g_{p,sh} = \frac{\beta}{1+\beta} g_{l,cr}, \tag{2.29}$$

$$g_{p,d} = \varepsilon^* \eta^* g_{l,cr}, \tag{2.30}$$

where the term $\varepsilon^* = \frac{\Delta T_f \dot{\varepsilon}}{\dot{T}}$ called characteristic strain and can be estimated based on

experiment results or stress simulation in casting processes and η^* is the dimensionless form of the integrated solid fraction across the mushy zone:

$$\eta^*(g_{l,cr}) = \int_0^{g_{lcr}} (1 - g_l) \frac{d\theta}{dg_l} dg_l. \tag{2.31}$$

With this approach, Monroe and Beckermann predicted shrinkage ($g_{p,sh}$) and deformation pore fraction ($g_{p,d}$) as a function of dimensionless Niyama criterion and strain rate as shown in Fig. 2.8 (a) and Fig. 2.8 (b), respectively. It can be seen that for a constant applied strain rate, deformation and shrinkage pore fraction both decrease with the dimensionless Niyama criterion. Moreover, considering a constant Niyama criterion, both pore fractions increase with the strain rate implying that the increase in the applied strain rate directly affects hot tearing susceptibility.

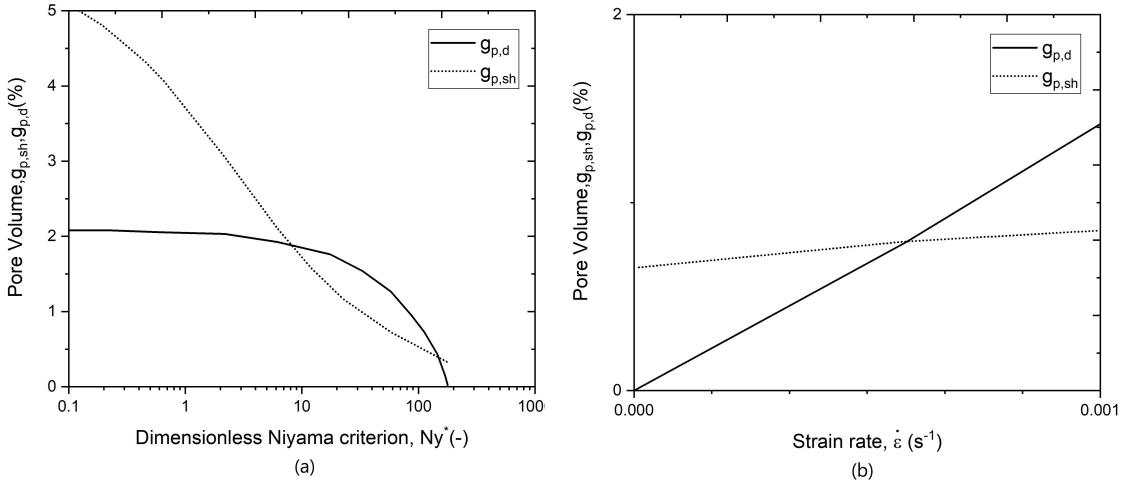

Figure 2.8: Predicted shrinkage and deformation pore fraction in Al-3wt.%Cu alloys (a) as a function of the dimensionless Niyama criterion with an applied strain rate of 10^{-3} s^{-1}, and (b) as a function of strain rate with a Niyama criterion value of 100 K $s^{0.5}m^{-1}$ [62].

From the aforementioned examples of hot tearing criteria and the other available criteria in the literature, it can be deduced that most of the hot tearing criteria are only able to predict hot tearing tendencies qualitatively without providing any detail about the location or severity of hot cracks.

2.5 Multi-physics Models

Hot tearing criteria predict the susceptibility of an alloy undergoing solidification to hot tearing for a given sets of processing conditions and alloy chemistry. However, they cannot predict whether or not a crack actually forms since such criteria are not able to predict the distribution of strain and localization of feeding at the grain boundaries, which both strongly influence the hot tearing phenomenon [65]. In the mushy zone, where both solid and liquid coexist, a great variety of grains in different morphologies such as columnar dendritic, equiaxed dendritic, and globular can nucleate and grow. Therefore, it is required to investigate the phenomenon at a more microscopic scale in order to account for intergranular and localized nature of grains [66]. Recently, researchers have proposed the use of multi-physics models that can directly investigate the simultaneous effect of both deformation and fluid flow on the solidification behavior at the microscopic scale. In this regard, different granular mechanics approaches have been suggested to link the semi-solid mechanical behavior of a domain with equiaxed globular microstructure to simulate the evolution of solid-liquid interface and fluid flow as a result of deformation and shrinkage.

Lahaie et al. [67] developed a model to simulate the response of the semi-solid body to an applied strain rate by predicting the ductility and liquid feeding in a 2-D semi-solid medium with an idealized microstructure, in which the solidification of all

grains occurs at the same rate, all solid grains are in the shape of hexagons as shown in Fig. 2.9, and the intergranular liquid is distributed uniformly between the grains before the deformation is applied. Although the authors claimed that the results of their model seemed to be in agreement with experimental observations, in reality, the solidification of grains is neither at the same rate nor in 2 dimensions.

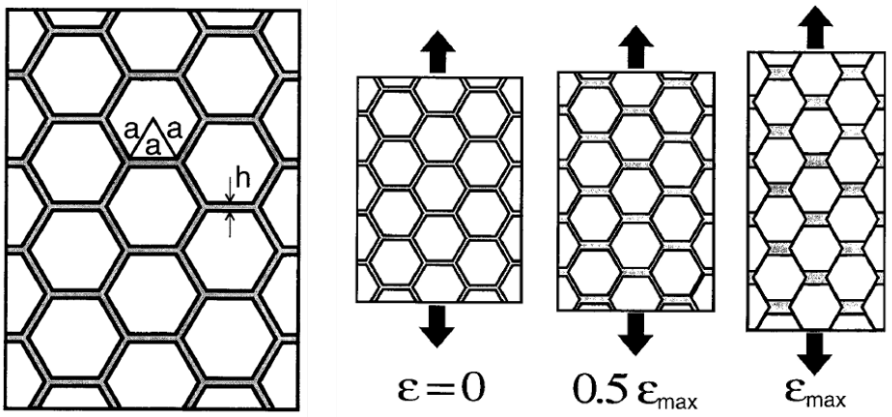

Figure 2.9: Schematic of the 2-D semi-solid structure with regular arrangement of grains and the tensile deformation of the semi-solid medium as a result of a constant applied strain rate with different strain values [67].

In order to account for the random arrangement of grains, Vernède et al. [68] developed a 2-D granular model to simulate the mechanical behavior of the mushy zone in which the grains are produced by a Voronoi tesselellation of random nucleation centers. As depicted in Fig. 2.10, which is schematic of a 2-D mushy zone at solid fraction of 0.92 and strain rate of 0.004 s^{-1}, this model is capable of simulating the grain structure at a given solid fraction, localization of fluid flow and the forces caused by liquid feeding and deformation.

Despite the progress made by 2-D techniques that take into account the random

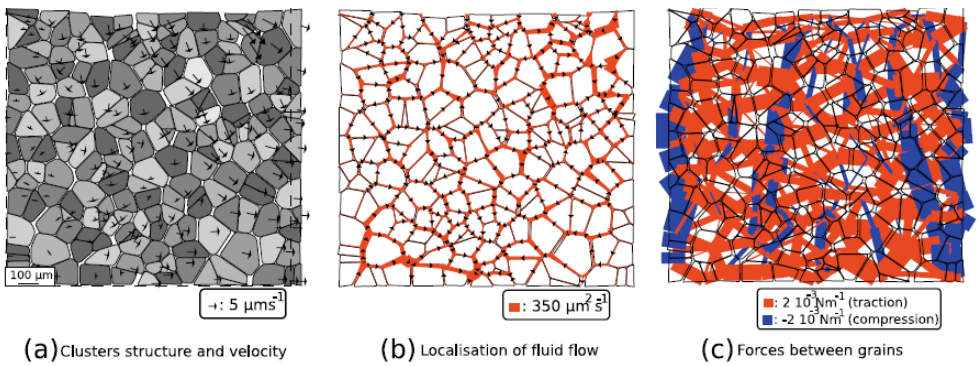

Figure 2.10: Schematic of a 2-D mushy zone at $g_s = 0.92$ subjected to a strain rate of 0.004 s^{-1} [68].

distribution of grains, description of solidification process in the scale of grains remained imperfect due to the 3-D nature of both semi-solid deformation and fluid flow between the grains [69]. In order to address this need, Sistaninia et al. [2] developed a 3-D granular hydro-mechanical model known as GMS-3D to predict hot tearing formation in solidifying alloys. The simulation domain in this model is a Representative Volume Element (RVE), which consists of randomly distributed grains with equiaxed-globular microstructure surrounded by liquid channels. Fig. 2.11 shows the evolution of the semi-solid microstructure during tensile deformation of a notched Al-2wt.%Cu specimen at three different simulation time predicted by GMS-3D. The solid grains, liquid channels, and cracks are colored in gray, white, and dark blue respectively. Fig. 2.12 represents the corresponding X-ray images taken during the experimental trial. Comparing the two figures, it can be concluded that the model offers a good insight into the prediction of hot tearing phenomenon [70, 71].

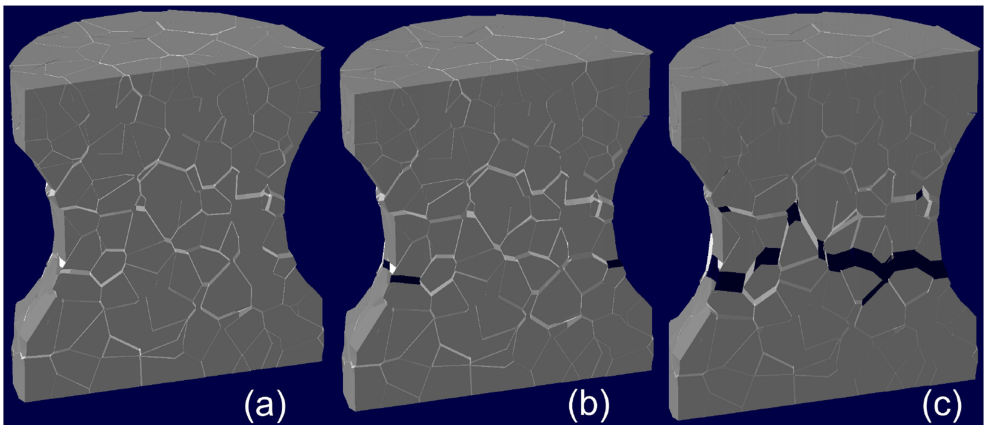

Figure 2.11: Evolution in the semi-solid microstructure during tensile deformation of a notched Al-2wt.%Cu specimen as predicted by GMS-3D at (a) $t = 405$ s, (b) $t = 729$ s, and (c) $t = 1215$ s after the start of the simulation [70].

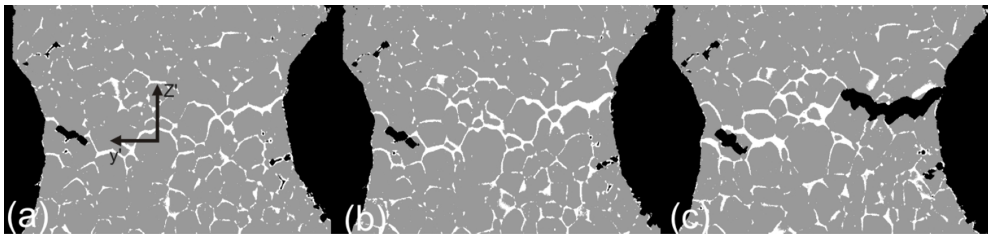

Figure 2.12: X-ray tomography of the cross-section showing the evolution in the semi-solid microstructure during the tensile deformation of a notched Al-2wt.%Cu after (a) $t = 486$ s, (b) $t = 729$ s, and (c) $t = 1215$ s from the beginning of the experiment [71].

2.6 Thermomechanical Modeling of the DC Casting Process

All of the hot tearing criteria and the multi-physics models that have been presented require knowledge of the thermo and mechanical fields experienced by a casting during solidification. In order to acquire this data, a mathematical model for simulating the DC casting process is needed. Since the early 1980s, there have been many efforts to model the DC casting process, which has evolved over the past few years owing to

the progress in computational methods. As discussed in the previous sections, in DC casting, the occurrence of hot tears corresponds to accumulation of tensile thermal stresses exceeding the semi-solid yield point in conjunction with hindered fluid flow at high solid fractions. Therefore, the first step that should be taken to simulate the process is to model the thermal conditions and calculate stress and strain evolution. In this regard, many researchers have focused on thermomechanical models, which account for the coupled thermal and mechanical behaviour of solidifying material using constitutive equations to predict stress and strain evolution within the casting. In thermomechanical models, the effect of fluid flow between the grains is ignored and liquid, solid, and semi-solid states are distinguished from each other by the amount of strength given to each of them. In the next step, a hot tearing criterion is implemented through post-processing calculations to assess hot tearing tendencies.

Thermomechanical models of the DC casting process can be separated into two distinct, but interrelated parts, namely, simulating the thermal conditions and stress state during and after the casting. Most recent models are either implemented in finite element commercial software packages designed for simulation of metal casting processes such as ProCAST, MAGMA, THERCAST, etc. or other software packages such as ABAQUS or ANSYS, which can be used as a platform for solving non-linear heat transfer and mechanical problems. In order to create a thermomechanical process model of DC casting, the problem is required to be addressed in terms of the following:

- Calculation of the domain and geometry
- Thermophysical properties of the material
- Constitutive properties

- Initial and boundary conditions

Extensive work has been performed on modeling the DC casting process. In this regard, Phillion [72] incorporated Pellini's Total Strain and the RDG criterion into a 2-D finite element model of the DC casting of the rectangular ingots to investigate hot tearing susceptibility and validate the aforementioned criteria. Two sets of process parameters, characterized by a change in cooling water flow rate, were used in the DC casting process. Good agreement was found between the industry experience and hot tearing predictions of Pellini's criterion. The RDG criterion was able to differentiate the hot tearing tendency between the start-up phase of two casting recipes with low and high cooling water flow rate.

Suyitno et al. [73], studied the effects of casting speed and alloy composition on hot tearing formation using a thermomechanical finite element simulation of a DC cast round billet combined with experimental work. Then, various hot tearing criteria were applied to evaluate their applicability in comparison with experimental data. The results showed that some criteria such as Clyne and Davies, or Novikov's criteria that their formulation are based on static parameters do not take into account the change in casting speed and are incapable of predicting hot tearing occurrence in different casting conditions. However, Katgerman, Feurer, Prokhorov, and the RDG criteria can qualitatively assess hot cracking tendency. Fig. 2.13 illustrates hot tearing susceptibility predicted by different hot tearing criteria in the vertical cross-section of an Al-Cu billet as well as the variation of the casting speed with the length of the billet. It can be seen that hot tearing tendency predicted by Novikov and Clyne and Davies does not change with casting speed. On the other hand, the sensitivity of hot tearing to casting speed is clearly demonstrated by other criteria such that hot

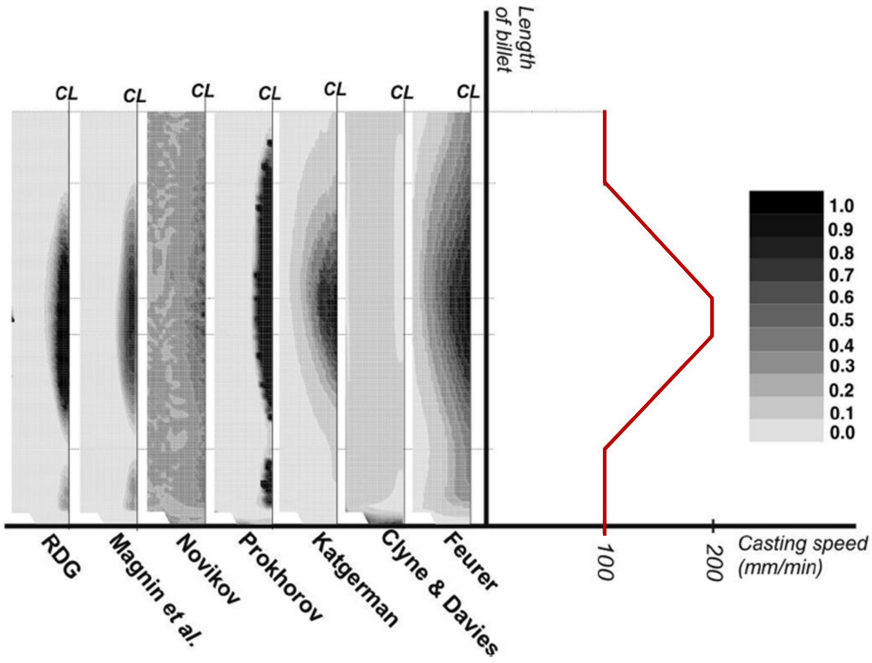

Figure 2.13: Hot cracking susceptibility in the vertical cross-section of an Al-4.5wt% Cu billet computed using different hot tearing criteria for a varying casting speed [73].

tearing tendency is an increasing function of casting speed.

2.7 Summary

In this chapter, after a short definition of the hot tearing defect, the most important mechanisms that explain the reason behind the formation of hot tearing as well as several criteria that predict hot tearing susceptibility were reviewed. The emphasis was then placed on the problem of hot tearing in DC casting of aluminum alloys and how different alloy and processing parameters influence the problem. From the review on the proposed mathematical methods for simulating the DC casting process and

the hot tearing evolution, it can be deduced that a model which investigates the effect of the DC casting process parameters on 3-D liquid feeding and strain localization at grain boundaries and consequently predict hot tearing formation and growth has not yet been proposed. The shortage of research in this area can be explained by what can be seen in Fig. 2.13; although some of the hot tearing criteria can successfully predict hot tearing susceptibility, none of them can exactly quantify whether or not hot tears will occur. In order to quantify hot tearing predictions in the DC casting process, it is required to take advantage of a granular multi-physics model and a thermomechanical model of the DC casting process at the same time.

Chapter 3

Scope and Objectives

As discussed in Chapter 1 and 2, hot tearing is one of the most severe defects encountered in DC casting of aluminum alloys and is intimately linked with the constitutive behavior of the alloy in the semi-solid region. Hot tearing has been widely investigated by various methods both experimentally and numerically. The experimental studies are limited due to the high temperature at which hot tears form and the sensitivity of factors that cause hot tearing to the casting geometry; thus, modeling of the DC casting process at the macroscopic scale has become a popular practice in industry. The limitation of such models is that they do not allow for localization of straining and liquid feeding between the grains that cause hot tearing formation; such phenomena are well addressed in meso-scale models.

The main goal of this research is to couple a macro-scale thermomechanical model of the DC casting process [1] with a meso-scale coupled hydro-mechanical model [74] in order to demonstrate a multi-scale approach for quantifying the severity of hot tears and predict where they occur in the DC cast billet. The first model, which has been developed in the general purpose finite element (FE) software package ABAQUS, is

used to predict the evolution of stress, strain, strain rate, temperature, etc. with time at different locations of the casting for different casting speeds. The second model, which is custom software, predicts the constitutive behavior of a semi-solid considering fluid flow between the grains, percolation, bridging of the solid grains and crack formation. In this model, it is assumed that equiaxed solid grains surrounded by liquid films are randomly distributed in a representative volume element (RVE). This thesis thus develops a bridge linking the macro- and the meso-scale model and explains how two models are coupled together in order to quantify hot tearing predictions.

This work is broken down into the following parts. In Chapter 2, a short review on hot tearing formation as well as the application of numerical models to investigate hot tearing were provided. The theoretical basics of the meso- scale and the macro-scale model as well as the methodology by which the two models are coupled are discussed in Chapter 4. After a brief discussion on the results from the macro- and the meso-scale model, Chapter 5 mainly focuses on the output of the multi-scale model considering different parameters such as strain rate, grain size, feedability of the mushy zone, etc. Finally, some possible future work and conclusions are presented in Chapter 6.

Chapter 4

Numerical Methods

4.1 Introduction

This chapter presents the methodology used in this thesis to investigate the problem of hot tearing in DC casting of aluminum alloys. First, the model utilized to simulate the DC casting process is presented. Here we used a thermomechanical finite element model realized with the general purpose software package, ABAQUS version 2017. This model is based on the models previously developed by Drezet et al. [75] and Jamaly et al. [1] to which the readers are referred for further details and references. The model predicts the evolution of the temperature distribution and displacement field which were validated by thermocouple data obtained from industrial DC casting trials and neutron diffraction measurements, respectively. Second, the coupled hydro-mechanical granular model developed by Sistaninia et al. [76, 70, 2], which consists of four separate segments and their coupling, is explained. The model was validated against synchrotron X-ray tomography results [77]. Henceforward, the first and the second models will be called "the macro-scale model" and "the meso-scale model",

respectively. Finally, the multi-scale approach to hot tearing, which utilizes the output of the macro-scale model to simulate the tensile behavior of the simulation domain at the meso-scale is presented.

4.2 The Macro-scale Model

The DC casting process of a round billet (320 mm diameter $\times$ 800 mm length) is simulated using an axisymmetric geometry as shown in Fig. 4.1. To simplify the problem, the interactions of the billet with the mold and the bottom block are taken into account by applying proper boundary conditions regardless of their geometries. 2-D element type CAX4T (4 mm height $\times$ 5 mm width), which has four integration points and performs coupled temperature-displacement analysis, is used to mesh the computational domain. The increase in the casting height as a result of the downward movement of the bottom block is simulated such that the bottom block and the billet remain in a fixed position and the billet height grows in vertical direction by addition of horizontal layers incrementally. Accordingly, the thermal boundary condition is moving upward at a rate consistent with the casting speed. In order to calculate the evolution of stress, strain, and temperature as a function of position in the billet and time, the solidification and constitutive models are implemented in ABAQUS through the user programmable subroutine UHARD. The material is assumed to be an aluminum AA5182 alloy (composition: Mn 0.35 wt.%-Mg 4.5 wt.%-Al balance), which is widely used for the production of automotive components and beverage cans. The alloy has a large solidification window (T_{sol} = 523 °C and T_{liq} = 637 °C), which makes it susceptible to hot tearing and suitable for this study.

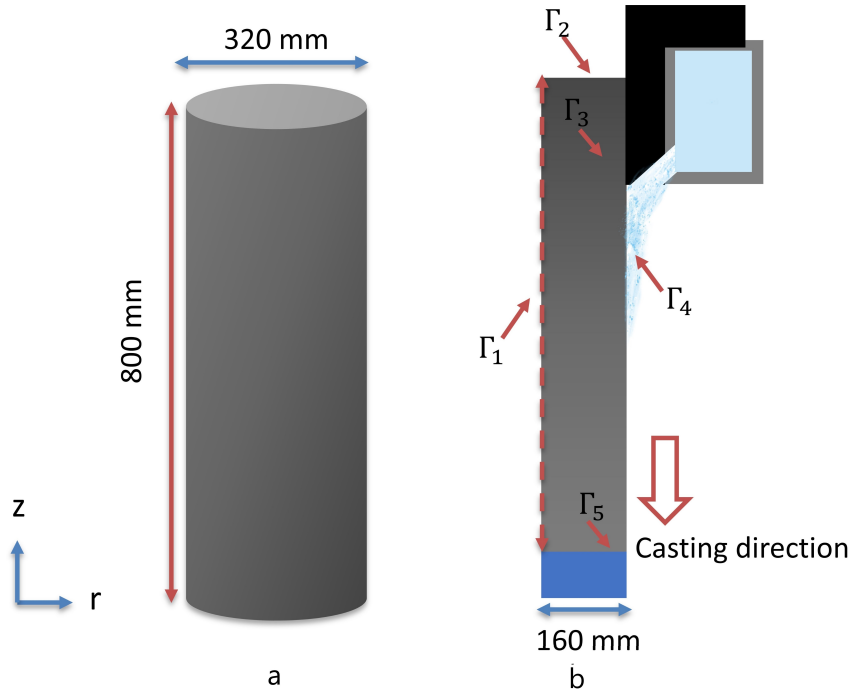

Figure 4.1: Schematic of (a) the actual DC cast billet and (b) the computational domain in the macro-scale model.

4.2.1 Boundary Conditions

It is necessary to apply mechanical boundary conditions to avoid convergence issues associated with rigid body motion. For this purpose, an axisymmetric boundary condition is applied to the axis of rotation ($r = 0$) to restrict the deformation of the centerline in radial direction. In addition, the bottom node at the centreline of the billet is constrained in radial (r) and axial (z) directions to suppress the separation of the bottom block and the billet at the centerline.

In order to solve heat transfer equations in a transient heat transfer problem, it is necessary to specify initial thermal conditions as well as proper thermal boundary conditions. The initial temperature of the layers of elements making up the domain is

set to 650 °C, which is the typical pouring temperature of AA5182 alloy. The ambient temperature is assumed to be 25 °C.

To simplify the simulation, it is assumed that heat transfer is limited to conduction while the effect of radiation is neglected. The heat is not extracted from the boundary Γ_1 in $-r$ direction due to the axial symmetry and from the boundary Γ_2 in z direction due to the use of a "hot top" in industry. In order to address heat transfer from the surface of the billet and the bottom, Cauchy type boundary conditions were applied to surfaces of the billet in contact with the mold (Γ_3), cooling water (Γ_4), and the bottom block (Γ_5), meaning that the heat flux from the billet to the surrounding environment is dependent on both the surface and surrounding temperature and is defined as:

$$q = h(T - T_\infty), \tag{4.1}$$

where q is the heat flux, h is the heat transfer coefficient, T is the surface temperature, and T_∞ is the ambient temperature. It is essential to know the value of the heat transfer coefficient in the calculations. When the surface of the billet solidifies within the mold, it shrinks and consequently loses its thermal contact with the mold. Therefore, at the boundary Γ_3, the heat transfer coefficient is dependent on the gap distance between the mold and the billet and is assumed to vary as a function of the volume fraction of solid (g_s) and is given by:

$$h_{\Gamma_3} = h_{contact}(1 - g_s) + h_{gap} \times g_s, \tag{4.2}$$

where $h_{contact} = 2000$ W.m^{-2}.K^{-1} and $h_{gap} = 50$ W.m^{-2}.K^{-1} are the heat transfer coefficients corresponding to $g_s = 0$ and $g_s = 1$, respectively. At the boundary Γ_5, the

heat transfer coefficient is assumed to be constant and equals to 1000 $W.m^{-2}.K^{-1}$. The solid fraction-temperature curve is taken from Ref. [78] and is shown in Fig. 4.2.

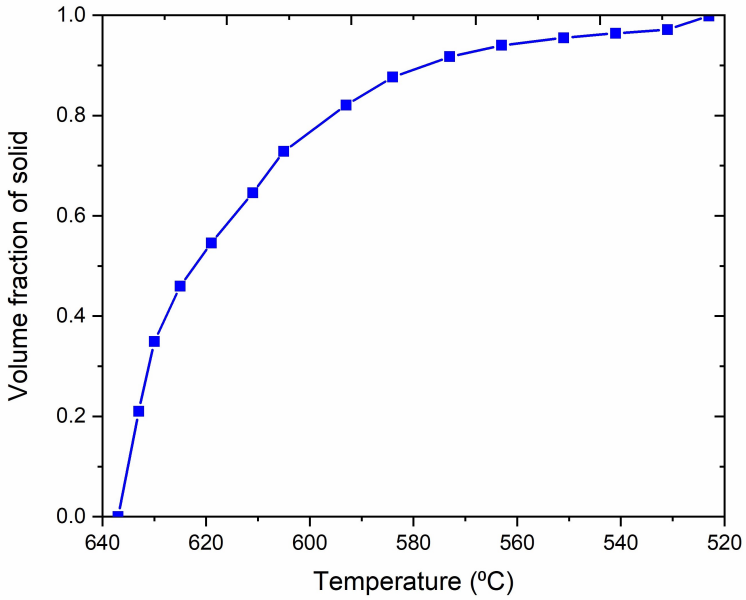

Figure 4.2: Solidification path of AA5182 used in the macro-scale model [78].

4.2.2 Materials Data

In order to perform a fully coupled thermomechanical analysis, it is required to determine different thermal and mechanical properties of the AA5182 alloy as a function of temperature by taking into account the transition temperatures, i.e. the liquidus temperature (T_{liq}), the mechanical coalescence temperature (T_{coh}), and the solidus temperature (T_{sol}). Including the mechanical coalescence temperature in the calculations is of importance as it is known to be the temperature at which the semi-solid

materials starts developing strength and exhibits contraction. In this work, the temperature for mechanical coalescence is considered to be 602 °C which corresponds to solid fraction of 0.75. Thermophysical properties of the AA5182 alloy were taken from Ref. [79] and are given in Table 4.1. Linear interpolation is used to calculate the material properties at intermediate temperatures. Moreover, since the fluid flow is ignored in this model, in order to consider the heat transfer due to the fluid flow in the liquid sump, the thermal conductivity is increased four times its actual value for temperatures above the liquidus. Moreover, the density is treated as constant to maintain the heat balance of the system.

Table 4.1: Thermophysical properties of AA5182 alloy used in the macro-scale model [79]

Property	**Temperature range (°C)**	**Value**
Thermal Conductivity ($W.m^{-1}.K^{-1}$)	$T < T_{coal}$	$119.2 + 0.623T$
	$T_{coal} \leq T \leq T_{liq}$	$594 - 0.484T - 0.00048T^2$
	$T > T_{liq}$	$69 + 0.033T$
Specific Heat ($J.kg^{-1}.K^{-1}$)	$T < T_{coal}$	$897 + 0.452T$
	$T_{coal} \leq T \leq T_{liq}$	$-994.8 + 8T - 0.0074T^2$
	$T > T_{liq}$	1097
Latent Heat ($kJ.kg^{-3}$)	N/A	397.1
Density ($kg.m^{-3}$)	N/A	2400

The Young's modulus (E) for deformation in the elastic region, coefficient of thermal expansion (α), and Poisson's ratio are also taken from Ref. [79] and are shown in Table 4.2. As can be calculated from the data presented in that table, the Young's modulus (E) changes from 71 GPa at room temperature ($T_{25^\circ C}$) to 10 GPa at solidus temperature (T_{sol}). Then, for computational purposes, the Young's modulus

was set to a small value of 0.01 GPa above the mechanical coalescence temperature ($T \geq T_{coal} + 10$) to eliminate the stress development in the mushy zone at lower solid fractions.

Table 4.2: Mechanical properties of AA5182 used in the macro-scale model [79]

Property	**Temperature range (°C)**	**Value**
E (GPa)	$T_{25^\circ} < T < T_{sol}$	$-0.162T^2 + 7.52T + 71589$
	$T_{sol} < T < T_{coal}$	$100.836 - 0.174T$
	$T \geq T_{coal} + 10$	0.01
α ($^\circ$ K^{-1})	$T \leq T_{coal}$	$-0.0235 + 2 \times 10^{-5}T + 4 \times 10^{-8}T^2$
	$T > T_{coal}$	0
Poisson's ratio	N/A	0.3

4.2.3 Constitutive Models

In order to describe the inelastic behavior of the alloy or in other words simulate the the mechanical response (σ) of the billet to deformation (ε), different constitutive laws depending on the temperature are used.

For the constitutive model of the solid metal, plastic deformation is described by a modified Ludwik equation developed by Alankar and Wells [80], which takes into account not only the time-independent plastic behavior at low temperatures but also the viscoplastic behavior of the solid at higher temperatures as it includes temperature dependent parameters:

$$\sigma(T, \varepsilon, \dot{\varepsilon}) = K(T)(\varepsilon_p + \varepsilon_{p_0})^{n(T)}(\dot{\varepsilon_p} + \dot{\varepsilon}_{p0})^{m(T)}, \tag{4.3}$$

where σ is the stress, K is the material's constant related to the strength of the material, n is the strain hardening coefficient, m is the strain rate sensitivity coefficient, $\dot{\varepsilon_p}$ is the equivalent plastic strain rate, and ε_p is the total plastic strain at temperatures below 400 °C. It is assumed that at temperatures higher than 361 °C there is no strain hardening and the flow stress is only dependent on temperature and strain rate. $\varepsilon_{p_0} = 10^{-6}\ s^{-1}$ and $\dot{\varepsilon}_{p0} = 10^{-4}\ \mathrm{s}^{-1}$ are constants with small values used to avoid numerical convergence issues in ABAQUS. The trendline equations of n, m and K parameters for AA5182 alloy are given in Table 4.3.

Table 4.3: Parameters of the modified Ludwik equation [80]

Parameter	**Temperature range (°C)**	**Value**
K (MPa)	$25 \leq T < 331$	$-0.3409T + 361.83$
	$331 \leq T \leq 500$	$-1.1015T + 613.59$
n	$25 \leq T < 206$	$-0.0003T + 0.170$
	$206 \leq T < 361$	$-0.0007T + 0.252$
	$361 \leq T \leq 500$	0
m	$25 \leq T < 183$	0
	$183 \leq T < 361$	$0.001T - 0.183$
	$361 \leq T \leq 500$	$0.0003T + 0.069$

For the constitutive equation between the solidus temperature (T_{sol}) and the mechanical coalescence temperature (T_{coal}), a model proposed by Phillion et al. [81], which includes the effects of grain size on the stress–strain predictions, is used:

$$\sigma(g_s, g_p, d) = g_s \sigma_s (\varepsilon_p + \varepsilon_0)^{n_{ss}(T)}, \tag{4.4}$$

$$\sigma_s = (483.5 - 0.77T)\dot{\varepsilon_p}^{(0.205+0.00006T)}, \tag{4.5}$$

$$h = d(1 - g_s)^{\frac{1}{3}}, \tag{4.6}$$

$$n_{ss} = -6.35e^{-4}h^2 + 0.0202h, \tag{4.7}$$

where σ is the total flow stress, g_s is the volume fraction of solid, σ_s is the solid flow stress, ε_p is the total plastic strain, ε_0 is the initial strain such that $\sigma(\varepsilon_p = 0) = \sigma_{yield}$, n_{ss} is a strain hardening parameter, $\dot{\varepsilon_p}$ is the equivalent plastic strain rate, T is the temperature, h is the thickness of the liquid channels between the grains, and d is the grain size. The expression for n_{ss} was derived from regression analysis of semi-solid tensile deformation experiments and microstructure simulation. As can be seen in Fig. 4.3 and Fig. 4.4, which illustrate the effect of solid fraction and grain size on the predicted stress-strain relationships for AA5182 alloy, by increasing the solid fraction and decreasing the grain size, semi-solid strength will increase.

In order to calculate the thickness of the liquid channels between the grains (h), the value of the grain size is needed. For this purpose, the methodology developed by Easton et al. [82] is used to estimate the grain size by considering the cooling rate and solute content as controlling parameters. The effect of solute content is quantified by introducing the growth restriction factor (Q), which is approximated for an alloy as:

$$Q = \sum_i m_i \; c_{0,i}(k_i - 1), \tag{4.8}$$

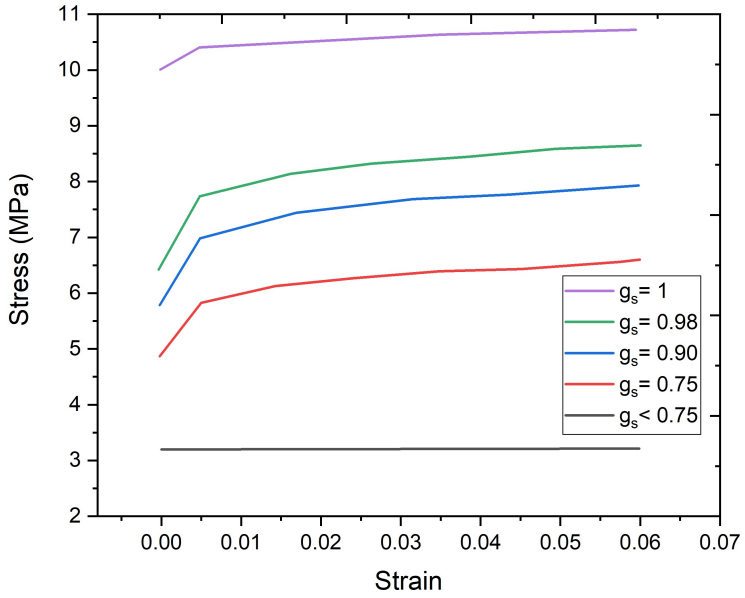

Figure 4.3: Schematic of semi-solid stress-strain response used in the simulation at various solid fractions for the grain size of 150 μm, and strain rate of 10^{-3} s^{-1}.

where for each element, m_i is the liquidus gradient, $c_{0,i}$ is the composition, and k_i the binary partition coefficient for each element in the alloy. Table 4.4 shows the data required to calculate the growth restriction factor.

Table 4.4: Data for calculating Q [83]

Element	$m(k-1)$ (K)
Ti	220
Mn	0.1
Mg	3

Assuming the alloy is cast after the addition of 0.005 wt% TiB_2 as a grain refiner,

the grain size (d) is given by:

$$d(\mu m) = \frac{1}{1.4(1 - e^{-0.569\dot{T}^{0.685}})[\mathrm{TiB_2}]^{1/3}} + (281 + \frac{381}{\dot{T}^{0.5}})\frac{1}{Q}. \tag{4.9}$$

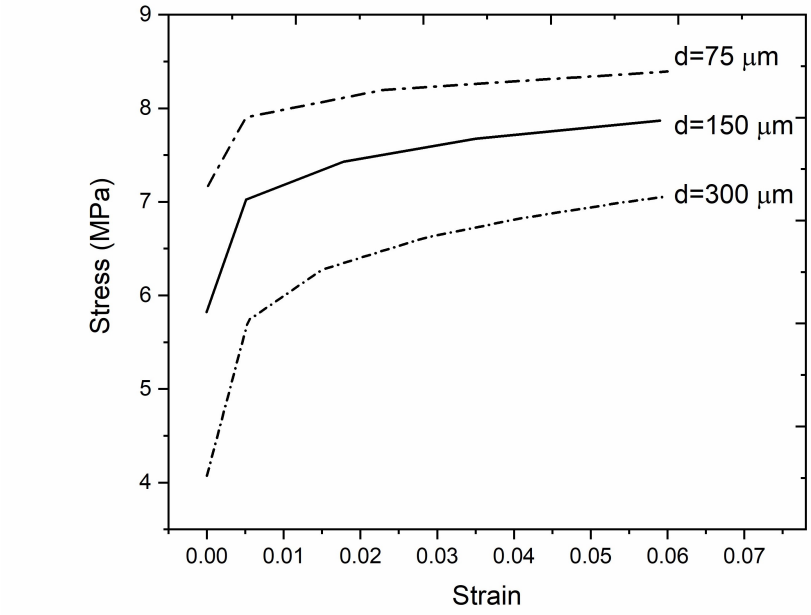

Figure 4.4: Schematic of semi-solid stress-strain response used in the simulation for various grain sizes at solid fraction of 0.98 and strain rate of 10^{-3} s^{-1}.

As can be seen in Table 4.3 , Eq. 4.3 is only valid for the temperature range of $25 - 500$ °C and Eq. 4.4 is valid for the temperature range of $T_{sol} - T_{coal}$; thus, the constitutive behavior used between $T = 500$ °C and $T_{sol} = 523$ °C is derived by linear interpolation between values of Eq. 4.3 and Eq. 4.4 at 500 °C and 523 °C, respectively. At temperatures above the T_{coal}, it is considered that the material exhibits an ideal plastic behavior as shown in Fig. 4.3.

The macro-scale model is able to predict the evolution of temperature, stress, strain, strain rate, etc. as a function of time within the DC cast billet. With the aid

of this model, the steady state and start-up regions can be identified through the temperature field and stress predication in vertical direction. Moreover, the simulation results can be used as input to calculations of different hot tearing criteria. Although the model was validated against thermal measurment data obtained from industrial DC casting trails and neutron diffraction measurements, simplifying assumptions can alter the results. The most important assumptions of this model which can affect the prediction of hot tearing are summarized as the ignorance of fluid flow and macrosegregation, the use of invariant solidification path, consideration of a constant heat transfer coefficient at the bottom block of the billet and simplification of heat transfer through cooling water sprays bellow the mold.

4.3 The Meso-scale Model

The mechanical behavior and liquid feeding of the semi-solid alloy during the DC casting process is described with the aid of a 3-D coupled hydro-mechanical granular model. The model consists of four different segments. (1): The solidification segment to create the solid-liquid geometry at any solid fraction. (2): The fluid flow segment for simulation of liquid pressure within the intergranular channels. (3): The semi-solid deformation segment to model the semi-solid mechanical behavior and finally (4): the failure segment to simulate crack initiation and propagation. Since hot tearing formation is the result of both lack of liquid feeding and deformation of alloy in the semi-solid region, the fluid flow segment, semi-solid deformation segment, and the failure segment are linked together using a coupling method between them. In the following each segment and the coupling method is presented.

4.3.1 Solidification Segment

The 3-D granular solidification model known as 3D-GMS [84] is used to generate the solid-liquid geometry based on Voronoi tessellation of randomly distributed nucleation centers. The geometry is assumed to be a representative volume element (RVE) of equiaxed globular grains with liquid channels in between as shown in Fig. 4.5 (a). To perform solidification calculations, each grain is divided into pyramids as illustrated in Fig. 4.5 (b) and (c). The summit of the pyramid is considered to be the nucleation center and its facet to be the base. The pyramid is further broken down into tetrahedral elements as illustrated in Fig. 4.5 (d). The solidification within each tetrahedron is reduced to a one-dimensional problem assuming infinite diffusion in the liquid and back diffusion in the solid. The evolution of the solid-liquid interface in each tetrahedron is given by:

$$v^* x^{*^2}(k_0 - 1)C_l + \frac{1}{3}(L^3 - x^{*^3})\frac{\dot{T}}{m_l} + x^{*^2} D_s \frac{\partial C_s}{\partial x\ |_{x^*}} = 0, \tag{4.10}$$

where v^* and x^* are the velocity of the interface and its actual position, k_0 is the partition coefficient, C_l and C_s are the compositions of the liquid and the solid, L is the height of the tetrahedron measured from the nucleation center, $\dot{T}$ is the cooling rate, m_l is the liquidus gradient, and D_s is the diffusion coefficient in the solid.

The evolution of the term $\frac{\partial C_s}{\partial x}\ |_{x^*}$ can be determined if one solves the diffusion equation in the solid phase:

$$\frac{\partial C_s}{\partial t} = D_s(\frac{\partial^2 C_s}{\partial x^2} + \frac{2}{x}\frac{\partial C_s}{\partial x}). \tag{4.11}$$

At high solid fractions, neighboring grains come into contact with each other and

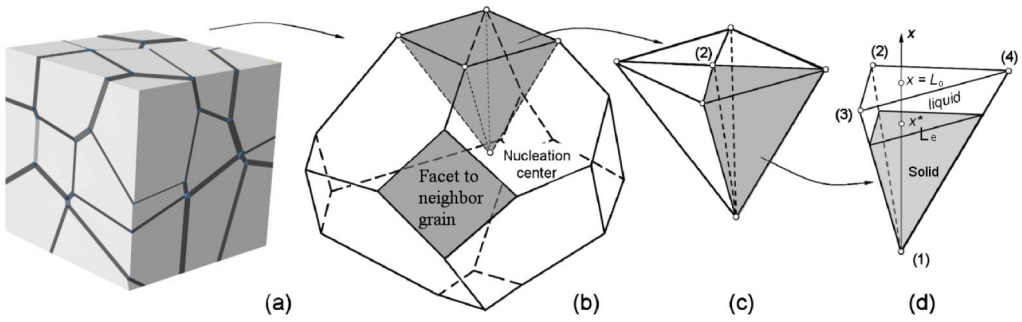

Figure 4.5: A breakdown of the RVE representing solid-liquid geometry in 3-D; (a) the entire model domain, (b) a polyhedral grain, (c) a pyramid volume element, and (d) a single tetrahedral element showing both the solid portion (gray) and liquid portion (clear) [84].

bridge. It is required for the model to use a coalescence criterion to decide which neighboring grains are going to coalesce. In this regard, the minimum surface energy criterion developed by Rappaz et al. [85] is implemented in which a random orientation angle between 0° and 90° is assigned to each grain and then the misorientation angle for two neighboring grains is calculated from $\Delta\theta = \theta_1 - \theta_2$, where θ_1 and θ_2 are the assigned angles and $\Delta\theta$ is the misorientation angle, which is translated to the energy of grain boundary according to available data in the literature [86, 87]. It is assumed that if $\Delta\theta$ is greater than 10°, the energy of grain boundaries (γ_{gb}) will be greater than the energy of solid-liquid interface ($2\gamma_{sl}$); therefore, the boundary of two neighboring grains is repulsive and a coalescence undercooling (ΔT_b) is needed to provide the driving force for coalescence:

$$\Delta T_b = \frac{\gamma_{gb,max} - 2\gamma_{sl}}{\Delta S_f} \frac{1}{\delta_{sl}}, \tag{4.12}$$

where ΔS_f is the entropy of fusion per unit volume, δ_{sl} is the diffuse solid-liquid interfacial thickness, and γ_{gb} is a value between 0 and $\gamma_{gb,max}$.

4.3.2 Fluid Flow Segment

During the course of solidification, liquid convection in channels between the grains occurs because of volumetric shrinkage as a result of phase transformation and mechanical deformation. The geometry used in fluid flow calculation is derived from the solidification segment and consists of prismatic grains and the flow is assumed to occur in direction parallel to polyhedral facets as shown in Fig. 4.6. In other words, if one considers a local frame (x', y', z') attached to the base of a the prismatic element, with the local z' axis perpendicular to the base surface, fluid velocity has only two dimensions, i.e. $v_{lx'}$ and $v_{ly'}$. In addition, assuming that the liquid density is constant and the flow is irrotational in the facet, a simplified form of Navier-Stokes equation can be used to formulate the fluid flow between two parallel grain:

$$\vec{v_l} = \frac{1}{2\mu_l}\vec{\nabla} p_l[z'^2 - h^2], \tag{4.13}$$

where $\vec{v_l}$ is the fluid velocity vector, μ_l is the dynamic viscosity, p_l is the pressure, h is the half of the liquid channel width, and the reference node of the local frame (x', y', z') is located in the half width of the liquid channel. If one combines Eq. 4.13 with mass conservation equation, and takes into account the variation of the liquid density, the liquid pressure can be found from:

$$\frac{2h^3}{3\mu_l}\nabla^2 p_l = 2\beta v^* + \Delta v_{sn} + \frac{2h}{K_l}\frac{\partial p_l}{\partial t}, \tag{4.14}$$

where $\beta = (\rho_s/\rho_l - 1)$ is the shrinkage factor, Δv_{sn} measures the difference between normal velocity of solid grains, i.e. $v^+_{sz'} - v^-_{sz'}$ and K_l is the bulk module of the liquid,

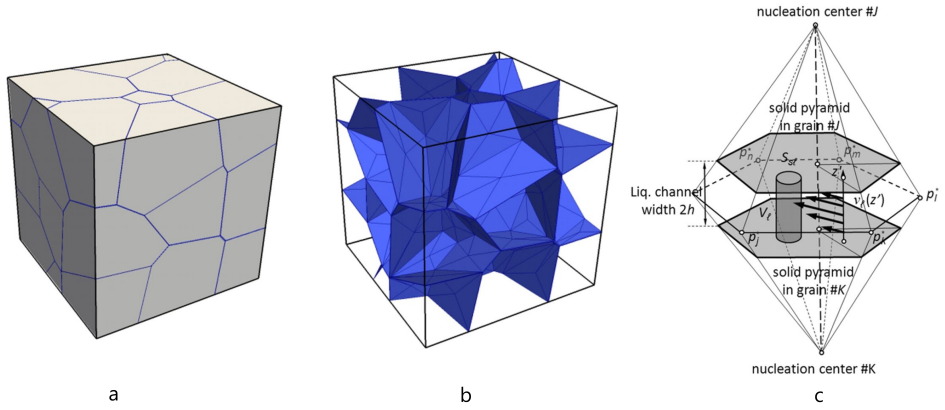

Figure 4.6: (a) The domain of the granular semi-solid model containing 27 ($3 \times 3 \times 3$) grains, (b) the network of the triangular liquid elements in between the polyhedral grains, and (c) a schematic of the liquid control volume and its location in relation to the facets of two neighboring grains.

which links the variation of the liquid density to liquid pressure drop:

$$\frac{1}{\rho_l}\frac{\partial \rho_l}{\partial t} = \frac{1}{K_l}\frac{\partial p_l}{\partial t}. \tag{4.15}$$

The left-hand side of Eq. 4.14 provides the variation in the liquid pressure drop required to account for the effect of solidification shrinkage and the solid deformation in the right-hand side. In order to calculate the liquid pressure in the semi-solid RVE, a finite element code using a free open-access program C++ template library known as IML++ has been written to solve Eq. 4.14.

4.3.3 Semi-solid Deformation Segment

The semi-solid deformation segment accounts for the distribution of strain between the grains and utilizes the output of the solidification segment, i.e. a set of solid tetrahedral elements, which are in solid contact with three other tetrahedrons of the

same grain. The fourth facet of the tetrahedral elements is either in solid contact with the facet of the neighboring grain after the coalescence or is separated from that by a liquid channel existing in between prior to coalescence. With the use of a C++ subroutine, a finite element mesh as well as an ABAQUS control file for performing the semi-solid deformation simulation based on the viscoplastic Ludwik's equation are created from the output of solidification segment:

$$\sigma(\varepsilon, \dot{\varepsilon}, T) = k_s(T)\varepsilon^{n(T)}\dot{\varepsilon}^{m(T)}. \tag{4.16}$$

The finite element mesh divides each solid tetrahedron into three solid elements, namely, a tetrahedral and a two pentahedral solid elements. Multi points constraint (MPC) elements are used to conserve the continuity of two neighboring tetrahedrons in a grain. Contact elements are located at the solid-liquid boundary of each grain to prevent the penetration of grains and the effect of hydrostatic pressure within the liquid is simulated by adopting link-spring elements with a negligible stiffness coefficient. With the aid of the semi-solid deformation segment, the overall stress-strain behavior of the RVE is predicted.

4.3.4 Failure Segment

It is required to apply a hot tearing criterion to the model to capture crack initiation and propagation. The criterion used in this model is based on the Young-Laplace equation for growing voids which takes into account the overpressure needed to overcome capillary forces at the interface of the atmosphere and the liquid as shown in

Fig. 4.7 and is defined as:

$$p_a - p_l = \frac{\lambda \cos\theta}{h}, \tag{4.17}$$

where p_a is the atmospheric pressure, p_l is the liquid pressure, λ is the surface tension at the void-liquid interface, $\cos\theta$ is the dihedral angle, and h is the half width of the liquid channel. According to the measurements made by Syvertsen [88], the value λ has been set to 5 J.m^{-2} in this simulation. Hence, the crack initiation occurs if the following assumption is valid:

$$p_l \leq p_a - \frac{5}{h}\,[Pa]. \tag{4.18}$$

Once the crack initiates, the crack propagates abruptly in the liquid channel con-

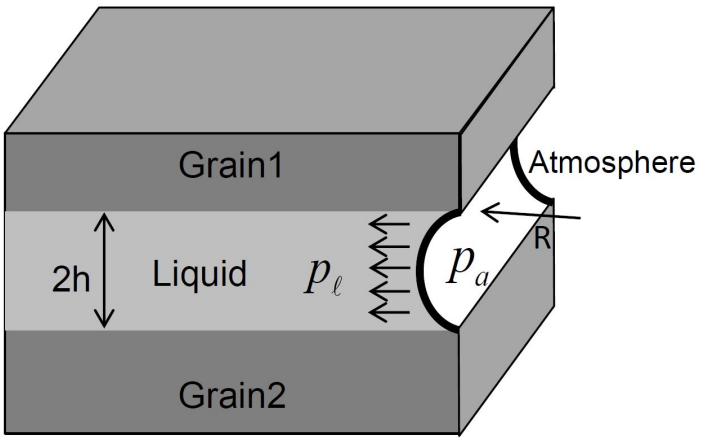

Figure 4.7: Schematic representation of crack initiation in the liquid channel located in between two solid grains.

nected to the tip of the crack. Therefore, a higher liquid pressure satisfies the condition for the crack propagation:

$$p_l \leq p_a - \frac{2}{h}\,[Pa]. \tag{4.19}$$

4.3.5 Hydro-mechanical Coupling

The semi-solid geometry is generated at a given solid fraction for a certain number of grains and a constant grain size in the solidification segment. An initial value for the liquid pressure, i.e. p_l^0 is assumed and based on the applied bulk strain rate, the imposed displacement, $\Delta u_v = \dot{\varepsilon_v} L \Delta t$ (where L is the dimension of the RVE, and $\dot{\varepsilon}_v$ is the bulk strain rate), is calculated and translated into ε_z' in the semi-solid deformation segment. With this information, a deformation simulation is performed in order to determine the velocity of each grain and the resulting change in the liquid channel size. Using these new Δv_{sn} and $2h$, the new p_l is calculated in the fluid flow segment and compered to its initial value (p_l^0). If $|p_l - p_l^0| > Tol$ (where Tol is a tolerance value), p_l^0 is replaced by p_l and the calculations are repeated until the pressure values converges, meaning that $|p_l^{n+1} - p_l^n| < Tol$. When the convergence is attained, the p_l value is compared to the pressure required to satisfy the failure criterion. If the comparison shows that a hot tear has formed, p_l in that channel will be set to p_a for the calculations in the semi-solid deformation segment because with crack formation in a channel, its liquid is sucked into other regions of the RVE and the displacement of $-2h$ is considered for that channel in the next increment, which means that channel will not be participated in fluid flow and deformation calculations in the next increments. The list of physical parameters used in the meso-scale model

is given in Table 4.5.

Table 4.5: List of parameters used in the calculations of the meso-scale model [74]

Parameter	**Value**	**Parameter**	**Value**
ρ_l	2440 kg.m^{-3}	μ_l	0.0015 Pa.s
K_l	41 GPa	β	0.08
ΔS_f	1.02×10^6 J.K^{-1}.m^{-3}	p_m	0 Pa
D_s	1.5×10^{-13} m^2.s^{-1}	D_l	3×10^{-9} m^2.s^{-1}
$\gamma_{gb,max}$	0.324 J.m^{-2}	γ_{sl}	0.092 J.m^{-2}
m	0.164	n	0.22
k_s	30.5 MPa.s$^{\mathrm{m}}$	k_0	0.1
m_l	-20 K/at.%	C_0	0.5 at.%

The meso-scale model is able to predict the overall response of a semi-solid RVE at high solid fraction to an applied strain while considering the liquid feeding and localization of straining between the grains. Moreover, it can predict the crack formation as a result of inability of the liquid to feed the deformation. The simulated stress-strain predictions show a good correlation with the experimental data available in the literature for Al-2wt.%Cu [86].

4.4 Multi-scale Approach to Hot Tearing

The idea behind this thesis is to couple the evolution of thermal and mechanical field throughout the casting provided by the macro-scale model with the ability of the meso-scale model to predict crack formation in a semi-solid RVE. To this end, the following steps as outlined in Fig. 4.8 are taken:

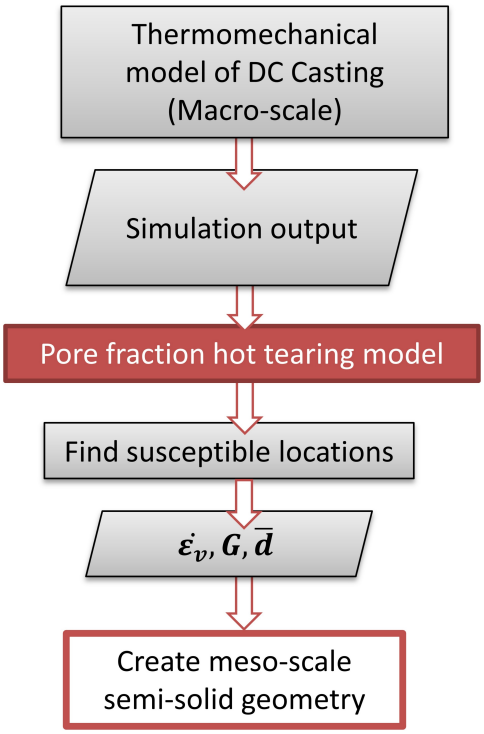

Figure 4.8: Flow chart of the multi-scale approach.

1. Using the macro-scale model, different simulations with variable casting speed have been performed. The simulation output provides the evolution of temperature, cooling rate, thermal gradient, grain size, and different states of stress and strain.

2. In order to assess the hot tearing susceptibility of different regions within the DC cast billet, a hot tearing criterion named "pore fraction hot tearing model" is implemented through post-processing calculations at $T = 546$ °C corresponding to solid fraction of 0.98, where the alloy has neither the strength of the fully solid material nor the ductility in lower solid fractions to accommodate stresses

and strains.

3. The most susceptible locations to hot tearing according to the pore fraction model are found. Then, the characteristics of those locations including grain size (d), thermal gradient (G), and bulk strain rate ($\dot{\varepsilon}_v$), are extracted from the macro-scale model.

4. The information extracted from the previous step is used to run the meso-scale model at solid fraction of 0.98 to simulate the tensile behavior of an RVE during the DC casting process and consequently predict hot tearing formation.

4.4.1 Application of The Pore Fraction Model

As discussed before, several controlling parameters, namely, casting speed, cooling water flow rate, melt temperature and casting geometry influence the quality of the DC cast billets. Among these parameters, the effect of casting speed on the severity of hot tearing formation will be investigated in this work. For pursuing this objective, three casting simulations with different casting speeds are performed at the macroscopic scale. In order to investigate the susceptibility of different regions within the billet to hot tearing, it is required to use a hot tearing criterion. The hot tearing criterion used in this work is pore fraction hot tearing model previously proposed by Monroe and Beckermann [62] and later developed by Dou et al. [89]. Fig. 4.9 shows a 2-D element in the mushy zone of the DC cast billet. Considering the direction of V_{lx} for the thermal gradient, one can assume that fluid moves in direction parallel with the thermal gradient, but solid deformation can occur in directions either perpendicular to or parallel with the thermal gradient, i.e. the directions $V_{s,y}$ and $V_{s,x}$, respectively. As discussed in Chapter 2, Monroe and Beckermann only considered

the defamation of the mushy zone in direction perpendicular to the thermal gradient in their criterion. However, Dou et al. [89] has extended their work by taking into account the deformation of the mushy zone in both directions parallel with and perpendicular to the thermal gradient. In this model, it is considered that the fluid flow ceases at liquid fraction of 0.2 and further shrinkage and deformation after that cause porosity formation. By applying mass conservation, the fraction of porosity that forms as a result of shrinkage ($f_{p,sh}$), deformation in either parallel ($f_{p,de,\varepsilon x}$) or perpendicular to the thermal gradient ($f_{p,de,\varepsilon y}$) can be defined as:

$$f_{p,sh} = \frac{\beta}{\beta + 1} f_{l,cr}, \tag{4.20}$$

$$f_{p,de,\varepsilon x} = \frac{\dot{\varepsilon}_{px} \Delta T_f}{\dot{T}} \int_0^{f_{l,cr}} (1 - f_l) \frac{d\theta}{df_l} df_l, \tag{4.21}$$

$$f_{p,de,\varepsilon y} = \frac{\dot{\varepsilon}_{py} \Delta T_f}{\dot{T}} \int_0^{f_{l,cr}} (1 - f_l) \frac{d\theta}{df_l} df_l, \tag{4.22}$$

where β is the solidification shrinkage, $f_{l,cr}$ is the critical liquid fraction, $\dot{\varepsilon}_{py}$ is the strain rate perpendicular to the thermal gradient, $\dot{\varepsilon}_{px}$ is the strain rate parallel with the thermal gradient, ΔT_f is the freezing range, $\dot{T}$ is the cooling rate, and θ equals $\frac{T - T_{sol}}{\Delta T_f}$.

In order to examine the susceptibility of the DC cast billet to hot tearing with the aid of the pore fraction model, first, using a Python code, cooling rate ($\dot{T}$), the strain rate parallel to the thermal gradient ($\dot{\varepsilon}_{px}$), and the strain rate perpendicular to the thermal gradient ($\dot{\varepsilon}_{py}$) are extracted from the results of the macro-scale model at $T =$ 546 °C corresponding to solid fraction of 0.98. Second, a C++ code is implemented

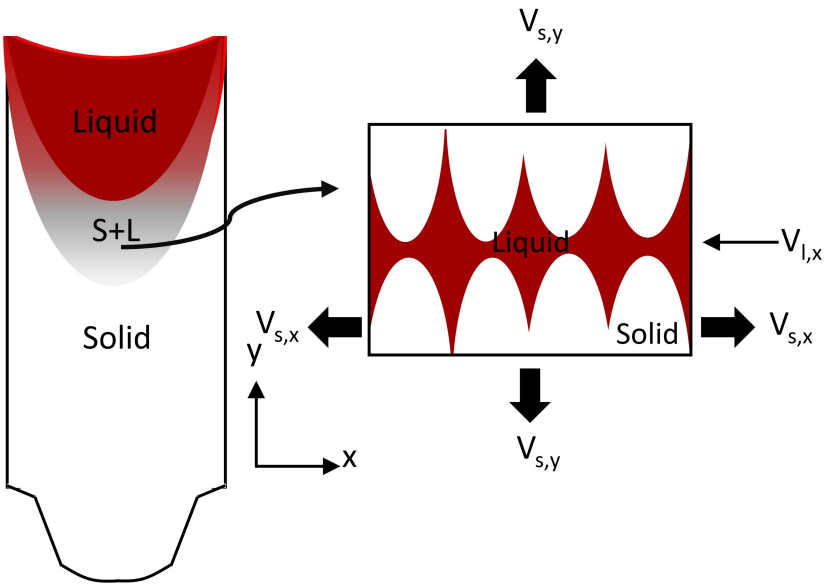

Figure 4.9: Schematic of a DC cast billet and a 2-D domain of the semi-solid region.

to calculate various pore fractions in the DC cast billet. For the calculation of $\dot{\varepsilon}_{px}$ and $\dot{\varepsilon}_{py}$, it is required to rotate the strain rate tensor from the global axi-symmetric coordinate system to the local system aligned with the thermal gradient:

$$A = R \times \dot{\varepsilon}_{ij} \times R', \tag{4.23}$$

$$R = \begin{bmatrix} cos(\frac{\pi}{2} - \gamma) & sin(\frac{\pi}{2} - \gamma) \\ -sin(\frac{\pi}{2} - \gamma) & cos(\frac{\pi}{2} - \gamma) \end{bmatrix}, \tag{4.24}$$

where A is the strain rate in the local coordinate, R is the transformation matrix, R' is the transpose matrix of R, $\dot{\varepsilon}_{ij}$ is the strain rate tensor in the global coordinate, and γ is the rotation angle between the x-axis and the direction of the thermal gradient. $A_{11} + \dot{\varepsilon}_H$ (where is $\dot{\varepsilon}_H$ is the hoop strain rate) is considered as $\dot{\varepsilon}_{py}$ and $\dot{\varepsilon}_{px}$ is given by A_{22}.

4.4.2 Application of The Meso-scale Model

After finding the characteristic of locations within the billet with the highest susceptibility to hot tearing, i.e. the grain size (d), thermal gradient (G), and bulk strain rate ($\dot{\varepsilon}_v$), the semi-solid geometry can be created to simulate the condition experienced by an RVE of grains during the DC casting process. For this purpose, it is necessary to assign proper fluid and mechanical boundary conditions on all surfaces of the RVE in the meso-scale model. Fig. 4.10 shows a schematic of an RVE at solid fraction of 0.98. In terms of mechanical boundary conditions, it is considered that symmetry boundary conditions are assigned to the surfaces $x = 0$, $y = 0$, and $z = 0$. The surface $x = L_x$ is joined to a reference node, which is moved with a constant bulk strain rate found from the macro-scale model, and the surfaces $z = L_z$ and $y = L_y$ are free to move.

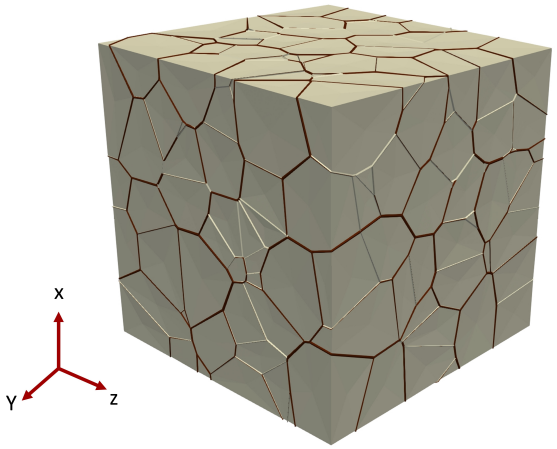

Figure 4.10: Schematic of a representative volume element (RVE) at solid fraction of 0.98.

During the DC casting process, as a result of molten metal convection in the casting, the fluid flows in between the intergranular regions. Therefore, Robin boundary

condition is imposed on the surface $x = 0$, which assumes that the RVE is fed by fluid with a constant feeding coefficient as follows:

$$q_l = f_l(p_l - p_m), \tag{4.25}$$

where q_l is the microscopic flux with the unit of μm.s^{-1}, p_l is the liquid pressure and p_m is the metallostatic pressure. It has been shown by Sistaninia et al. [70] that the feeding coefficient, f_l, can be defined as:

$$f_l = \frac{q_l}{p_l - p_m} = \frac{1}{\int_{T_l}^{T} \frac{\mu_l(1-g_s(T))}{K(g_s)G} dT}, \tag{4.26}$$

where μ_l is the liquid viscosity, G is the thermal gradient and K is the permeability of the mushy zone which is found from the Carman-Kozeny relation [90]:

$$K = \frac{(1-g_s)^3}{5S_v^{sl\,2}}, \tag{4.27}$$

where S_v^{sl} is the intrinsic specific solid-liquid interfacial area. Finally, the other surfaces of the RVE are considered to be closed to fluid flow.

4.5 Summary

In this chapter, the details of the two numerical models, i.e. the thermomechanical model of the DC casting process (the macro-scale model) and the 3-D coupled hydro-mechanical granular model (the meso-scale model) as well as the approach for coupling them were explained. The novelty of this master's thesis is the simultaneous study of a macro-scale process (DC casting) and a micro-scale phenomenon (hot tearing) by

addressing each problem in its own scope. In the next chapter, the presented tools will be outlined to provide a valuable insight into the simulation of hot tearing during the DC casting process.

Chapter 5

Results and Discussion

5.1 Introduction

After the detailed description of the numerical methods in Chapter 4, now it is time to concentrate on the results of this research work. In this chapter, first, the results obtained from the macro-scale model, which mainly include the thermal and stress field evolution will be presented in Section 5.2. Second, the main abilities of the meso-scale model will be discussed in Section 5.3, and eventually, the attention will be drawn toward the formation of hot tearing with the aid of the multi-scale approach in Section 5.4.

5.2 Macro-scale Model

The thermomechanical model of DC casting was simulated for three different casting speeds shown in Table 5.1. In the following, the results of the macro-scale model for the simulation case A will be presented to provide an insight into the typical outcome

of the thermomechanical models.

Table 5.1: List of the macro-scale simulation cases

Case	**Casting speed (mm.min^{-1})**
A	66
B	56
C	46

In Fig. 5.2 the evolution of temperature with time for three points located at (a) the centerline, (b) the mid-radius, and (c) the surface of the billet and all at 40 mm above the bottom block as illustrated in Fig. 5.1 is presented. As can be seen, the evolution of temperature varies in radial direction and point (c) cools down much faster than points (a) and (b) owing to differential cooling conditions experienced by different locations. The surface of the billet is in direct contact with the mold and later with the cooling water impinging against it; therefore, the heat extraction is faster on the surface in comparison to the center and the mid-radius of the billet.

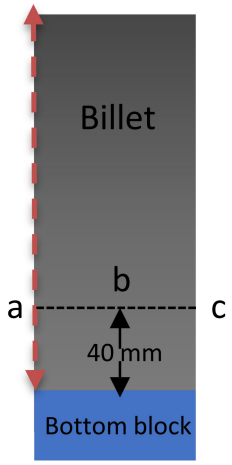

Figure 5.1: Location of points a, b, and c within the DC cast billet.

It should be noted that the temperature of the specified points does not decrease until about 35 seconds after the start of the casting when the layer of elements at the corresponding height is added.

The evolution of hoop stress as a function of time for points a, b, and c of Fig. 5.1 is displayed in Fig. 5.3. For all three locations, the hoop stress follows the same trend; it is close to zero before the coalescence temperature (T_{coal}), then it becomes compressive followed by a shift toward the tensile direction, and finally, it shows a uniform behavior until the simulation is completed. However, the evolution of hoop stress is much slower at the center of the billet (point a) than at its surface (point c), indicating that the variation in temperature field leads to a differential state of stress and deformation in the billet. In other words, the mechanical behavior of the billet is significantly dependent on the temperature distribution. Hence, it is essential to distinguish between the transient start-up phase of the casting and the steady state phase, because as explained in Chapter 1, the start-up region of the DC casting is the most crucial phase in terms of hot tearing formation. For achieving this purpose, the evolution of temperature as a function of time at different locations along the surface and the centerline of the billet is plotted in Fig. 5.4 and Fig. 5.5, respectively. It is worth mentioning that time zero for each temperature profile at a specific height represents the time at which the corresponding layer of elements is added. In both figures, as the height increases the temperature profiles get closer to each other and above a certain height, they start to merge. The height above which the temperature profiles do not change with the location anymore, is where the steady state phase is achieved. During the steady state phase of the DC casting, the heat transfer occurs from the surface of the billet to the mold and the cooling water; however, in the

start-up phase, the heat is also extracted from the bottom block, which causes the variation in the temperature profiles in this region. Another interesting observation is that although the surface of the billet reaches the steady state at around 50 mm above the bottom block, the centerline of the billet still experiences the start-up phase at this height and the temperature profiles do not converge until the height of 200 mm, which implies that the acceleration in the rate of heat extraction shifts the start of the steady state to lower heights in the billet. As hot tearing is a quality issue in the start-up region of the casting, it can be expected that there would be a higher risk of hot tearing formation near the center of the billet rather than its surface.

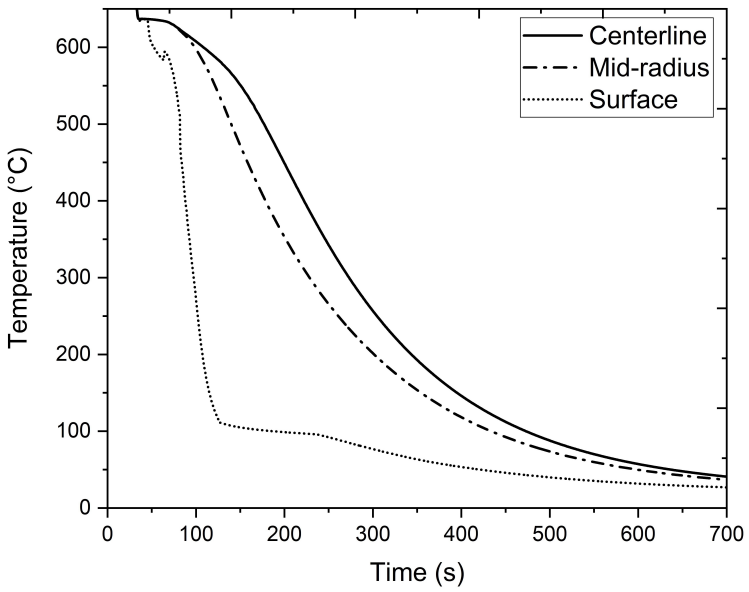

Figure 5.2: Evolution of temperature with time at three different locations in the billet shown in Fig. 5.1 for case A.

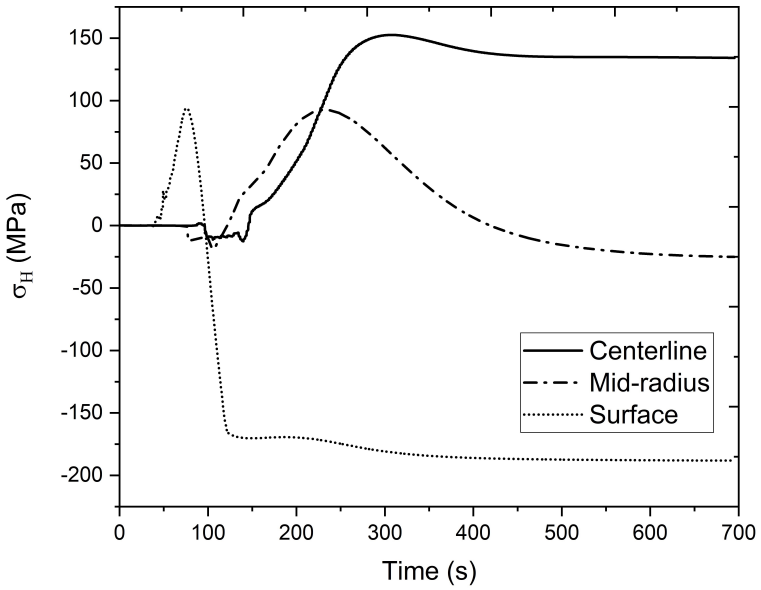

Figure 5.3: Evolution of hoop stress as a function of time at three different locations shown in 5.1 for case A.

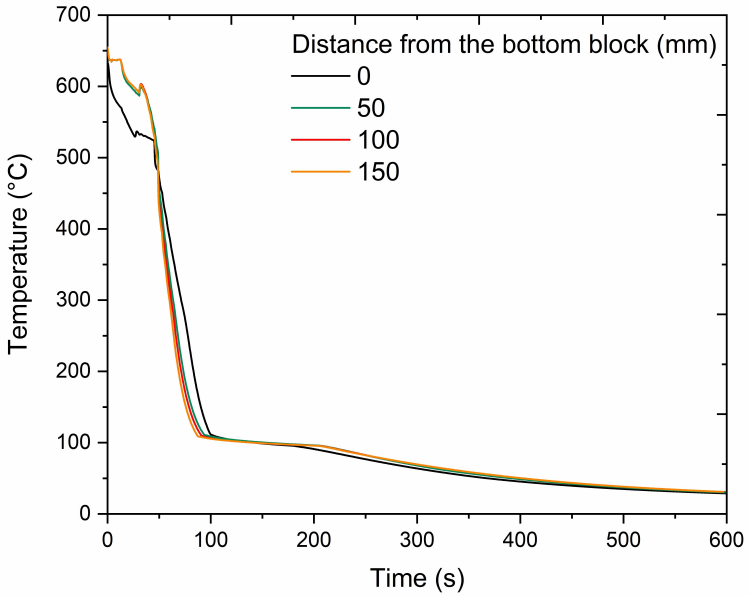

Figure 5.4: Evolution of temperature with time along the surface of the billet at different heights for case A.

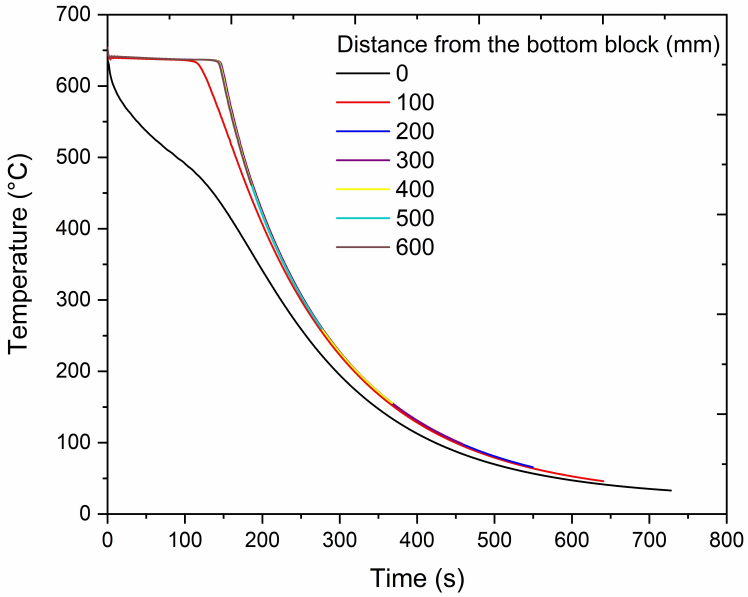

Figure 5.5: Evolution of temperature with time along the centerline of the billet at different heights for case A.

Fig. 5.6 illustrates the variation in the grain size and the contour plots of the hoop stress and the temperature field at the end of the casting throughout the billet. As shown in Fig. 5.6 (a), the grain size varies from 185 to 225 μm and the largest grains are found near the base of the casting, which confirms the fact that this region experienced the lowest cooling rate during solidification. From Fig. 5.6 (c), it can be observed that the area close to the surface of the billet experiences a compressive hoop stress distribution and the regions near the center of the billet are in tension. However, the hoop stress in the liquid sump, which is shown by red in Fig. 5.6 (b) is close to zero, because the temperature in that region ranges from 590 to 640°C, which is far from the coalescence temperature and the stress has not yet developed in the semi-solid material.

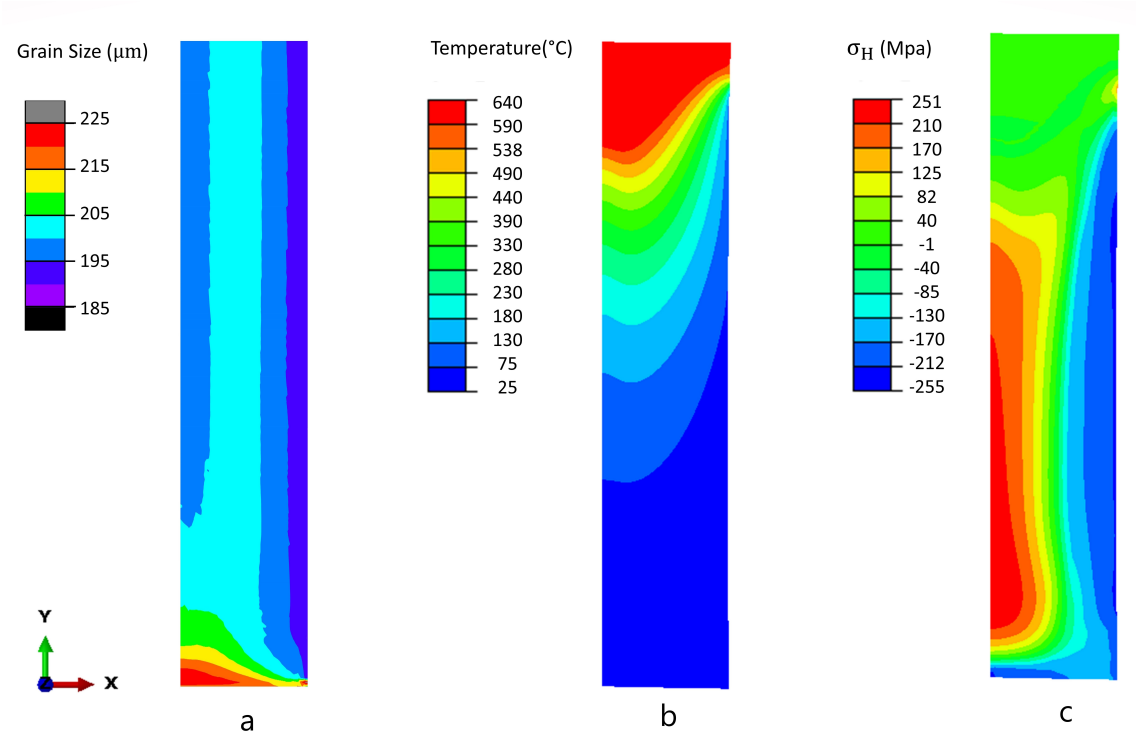

Figure 5.6: Contour plots representing (a) grain size, (b) temperature, and (c) the hoop stress at the end of the simulation for case A.

5.3 The Meso-scale Model

The macro-scale model can provide an insight into thermal and mechanical behavior of the DC cast billet during the casting and by implementing a hot tearing criterion, one can examine the susceptibility of different locations to hot tearing. However, hot tearing is a more complex incident influenced by the localization of straining and liquid feeding between the grains. Although such phenomenon cannot be explained in the macro-scale model, in which the smallest part of the simulation is one element (4 mm height $\times$ 5 mm width), they are well addressed in the meso-scale model. In the following, some of the most important capabilities of the meso-scale model, which will

assist us with the prediction of hot tearing in the scale of grains are demonstrated.

Fig. 5.7 shows the cross-section of a representative volume element with 7 grains per side at different solid fractions of 0.5, 0.7, and 0.9 generated by the solidification segment of the meso-scale model. Liquid channels and solid grains are colored in red and gray, respectively. It can be seen as the solid fraction increases, the thickness of liquid channels between the grains decreases and more grains come into contact together, coalesce and create grain clusters, i.e. groups of grains that are in solid contact with each other. Therefore, as the solid fraction increases, the fluid flow between the grains becomes more restricted.

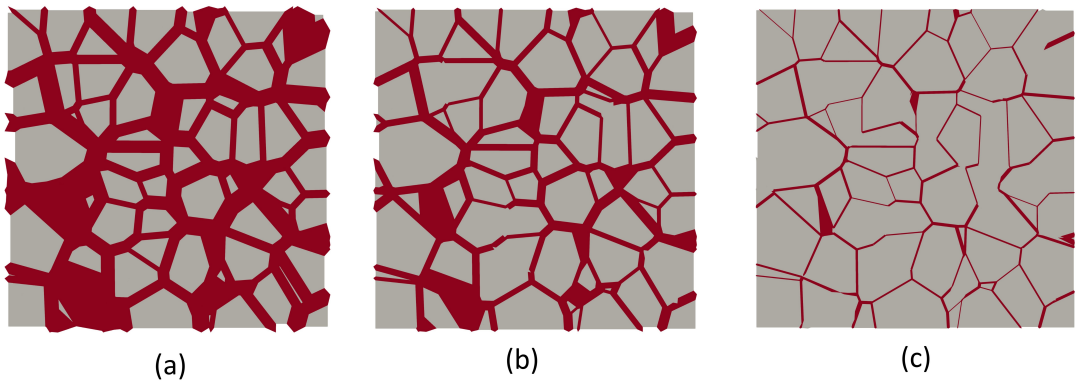

Figure 5.7: Cross-section of the representative volume element (RVE) generated by the solidification segment of the meso-scale model at three solid fractions of (a) 0.5, (b) 0.7, and (c) 0.9.

Fig. 5.8 shows the permeability of the mushy zone as a function of solid fraction for three different grain sizes of 100 μm, 200 μm, and 300 μm predicted by the fluid flow segment of the meso-scale model using Carman-Kozeny relation (Eq. 4.27). It can be observed that the permeability of the mushy zone decreases with increasing solid fraction, meaning that it is more difficult for fluid to pass through the liquid channels at high solid fractions rather than low solid fractions. Furthermore, the permeability

increases with the grain size owing to the decrease in the intrinsic specific solid-liquid interfacial area (S_v^{sl}) with increasing the grain size (recalling Eq. 4.27).

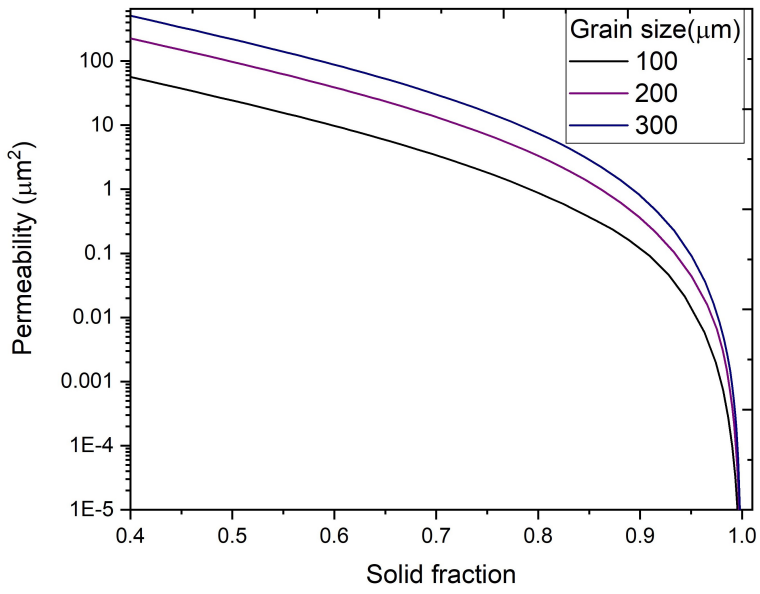

Figure 5.8: Variation of permeability of the mushy zone with solid fraction for three different grain sizes of 100 μm, 200 μm and 300 μm.

Fig. 5.9 shows the contours of liquid pressure at three different solid fractions of 0.5, 0.7, 0.9 for an RVE with 7 grains per side considering that a constant flux of $q = 50$ μm.s^{-1} is imposed on the bottom of the RVE ($x = 0$) and the liquid pressure is zero ($p_l = 0$) on the top surface, i.e. $x = L_x$. It should be noted that the values shown in the figures legend correspond to the pressure in the liquid channels and there is no pressure defined for solid grains; however, in order to better represent the variation of the pressure in the RVE, solid grains are also colored. It can be seen that for all three solid fractions, the pressure in liquid channels drops from zero on the surface $x = L_x$ to a negative value on the surface $x = 0$. Moreover, the liquid

pressure drop increases with the solid fraction such that at $g_s = 0.5$ (Fig. 5.9 (a)), the difference between the liquid pressure on the top and the bottom of the RVE is 5.2 Pa; however, it changes to 51 Pa and 4800 Pa for $g_s = 0.7$ and $g_s = 0.9$ (Fig. 5.9 (b) and (c)), respectively. Furthermore, the channels in which the liquid flow occur are shown with black and it is noticeable that as the solid fraction increases the number of such channels decreases; this means that with increasing the solid fraction, fluid flow in liquid occurs in more preferential paths.

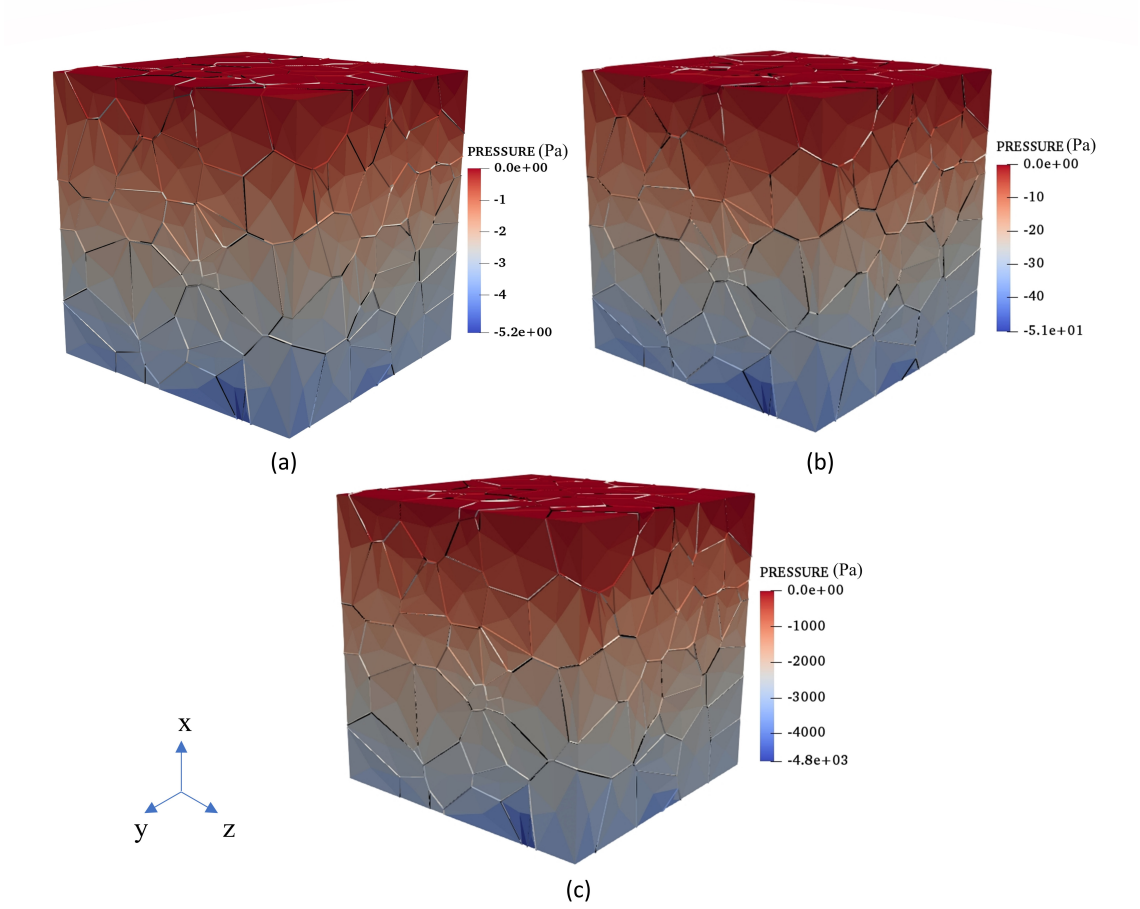

Figure 5.9: Contour plots of the liquid pressure drop for an RVE with 7 grains per side at solid fractions of (a) 0.5, (b) 0.7, and (c) 0.9.

Fig 5.10 shows the predicted average stress-strain behavior of an RVE over the surface $x = L_x$ with a grain size of 250 μm, subjected to a strain rate of 0.001 s^{-1} for three different solid fractions of 0.94, 0.96, and 0.98. All the surfaces of the RVE are considered to be closed to any fluid flow or in other words the fluid flux is zero on all surfaces ($q = 0$). It can be clearly seen that for all solid fractions the stress increases with strain until it reaches a maximum value. However, this increase is much larger for a solid fraction of 0.98 since as the solid fraction increases more grains coalesce, which increases the stiffness of the semi-solid.

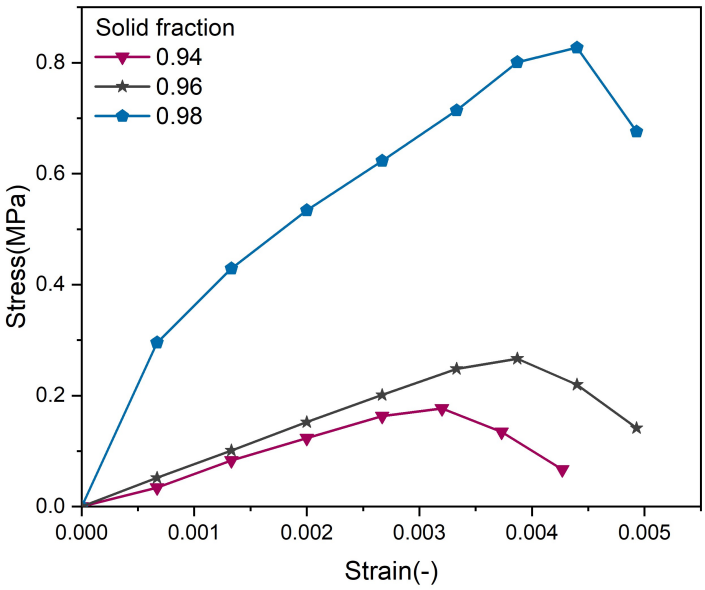

Figure 5.10: Average stress-strain behavior of the RVE subjected to a strain rate of 0.001 s^{-1} for different solid fractions of 0.94, 0.96, 0.98

5.4 Multi-scale Approach

Some of the important capabilities of the macro-scale and the meso-scale model have been reviewed and now it is time to focus on the multi-scale approach. The main challenge in this coupling is to determine when and how to apply the meso-scale model to optimize the computational costs. In this regard, first, the results of the pore fraction model for three simulation cases A, B, and C (Table 5.1) are presented in Section 5.4.1. Then, from those results, the locations in the billet exhibiting the highest susceptibility to hot tearing with respect to the pore fraction model are found and characteristics of such locations will be discussed in Section 5.4.2. After that, the focus will be placed on the tensile behavior of the RVEs possessing characteristics of the locations with the highest risk of hot tearing based on the pore fraction model (Section 5.4.3) and presenting a hot tearing susceptibility in Section 5.4.4. Finally the results obtained from the multi-scale approach are discussed against the available hot tearing models in the literature.

5.4.1 Pore Fraction Model

In order to explore the hot tearing susceptibility within the DC cast billet, the distributions of the total deformation pore fraction ($f_{p,de} = f_{p,de,\varepsilon x} + f_{p,de,\varepsilon y}$) for simulation cases A, B, and C are analyzed. Fig. 5.11 shows the variation of the total deformation pore fraction as a function of distance from the bottom block along the centerline of the billet at solid fraction of 0.98 for the three simulation cases A, B, and C. As can be seen, for all three cases the pore fraction is an increasing function of the distance from the bottom block until it reaches a peak value at a few millimeters above the bottom surface of the billet, which indicates the susceptibility of the billet to hot

tearing in the start-up region. As the casting speed increases, the peak value of the deformation pore fraction also increases and shifts to lower heights in the billet such that it occurs at the height of 12 mm, 16 mm, and 24 mm above the bottom block for casting speeds of 66 mm.min^{-1} (case A), 56 mm.min^{-1} (case B), and 46 mm.min^{-1} (case C), respectively. After the peak value has been attained, the pore fraction is followed by a decreasing trend until 50-100 mm above the bottom block depending on the casting speed. For case C, the pore fraction becomes zero above 90 mm from the bottom block, meaning that there is no vulnerability to hot tearing; however, for case A and B, the pore fraction starts to increase after 80 and 100 mm above the bottom block, respectively in such a way that for case A at the height of 350 mm, it even becomes larger than the peak value. Therefore, it can be surmised that for case A the hot tearing susceptibility starts to increases above 80 mm from the bottom block, but as discussed before and shown in Fig. 5.5, above 200 mm from the bottom block, the DC cast billet reaches the steady state region, where the chance of hot tearing formation is extremely low.

Recalling Eq. 4.21 and Eq. 4.22 shows that $f_{p,de,\varepsilon x}$ and $f_{p,de,\varepsilon y}$ are functions of $\dot{\varepsilon}_{px}$ and $\dot{\varepsilon}_{py}$, respectively. Fig. 5.12 shows the variation in the strain rate parallel with the thermal gradient ($\dot{\varepsilon}_{px}$) and Fig. 5.13 depicts the evolution of the strain rate perpendicular to the thermal gradient ($\dot{\varepsilon}_{py}$) along the centerline of the billet in terms of the distance from the bottom block. By comparing the two figures, it can be noticed that the evolution of the deformation pore fraction in the start-up and the steady state phase is controlled by $\dot{\varepsilon}_{px}$ and $\dot{\varepsilon}_{py}$, respectively. Therefore, the increase in the deformation pore fraction for case A in the steady state region is the result of the increase in $\dot{\varepsilon}_{py}$ as shown in Fig. 5.13, which implies hot tearing susceptibility in the

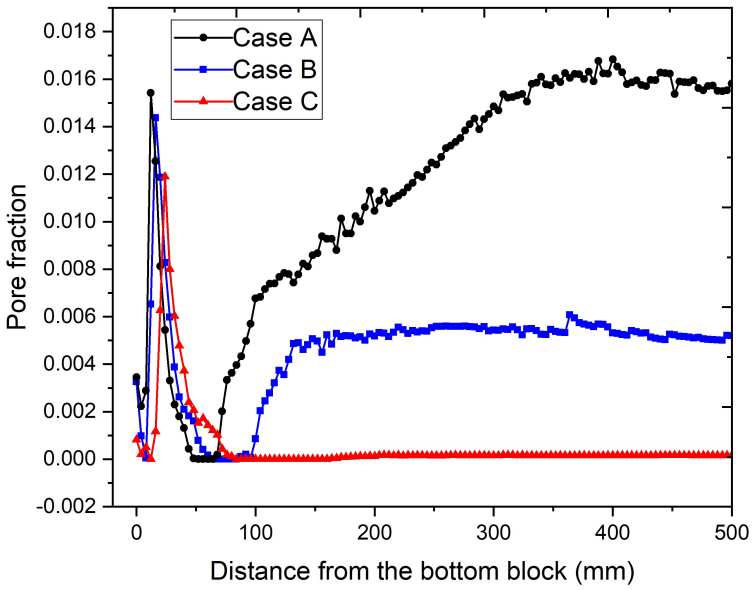

Figure 5.11: Evolution of the deformation pore fraction along the centerline of the billet at solid fraction of 0.98 for the macro-scale simulation cases A, B, and C.

steady state region. However, after plotting the strain perpendicular to the thermal gradient along the centerline of the billet, which is calculated in the same way as $\dot{\varepsilon}_{py}$ (Eqs. 4.23 to 4.24) but by using the strain tensor in the global coordinate instead of the strain rate tensor, it is shown in Fig. 5.14 that the strain perpendicular to the thermal gradient becomes negative above 32 mm from the bottom block, meaning that the strain is compressive which not only does not cause cracking, but it can also heal the hot tears by leading the liquid into regions where feeding is difficult. Therefore, the positive increasing values of $\dot{\varepsilon}_{py}$ seen in Fig. 5.13 results from the increase in the compressive strain with time. Hence, it can be deduced that the positive values of $\dot{\varepsilon}_{py}$ and $\dot{\varepsilon}_{px}$ causes hot tearing susceptibility if the semi-solid material is in tension.

In order to study the hot tearing propensity in radial direction, the evolution of deformation pore fraction as a function of distance from the centerline of the billet

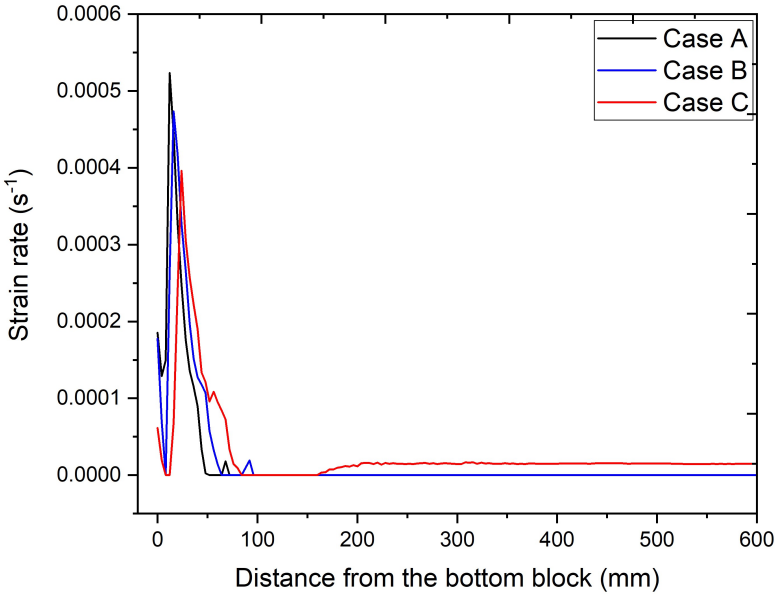

Figure 5.12: Evolution of the strain rate parallel with the thermal gradient ($\dot{\varepsilon}_{px}$) along the centerline of the billet at solid fraction of 0.98 for the macro-scale simulation cases A, B, and C.

for cases A, B, and C at three different heights of 12 mm, 16 mm, and 24 mm above the bottom block is plotted in Fig. 5.15. For each case, the height is chosen based on the location of the peak value in Fig. 5.11. It can be observed that the deformation pore fraction generally decreases as it gets closer to the surface of the billet, implying that the hot tearing susceptibility decreases in radial direction. Therefore, from the results of applying the pore fraction hot tearing criterion to the macro-scale model, it can be concluded that there is a risk of hot tearing formation near the center of the billet and as the casting speed increases, the distance between the point with the highest vulnerability to hot tearing and the bottom surface of the billet decreases. Moreover, there is no risk of hot tearing formation near the surface of the billet.

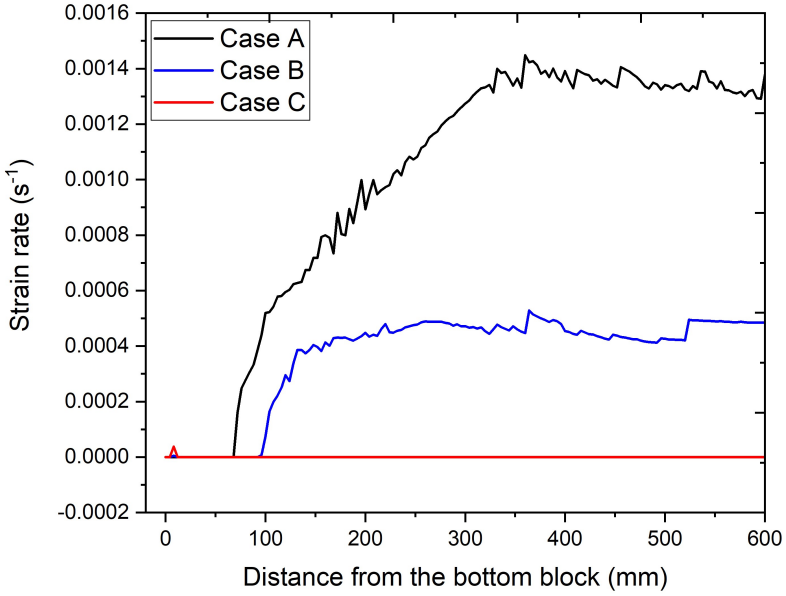

Figure 5.13: Evolution of the strain rate perpendicular to the thermal gradient ($\dot{\varepsilon}_{py}$) along the centerline of the billet at solid fraction of 0.98 for the macro-scale simulation cases A, B, and C.

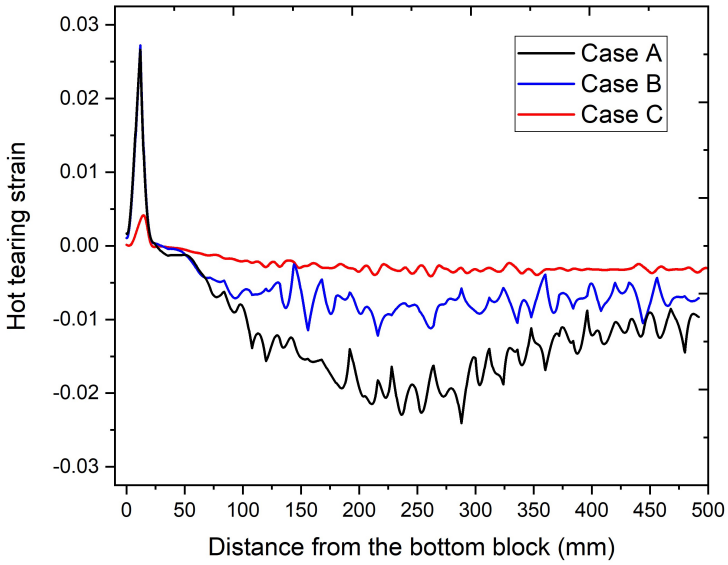

Figure 5.14: Variation in the strain perpendicular to the thermal gradient as a function of distance from the bottom block along the centerline of the billet at solid fraction of 0.98 for the macro-scale simulation cases A, B, and C.

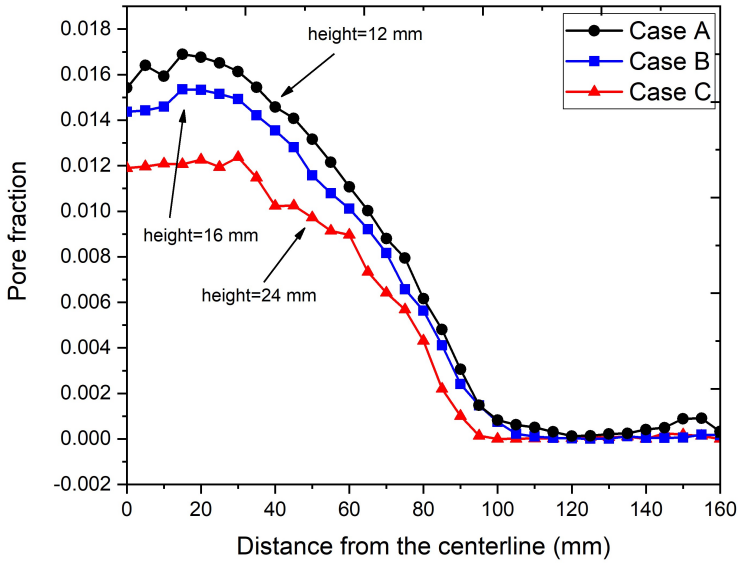

Figure 5.15: Evolution of the deformation pore fraction as a function of distance from the centerline of the billet at solid fraction of 0.98 for the macro-scale simulation cases A, B, and C.

5.4.2 Characteristics of Susceptible Locations

Although the risk of hot tearing initiation has been investigated so far, the question whether or not hot tears will initiate still remains. To answer this question, it is required to identify the location within the billet demonstrating the highest risk of hot tearing formation according to the pore fraction model for each simulation case. Such locations are named X, Y, and Z for simulation cases A, B, and C, respectively and their coordinates are listed in Table 5.2. The next step is to extract the grain size, strain rate, and thermal gradient from the macro-scale model as well as calculate the feeding coefficient of locations X, Y, and Z at solid fraction of 0.98. Then the RVE, which contains a certain number of grains is deformed with a constant bulk strain rate as explained in Chapter 4. In order for the reader to gain an understanding of

the variation of the mentioned parameters in radial direction, they are plotted at the height of 12 mm, 16 mm and 24 mm above the bottom block for simulation cases A, B, and C, respectively, as a function of distance from the centerline of the billet in the following.

Fig. 5.16 shows the variation in the grain size for simulation cases A, B, and C in radial direction at the specified heights. As can be seen, for all three cases the grain size is generally a decreasing function of the distance from the centerline of the billet; although the casting speed is different, the grain size is almost the same in the locations with the highest risk of hot tearing formation.

The bulk strain and strain rate are defined as the volumetric deformation and the rate of such deformation. However, the strain rate parallel to the thermal gradient that causes cracking in the start-up region as explained by the pore fraction model, is an axial strain rate. Therefore, it is considered that the bulk strain rate is $3 \times \dot{\varepsilon}_{px}$; with such consideration, the variation of the bulk strain rate in radial direction for the three simulation cases A, B, and C is shown as Fig. 5.17. It can be seen that the bulk strain rate increases with the casting speed and decreases in radial direction.

Table 5.2: Locations within the billet for which the semi-solid geometries are generated, x is the distance from the centerline and y is the distance from the bottom block.

Macro-scale simulation case	**Location within the billet**	**x (mm)**	**y (mm)**
A (66 mm.min^{-1})	X	15	12
B (56 mm.min^{-1})	Y	15	16
C (46 mm.min^{-1})	Z	20	24

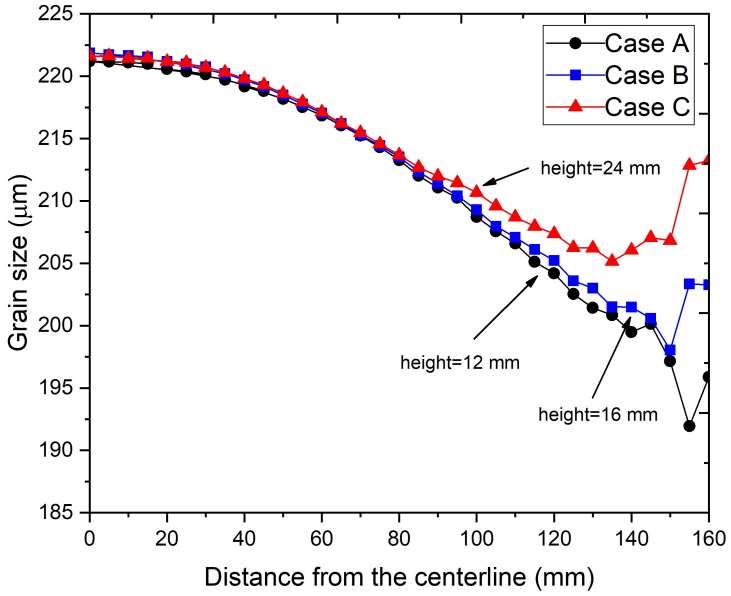

Figure 5.16: Evolution of grain size in radial direction at solid fraction of 0.98 for the macro-scale simulation cases A, B, and C at the heights specified in Table 5.2.

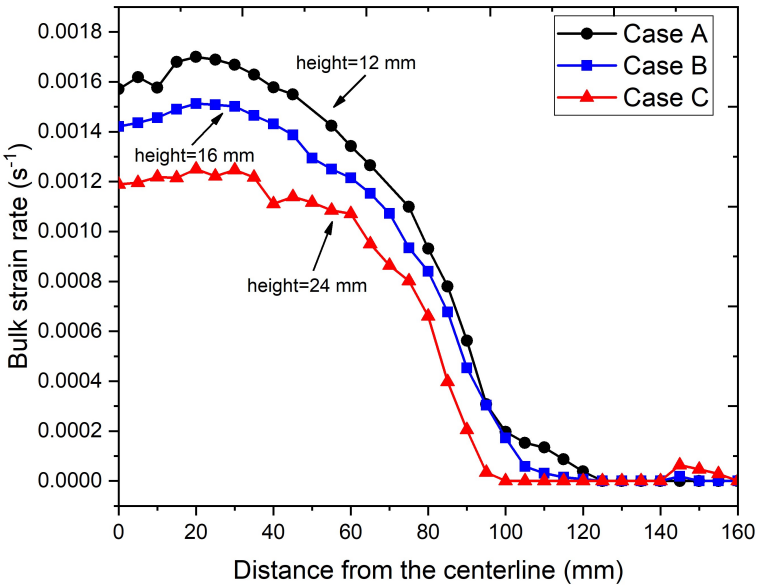

Figure 5.17: Evolution of bulk strain rate in radial direction at solid fraction of 0.98 for the macro-scale simulation cases A, B, and C at the heights specified in Table 5.2.

As explained in Chapter 4, in order to take into account the feedability of the mushy zone, it is required to calculate the feeding coefficient at the solid fraction of interest, i.e. g_s=0.98. Recalling Eq. 4.26, the feeding coefficient (f_l) is a function of permeability (K), solid fraction (g_s), thermal gradient (G), and viscosity of the fluid (μ_l). Considering a constant viscosity of 0.0015 Pa.s and a grain size of 220 μm, the variation in the feeding coefficient as a function of solid fraction for thermal gradients of 2500, 3500, and 5500 K.m^{-1} is shown in Fig. 5.18. It can be clearly observed that as the solid fraction increases and the thermal gradient decreases, the feedability of the mushy zone decreases. Fig. 5.19 shows the variation of the thermal gradient in radial direction at the specified heights for three simulation cases. It is clear that the thermal gradient increases with the distance from the centerline at a given height. The feeding coefficient, thermal gradient, grain size, and bulk strain rate at the determined locations X, Y, and Z are listed in Table 5.3. The next step is to generate the semi-solid geometry corresponding to those locations.

Table 5.3: Characteristics of nodes demonstrating the highest deformation pore fraction at solid fraction of 0.98

Simulation case	**X**	**Y**	**Z**
d (μm)	220	220	220
$\dot{\varepsilon}_v$ (s^{-1})	0.0017	0.0015	0.0012
G (K.m^{-1})	3000	2850	2700
f_l (μm.Pa^{-1}.s^{-1})	0.008	0.007	0.006

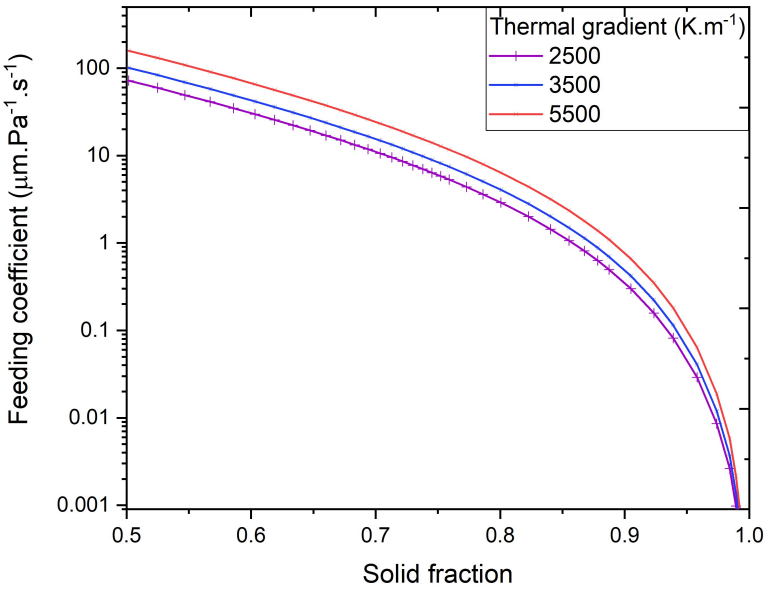

Figure 5.18: Variation in feeding coefficient with solid fraction for thermal gradients of 2500 K.m^{-1}, 3500 K.m^{-1}, 5500 K.m^{-1} and a constant grain size of 220 μm.

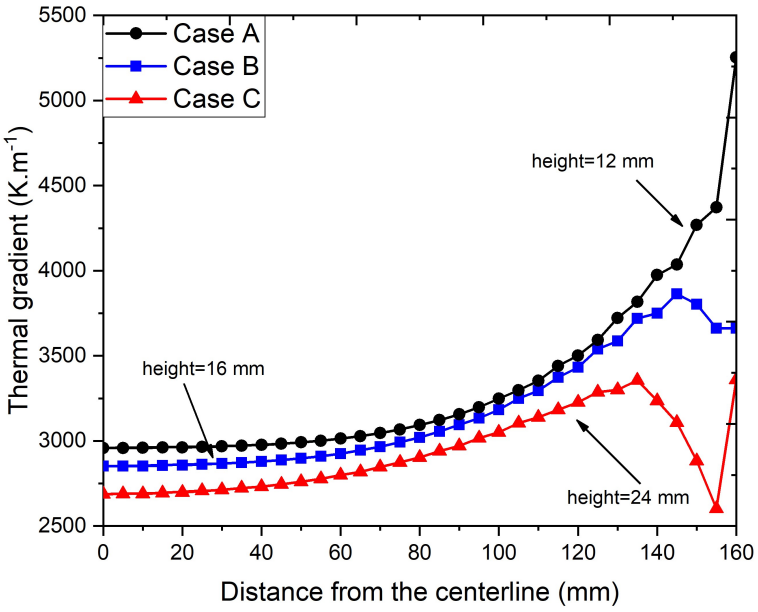

Figure 5.19: Evolution of thermal gradient in radial direction at solid fraction of 0.98 for the macro-scale simulation cases A, B, and C at the heights specified in Table 5.2.

5.4.3 Application to Meso-scale Model

Fig. 5.20 (a) and (b) represent the average stress and the average liquid pressure of the RVE as a function of strain over the surface $x = L_x$ at solid fraction of 0.98 for simulation cases X, Y, and Z. As can be seen in Fig. 5.20 (a), the stress increases with the strain for all three cases until it reaches a maximum value, which can be called the failure stress, then no further increase is observed in the stress evolution. Moreover, the strain at which the failure is achieved varies in such a way that for case X it is almost twice as large as that for case Z. However, the failure stress does not considerably vary for the three simulation cases.

As illustrated in Fig. 5.20 (b), by applying tensile deformation to the RVE, the liquid pressure drops from its initial value which is considered to be zero. For each case, the strain at which the maximum liquid pressure drop and maximum stress are achieved represents the onset of cracking. For simulation case Z, the crack initiation happens at a smaller strain but larger liquid pressure drop in comparison to cases X and Y. This can be explained in terms of the smaller feeding coefficient (f_l) used for case Z, which causes more restricted liquid feeding between the grains and consequently a larger pressure drop as the deformation proceeds. However, since the strain rate for each simulation case is different, it is not possible to give a clear statement about the effect of liquid feeding and also strain rate on the tensile behavior of the RVE.

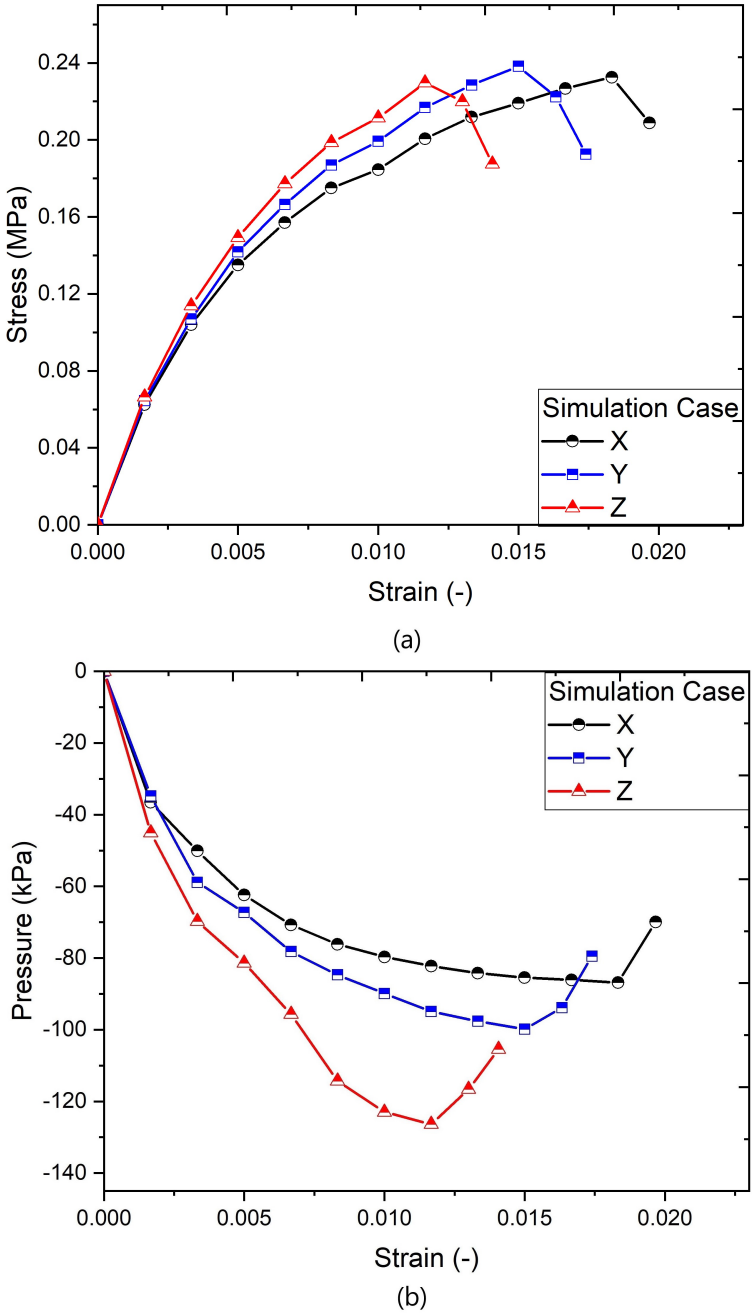

Figure 5.20: Simulated (a) stress-strain curves and (b) pressure-strain curves of the RVE with liquid feeding for simulation cases X, Y, and Z.

To more clearly demonstrate the tensile behavior of the RVE, the stress-strain and the pressure-strain curves corresponding to case Y are plotted together in Fig. 5.21. In addition, the contour maps of the maximum principal strain at three strain values of $\varepsilon_1 = 0.0133$, $\varepsilon_2 = 0.0163$ and $\varepsilon_3 = 0.0174$, which are defined with red squares in Fig. 5.21, are shown in Fig. 5.22 (1) , (2), and (3), respectively. In contour map (1), which is one increment before the maximum stress is achieved, the strain is localized between the grains, but there is no sign of a crack. The crack initiation and growth are shown in contours 2 and 3 which correspond to one and two increments after the maximum stress is obtained, respectively.

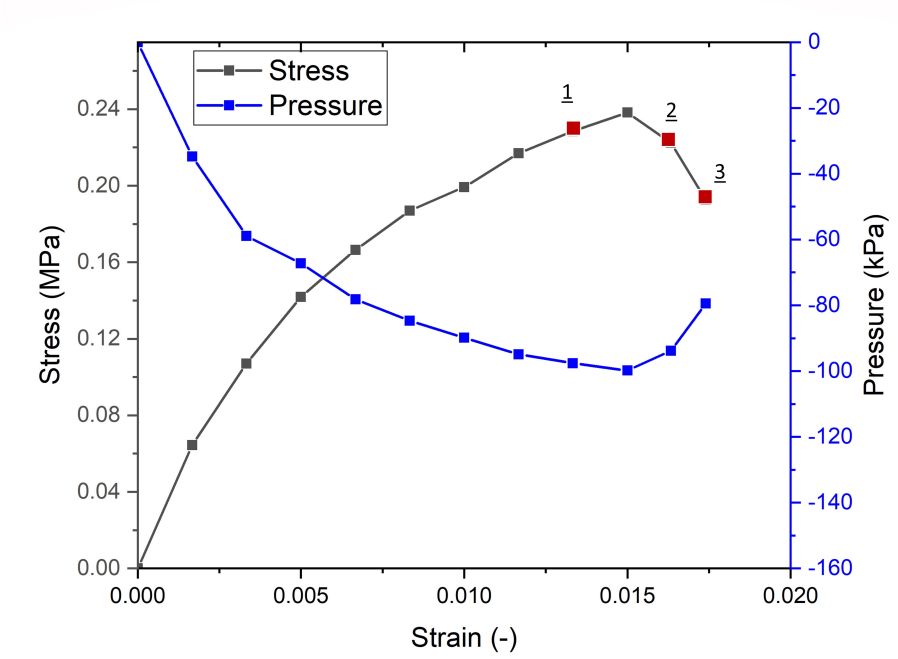

Figure 5.21: Simulated stress-strain and stress-pressure curves for simulation case Y.

The increase in the liquid pressure after the maximum pressure drop is reached is due to the fact that the crack growth causes the associated liquid channel to become dry and its remaining liquid is sucked into other regions of the RVE. The corresponding

liquid channel will be eliminated from the fluid flow and deformation calculations of the next increment.

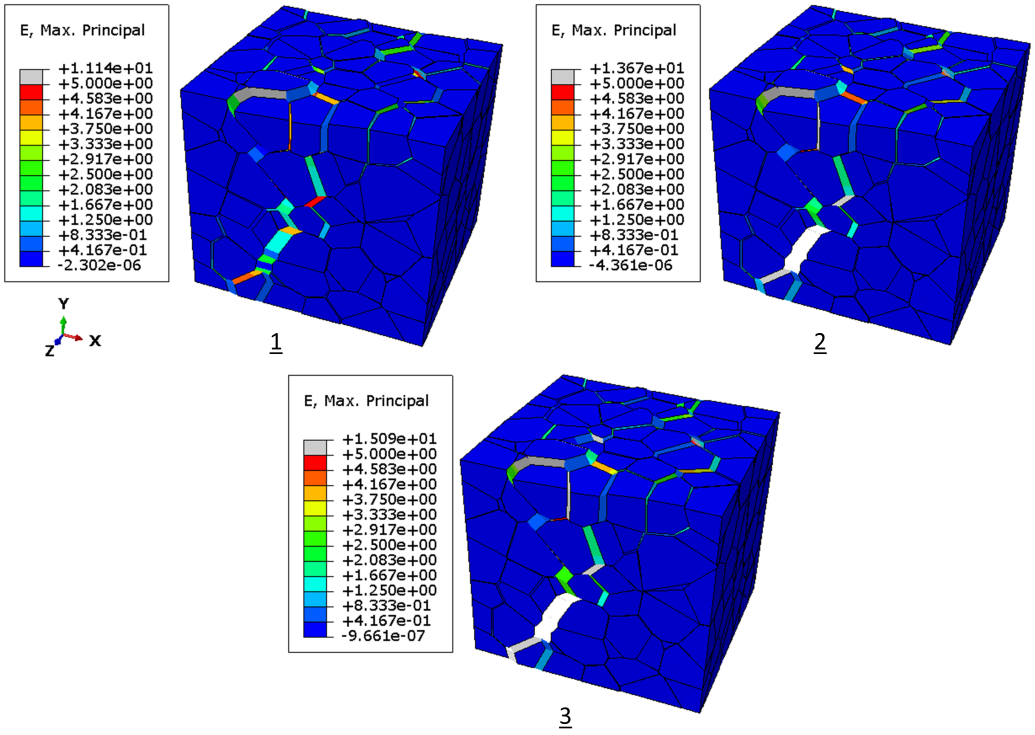

Figure 5.22: Contour maps of maximum principal strain for three strain values defined in Fig. 5.21 corresponding to case Y.

To investigate the effect of bulk strain rate ($\dot{\varepsilon}_v$) and the feeding coefficient (f_l) on the tensile behavior of the mushy zone, five simulations with a constant grain size of 220 μm and various $\dot{\varepsilon}_v$ and f_l where performed. The corresponding stress-strain behaviors are plotted in Fig. 5.23. As can be seen, the decrease in f_l and increase in $\dot{\varepsilon}_v$ result in a higher resistance to tensile deformation or in other words higher stiffness. However, determining which parameter controls the tensile behavior of the RVE depends on their values. A comparison between the green curve (f_l = 0.01 μm.Pa^{-1}.s^{-1} , $\dot{\varepsilon}_v$ = 0.0017 s^{-1}) and the blue curve (f_l = 0.007 μm.Pa^{-1}.s^{-1} ,

$\dot{\varepsilon}_v = 0.0012$ s^{-1}) indicates that $\dot{\varepsilon}_v$ is the controlling parameter, while comparing the green curve with the red curve ($f_l = 0.007$ μm.Pa^{-1}.s^{-1} , $\dot{\varepsilon}_v = 0.0015$ s^{-1}) shows the opposite. With this information, in Fig. 5.20 (a), f_l is the controlling parameter, meaning that although $\dot{\varepsilon}_v$ increases with casting speed, the increase in f_l results in lower stiffness for simulation case X with casting speed of 66 mm.min^{-1}.

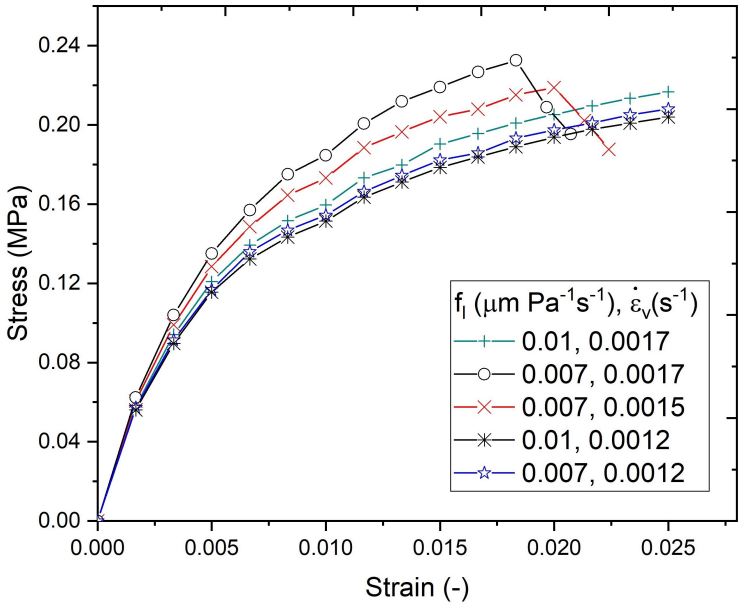

Figure 5.23: Simulated stress-strain behavior of the RVE for various feeding coefficients and bulk strain rates.

The tensile behavior of the mushy zone at the location in the billet demonstrating the highest hot tearing susceptibility according to the pore fraction model for each of the three simulation cases was investigated. The findings infer that for the most vulnerable locations the results from the pore fraction model are in accordance with the multi-scale approach, meaning that crack initiation will occur at locations with the highest deformation pore fraction. Although a constant grain size of 220 μm was

chosen for the three simulation cases X, Y, and Z, it generally varies with location in the billet as shown in Fig. 5.6 (a). To study the role of grain size, a number of simulations were performed considering a constant $f_l = 0.007$ μm.Pa^{-1}.s^{-1} and various $\dot{\varepsilon}_v$ and d. For each simulation, the stress at fracture was recorded and the resulting contour map is depicted in Fig. 5.24. It is worth mentioning that large values for $\dot{\varepsilon}_v$ were used deliberately to force the crack formation in the RVE. It is clear that the stress at fracture decreases with grain size. However, for a constant grain size, the variation in $\dot{\varepsilon}_v$ does not significantly affect the stress at fracture and such observation is also confirmed by Fig. 5.20 (a). Hence, it can be deduced that regardless of the applied bulks strain rate, as the grain size decreases, the crack initiation requires a larger stress which implies lower propensity to hot tearing formation.

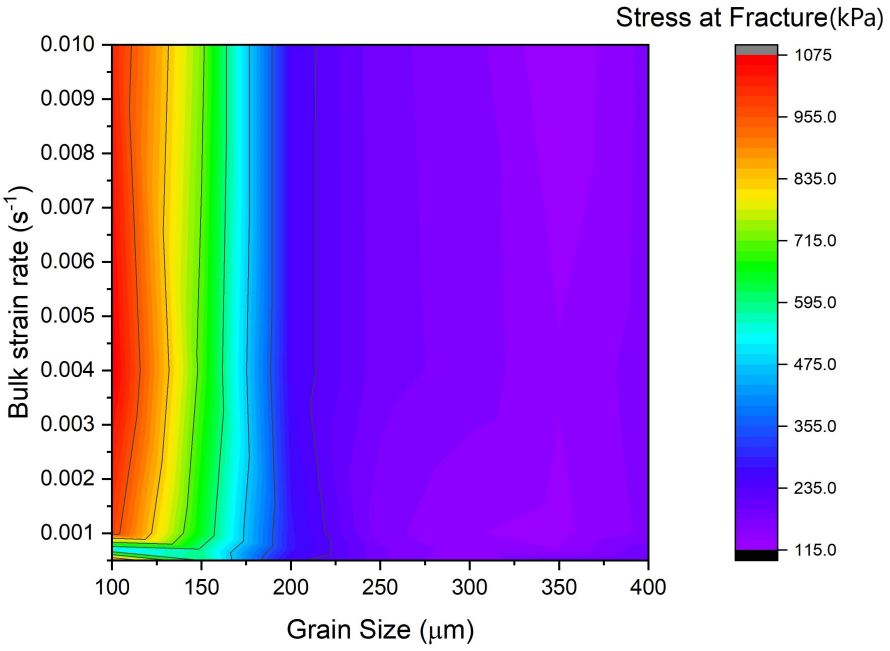

Figure 5.24: Contour map of stress at fracture as a function of bulk strain rate and grain size for a constant feeding coefficient of 0.007 μm.Pa^{-1}.s^{-1}.

5.4.4 Hot Tearing Susceptibility Map

As explained so far, the multi-scale approach can provide detailed information about the mechanical behavior of the mushy zone at different locations and consequently predict the crack initiation and growth considering the liquid pressure drop between the grains as a result of deformation. Furthermore, this approach can be used to generate a map that defines the locations within the billet where hot tearing formation most likely occurs, which would be beneficial for the aluminum DC casting industry. Fig. 5.25 shows the hot tearing susceptibility maps generated for the macro-scale simulation cases A, B, and C. In this figure, the red dots are representative of locations in which hot tears will possibly form and the rest of the billet colored in gray corresponds to region where hot tears are not expected to form. For the sake of visibility, only 190 mm of each billet is shown.

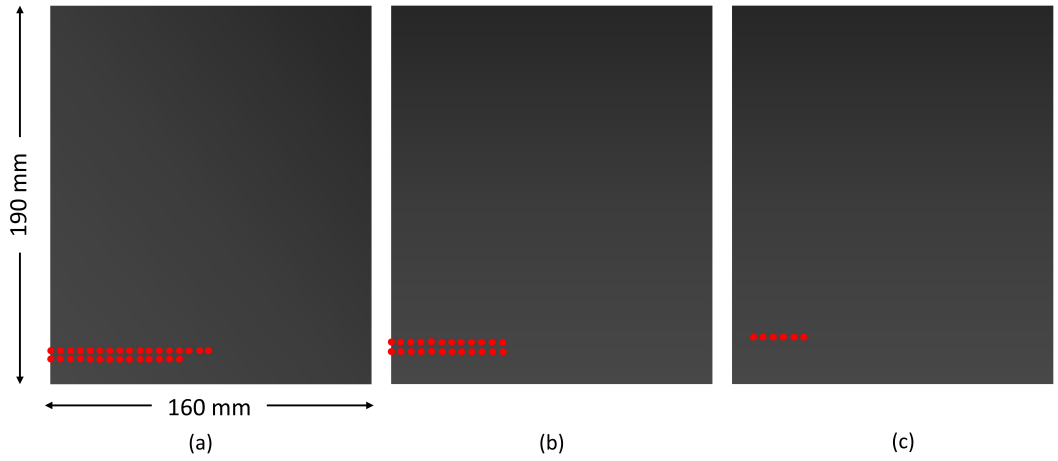

Figure 5.25: Hot tearing susceptibility map for simulation cases a) A with casting speed of 66 mm.min^{-1}, b) B with casting speed of 56 mm.min^{-1}, and c) C with casting speed of 46 mm.min^{-1}.

It is worth mentioning that since the nodal values of temperature, cooling rate, thermal gradient and strain rate were extracted from ABAQUS, hot tearing formation is examined at the vertices of the rectangular elements (4 mm height $\times$ 5 mm width). As can be seen, the number of red points increases with the casting speed. Therefore, it can be concluded that the hot tearing propensity of a billet increases with the casting speed or in other words as the casting speed increases there are more possible locations within the billet where hot tears can form.

5.5 Summary

A multi-scale approach for simulating hot tearing phenomenon in DC casting of aluminum alloys was presented. The novelty of this approach lies in the combination of the macro-scale simulation of the DC casting process with the multi-physics granular modeling of hot tearing defect. As discussed in the previous sections, the multi-scale approach is capable of simulating hot tearing initiation, growth, and propagation within a representative volume element of the mushy zone. However, most of the available models in the literature have focused on the hot tearing susceptibility, which does not give any indication whether or not hot tears will form. According to the multi-scale approach, hot tearing formation is a function of several influencing and interdependent parameters. The change of cooling condition experienced by the DC cast billet as a result of the variation of casting speed as well as non-uniformity of heat extraction from different locations of the billet affects the deformation state, cooling rate, and thermal gradient, which further influence the strain rate, grain size, permeability, and feeding coefficient. Considering all the mentioned parameters, the multi-scale approach emphasizes the fact that hot tearing is a phenomenon resulting

from the combination of the tensile deformation and restricted feeding of the mushy zone. Recent well-known hot tearing models such as the RDG criterion, the dimensionless Niyama criterion, and the pore fraction model also account for the effect of deformation and liquid pressure drop to predict hot tearing susceptibilities. However, they are not able to answer the question if hot tears would initiate in intergranular regions at locations with lower risk of hot tearing formation or not. For instance, the pore fraction model (Section 5.4.1) reported that along the centerline of the billet, the locations at 12 mm, 16 mm, and 24 mm above the bottom block for simulation cases A, B, and C are at the highest risk of hot tearing formation. However, the model cannot predict if hot tearing occurs for other locations with lower risk of hot tearing formation. In the multi-scale approach, the pore fraction model is used as an aid to determine where to start the meso-scale simulations to reduce high computational costs. From the hot tearing susceptibility map presented in Section 5.4.4, it can be inferred that hot tearing prediction of the multi-scale approach is in correlation with the results of experimental and numerical investigations available in the literature such as the study by M'Hamdi et al. [23] or Jamaly et al. [1], which agree upon the increase in hot tearing susceptibility as a result of the increase in the casting speed.

Chapter 6

Conclusion and Perspectives

Hot tearing is a complex defect associated with DC casting of aluminum alloys. Various mathematical simulations have been performed in the literature to model the DC casting process and predict hot tearing formation. Due to the large dimensions of the DC cast billets, the proposed DC casting models in the literature simulate the process in the macro-scale, then a hot tearing criterion is implemented through post processing calculations to predict the risk of hot tearing formation. However, since hot tearing is an intergranular phenomenon, the available models in the literature could not address the problem of hot tearing properly. In this thesis, a multi-scale approach for investigating the tensile behavior of different locations of the DC cast billet at the scale of grains and consequently predict hot tearing formation was developed. This approach takes into account both the macroscopic aspects of the DC casting process and the microscopic nature of the hot tearing formation and consists of two separate models:

1. The macro-scale model: a thermomechanical model of the DC casting process

implemented in ABAQUS finite element package at the macro-scale to predict the evolution of temperature, cooling rate, thermal gradient, strain, and strain rate.

2. The meso-scale model: a coupled meso-scale hydro-mechanical granular model known as GMS-3D, which consists of 4 separate segments; (1) the solidification segment, (2) the fluid flow segment, (3) the semi-solid deformation segment, and (4) the failure segment.

The macro-scale model predicts the evolution of temperature, strain rate, cooling rate, thermal gradient, and grain size with time at different locations within the DC cast billet for three different simulation cases with casting speeds of 46 $mm.min^{-1}$, 56 $mm.min^{-1}$, and 66 $mm.min^{-1}$. Then, the output of the macro-scale model was used as input to the meso-scale model to investigate the effect of different parameters at both macro and mesoscopic scales on tensile behavior of a representative volume element (RVE) of the mushy-zone, which lead to the following conclusions:

1. The combination of different parameters determines the tensile behavior of the RVE. For a constant grain size, as the feeding coefficient decreases and the strain rate increases, the liquid pressure drop and the resistance to tensile deformation increases and crack formation occurs at lower strains. For a constant feeding coefficient, regardless of the applied bulk strain rate, the stress at fracture increases with decreasing the grain size, meaning that as the grain size decreases, the mushy zone becomes more resistance to hot tearing formation.

2. The tensile behavior of different locations of the DC casting billet was demonstrated in terms of contour maps of the RVE corresponding to different strain

values of the stress-strain curve. Such contour maps show the strain localization between the grains as well as hot tearing initiation, growth, and propagation within an RVE.

3. Hot tearing susceptibility map was generated to determine the region within the DC cast billet were hot tearing formation can occur. According to this map, in the three DC casting simulations performed, the condition for hot tearing formation was favorable at a few millimeters above the bottom block and near the centerline of the billet. As the casting speed increases, this region shifts to lower heights in the billet and a greater region is prone to hot tearing.

Regarding the limitations of the implemented simulation techniques and the results obtained from this study, the following potential future research directions are suggested:

1. Modifying both the macro-scale and the meso-scale models will improve the accuracy of the multi-scale approach. In this regard, including a macrosegregation model in order to take into account the variation of alloy properties with composition and considering the effect of cooling rate and chemical composition on the solidification path in the macro-scale model would be advantageous. In terms of the meso-scale model, although the corners of the polyhedral grains have been rounded for grains coalescence, in the fluid flow and deformation calculations they are still edgy; therefore, using smooth grains would enhance the performance of the meso-scale model.

2. The results of the macro-scale and the meso-scale models have been validated

against experimental data for aluminum alloy AA5182 and Al-2wt.%Cu, respectively. Therefore, it is suggested to perform X-ray tomography during the tensile deformation of semi-solid aluminum alloy AA5182 to validate the meso-scale model for this alloy.

3. Some of the results of the multi-scale approach needs to be validated against experimental data. For instance, the simultaneous effect of the feeding coefficient and bulk strain rate in determining the tensile behavior of the RVE or the result showing that the stress at fracture in the mushy zone at a high solid fraction with a constant feeding coefficient is only a function of grain size and independent of the applied bulk strain rate, require further investigations.

Appendix

A. *The Thermomechanical model of DC Casting Process (The Macro-scale Model)*

The DC casting process of the AA5182 alloy was simulated using an axi-symmetric fully coupled thermomechanical model realized with the general purpose software ABAQUS version 2017. The solidification and constitutive models are implemented in ABAQUS through the user programmable subroutine UHARD. The model was previously developed by Drezet et al. [75] and Jamaly et al. [1] to which the readers are referred for further details and references. Although the corresponding ABAQUS input file and the user subroutine code are not provided in this thesis, they are available in the repository kept by Dr. André Phillion in the department of Materials Science and Engineering at McMaster University.

B. *The 3-D Coupled Hydro-mechanical Model (The Meso-scale Model)*

The 3-D coupled hydro-mechanical model used in this thesis is custom software developed in C++ programming language by Dr. André Phillion and his former colleague Dr. Meisam Sistaninia in Computational Materials Laboratory at EPFL University. The model consists of four separate segments; (I) the solidification segment, (II) the fluid flow segment, (III) the semi-solid deformation segment, and (IV) the failure

segment. The input geometry for solidification segment was created using the open source library Voro++. For the fluid flow calculations, a finite element code which uses a C++ template library known as IML++, has been written. In order to perform the numerical simulation of the semi-solid deformation segment, the output of the solidification calculation is translated to a finite element mesh with the aid of a C++ subroutine, which also generate the ABAQUS control file. The semi-solid deformation simulations is then performed using the commercial finite element package ABAQUS version 2019. Finally, by considering a failure criterion, the fluid flow segment, the semi-solid deformation segment, and the failure segment are coupled through pressure in the liquid and opening at grain boundaries. By using a control file that specifies the parameters setting, simulation of the uncoupled fluid flow model, the uncoupled mechanical model, and the coupled hydro-mechanical model can be performed. For further information about each model, the readers are referred to Refs.[70], [76], and [74], respectively. Although the simulation code is not provided in this thesis, it is in the repository kept by Dr. André Phillion in the department of Materials Science and Engineering at McMaster University.

C. *Development of The Pore Fraction Model*

Although a full description of the pore fraction model has been given in Ref. [89], the key equations governing the model are summarized here for the sake of completeness. The mass conservation equation and Darcy's law in a control volume which consists of dendrite arms and interdendritic liquid are expressed as Eq. C.1 and Eq. C.2, respectively:

$$\mathrm{div}\langle \rho V \rangle - v_T \frac{\partial \langle \rho \rangle}{\partial x} = 0, \tag{C.1}$$

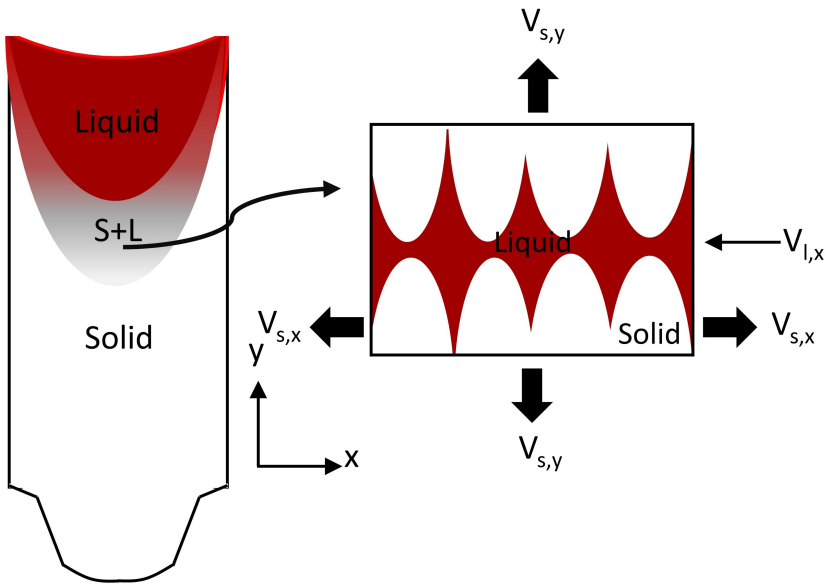

Figure C.1: Schematic of a DC cast billet and a 2-D domain of the semi-solid region.

$$f_l V_{1x} = -\frac{K}{\mu}\frac{dp}{dx}, \tag{C.2}$$

where ρ is the density, V is the velocity , $v_T = \frac{\dot{T}}{G}$ is the growth interface velocity in direction aligned with the thermal gradient, μ is the viscosity, K is the permeability, and P is the melt pressure. The values inside the notation $\langle . \rangle$ are locally averaged over the solid and liquid phases. Therefore, the average density and the average mass flow are defined as $\langle \rho \rangle = \rho_s f_s + \rho_l f_l$ and $\langle \rho V \rangle = \rho_s f_s V_s + \rho_l f_l V_l$, where f_s and f_l are the volume fractions of solid and liquid, respectively. The densities of solid and liquid, i.e. ρ_s and ρ_l are assumed to be constant but not equal. Considering that fluid moves in direction parallel with the thermal gradient and solid deforms in directions perpendicular to and parallel with the thermal gradient, Eq. C.1 is expanded as:

$$\frac{\partial(\rho_l f_l V_{lx})}{\partial x} + \frac{\partial(\rho_s f_s V_{sx})}{\partial x} + \frac{\partial(\rho_s f_s V_{sy})}{\partial y} = v_T \left[\frac{\partial(\rho_s f_s)}{\partial x} + \frac{\partial(\rho_l f_l)}{\partial x} \right], \tag{C.3}$$

where V_{sx} and V_{sy} are the velocity of solid deformation in x and y directions, respectively as shown in Fig. C.1. Assuming that f_s and f_l only vary along the thermal gradient (x direction), Eq. C.3 is rewritten as:

$$\frac{\partial(\rho_l f_l V_{lx})}{\partial x} + (1+\beta)\left[V_{sx}\frac{\partial f_s}{\partial x} + f_s\dot{\varepsilon}_{px} + f_s\dot{\varepsilon}_{py}\right] = v_T\beta\frac{\partial f_s}{\partial x}, \tag{C.4}$$

where $\dot{\varepsilon}_{py}$ and $\dot{\varepsilon}_{py}$ are the strain rates parallel with and perpendicular to the thermal gradient, respectively. The integration of Eq. C.4 over x gives:

$$f_l V_{lx} + (1+\beta)\left[V_{sx}f_s + \int f_s(\dot{\varepsilon}_{px} + \dot{\varepsilon}_{py})dx\right] - v_T\beta f_s = C = -v_T\beta. \tag{C.5}$$

After using Darcy's law to link liquid pressure and velocity, integrating Eq. C.5 from $x_{f_l=f_{lcr}}$ to $x_{f_l=1}$ gives:

$$\Delta P_{cr} = (1+\beta)\mu\int_{f_l=f_{lcr}}^{x_{f_l=1.0}}\frac{1}{K}\left[V_{sx}f_s + \int f_s(\dot{\varepsilon}_{px}+\dot{\varepsilon}_{py})dx\right]dx + v_T\beta\mu\int_{f_l=f_{lcr}}^{x_{f_l=1.0}}\frac{f_l}{K}dx \tag{C.6}$$

where μ is constant throughout the mushy zone and $v_T = \frac{\dot{T}}{G}$ is evaluated at a critical temperature near the solidus. ΔP_{cr} corresponds to the liquid pressure drop between $f_l = 1.0$ and a critical liquid fraction at which liquid feeding ceases (f_{lcr}). Since the temperature gradient, cooling rate, and strain rate are assumed to be constant, the

integration variable of Eq. C.6 can be changed from position to fraction liquid:

$$\Delta P_{cr} = \frac{(1+\beta)\mu}{G}\int_{f_{lcr}}^{1}\frac{1}{K}\left[V_{sx}f_s + \frac{(\dot{\varepsilon}_{px}+\dot{\varepsilon}_{py})}{G}\int_0^{f_{lcr}}(1-f_l)\frac{dT}{df_l}df_l\right]\frac{dT}{df_l}df_l + \frac{\dot{T}\beta\mu}{G^2}\int_{f_{lcr}}^{1}\frac{f_l}{K}\frac{dT}{df_l}df_l. \tag{C.7}$$

Introducing a dimensionless temperature, $\theta = T - T_{sol}/\Delta T_f$, where ΔT_f is the freezing range of the alloy and rearranging Eq. C.7, one finally gets:

$$\Delta P_{cr} = \frac{(1+\beta)\mu\Delta T_f^2(\dot{\varepsilon}_{p_x}+\dot{\varepsilon}_{p_y})}{G^2}I_{de} + \frac{(1+\beta)\mu\Delta T_f\dot{\varepsilon}_{p_x}\lambda_2}{G}I_{sh\dot{\varepsilon}} + \frac{\dot{T}\beta\mu\Delta T_f}{G^2}I_{sh}, \tag{C.8}$$

$$I_{de} = \int_{f_{lcr}}^{l}\left[\frac{1}{K}\int_0^{f_{lcr}}(1-f_l)\frac{d\theta}{df_l}df_l\right]\frac{d\theta}{df_l}df_l, \tag{C.9}$$

$$I_{sh\dot{\varepsilon}} = \int_{f_{lcr}}^{1}\frac{1-f_l}{K}\frac{d\theta}{df_l}df_l, \tag{C.10}$$

$$I_{sh} = \int_{f_{lcr}}^{1}\frac{f_l}{K}\frac{d\theta}{df_l}df_l, \tag{C.11}$$

where I_{de}, I_{sh}, and $I_{sh\dot{\varepsilon}}$ are associated with the term related to deformation, shrinkage, deformation-induced shrinkage, respectively. When fluid flow ceases, mass conservation can be applied to calculate the porosity required to form to feed the remaining shrinkage:

$$f_{p,sh} = \frac{\beta}{\beta+1}f_{lcr}, \tag{C.12}$$

the fraction porosity that forms as a result of deformation in directions parallel and perpendicular to the thermal gradient are defined as:

$$f_{p,de,\varepsilon x} = \frac{\dot{\varepsilon}_{px}\Delta T_f}{\dot{T}} \int_0^{f_{lcr}} (1 - f_l)\frac{d\theta}{df_l} df_l, \tag{C.13}$$

$$f_{p,de,\varepsilon y} = \frac{\dot{\varepsilon}_{py}\Delta T_f}{\dot{T}} \int_0^{f_{lcr}} (1 - f_l)\frac{d\theta}{df_l} df_l, \tag{C.14}$$

finally the strain rate induced shrinkage pore fraction can be calculated as below:

$$f_{p,sh\dot{\varepsilon}} = \frac{G\dot{\varepsilon}_{px}\lambda_2}{\dot{T}}(1 - f_l) = \frac{V_{sx}}{v_T}(1 - f_{lcr}). \tag{C.15}$$

Therefore, the total deformation pore fraction can be computed as:

$$f_{p,sum} = f_{p,sh} + f_{p,sh\dot{\varepsilon}} + f_{p,de,\varepsilon x} + f_{p,de,\varepsilon y} \tag{C.16}$$

Bibliography

[1] Nasim Jamaly, AB Phillion, and J-M Drezet. Stress–strain predictions of semisolid al-mg-mn alloys during direct chill casting: Effects of microstructure and process variables. *Metallurgical and Materials Transactions B*, 44(5):1287–1295, 2013.

[2] M Sistaninia, AB Phillion, J-M Drezet, and M Rappaz. A 3d coupled hydro-mechanical granular model for the prediction of hot tearing formation. In *IOP Conference Series: Materials Science and Engineering*, volume 33, page 012070. IOP Publishing, 2012.

[3] Aluminum Association et al. *Aluminum: properties and physical metallurgy*. ASM international, 1984.

[4] Roger Lumley. *Fundamentals of aluminium metallurgy: production, processing and applications*. Elsevier, 2010.

[5] Myer Kutz. *Materials and Mechanical Design*. John Wiley and Sons, 2006.

[6] Dmitry G Eskin. *Physical metallurgy of direct chill casting of aluminum alloys*. CRC press, 2008.

[7] Zhihao Zhao, Jianzhong Cui, Jie Dong, and Beijiang Zhang. Effect of low-frequency magnetic field on microstructures and macrosegregation of horizontal direct chill casting 7075 aluminum alloy. *Journal of materials processing technology*, 182(1-3):185–190, 2007.

[8] JF Grandfield and PT McGlade. Dc casting of aluminium: process behaviour and technology. In *MATERIALS FORUM-RUSHCUTTERS BAY-*, volume 20, pages 29–51, 1996.

[9] Miha Založnik. *Modeling of macrosegregation in direct chill casting*. PhD thesis, Univerza v Novi Gorici, Fakulteta za podiplomski študij, 2006.

[10] J-M Drezet and M Rappaz. Modeling of ingot distortions during direct chill casting of aluminum alloys. *Metallurgical and Materials Transactions A*, 27(10):3214–3225, 1996.

[11] Etienne JFR Caron, Amir R Baserinia, Harry Ng, Mary A Wells, and David C Weckman. Heat-transfer measurements in the primary cooling phase of the direct-chill casting process. *Metallurgical and Materials Transactions B*, 43(5):1202–1213, 2012.

[12] Robert Vertnik, Miha Založnik, and Božidar Šarler. Solution of transient direct-chill aluminium billet casting problem with simultaneous material and interphase moving boundaries by a meshless method. *Engineering Analysis with Boundary Elements*, 30(10):847–855, 2006.

[13] J Sengupta, SL Cockcroft, DM Maijer, and A Larouche. Quantification of temperature, stress, and strain fields during the start-up phase of direct chill casting

process by using a 3d fully coupled thermal and stress model for aa5182 ingots. *Materials Science and Engineering: A*, 397(1-2):157–177, 2005.

[14] P Pavan Kumar, AK Nallathambi, E Specht, and A Bertram. Mechanical behavior of mushy zone in dc casting using a viscoplastic material model. *Tech. Mech*, 32(2-5):342–357, 2011.

[15] J Sengupta, BG Thomas, and MA Wells. The use of water cooling during the continuous casting of steel and aluminum alloys. *Metallurgical and Materials Transactions A*, 36(1):187–204, 2005.

[16] Ravindra V Tilak, Rodney W Wirtz, and Ronald M Streigle. Apparatus for casting aluminum lithium alloys, July 9 2013. US Patent 8,479,802.

[17] A Chaijaruwanich, PD Lee, RJ Dashwood, YM Youssef, and H Nagaumi. Evolution of pore morphology and distribution during the homogenization of direct chill cast al–mg alloys. *Acta Materialia*, 55(1):285–293, 2007.

[18] PD Lee, RC Atwood, RJ Dashwood, and H Nagaumi. Modeling of porosity formation in direct chill cast aluminum–magnesium alloys. *Materials Science and Engineering: A*, 328(1-2):213–222, 2002.

[19] Miha Založnik and Božidar Šarler. Modeling of macrosegregation in direct-chill casting of aluminum alloys: Estimating the influence of casting parameters. *Materials Science and Engineering: A*, 413:85–91, 2005.

[20] Hervé Combeau, Miha Založnik, and Marie Bedel. Predictive capabilities of multiphysics and multiscale models in modeling solidification of steel ingots and dc casting of aluminum. *Jom*, 68(8):2198–2206, 2016.

[21] Galia Harel, Menachem Bamberger, Y Rami, S Spigarelli, Mohamad El Mehtedi, and Giuseppe Cupitò. Dc casting-simulation and microstructure of mg-zn alloys. In *Materials Science Forum*, volume 638, pages 1518–1523. Trans Tech Publ, 2010.

[22] H Hao, DM Maijer, MA Wells, Andre Phillion, and SL Cockcroft. Modeling the stress-strain behavior and hot tearing during direct chill casting of an az31 magnesium billet. *Metallurgical and materials transactions A*, 41(8):2067–2077, 2010.

[23] M M'hamdi, S Benum, D Mortensen, HG Fjaer, and J-M Drezet. The importance of viscoplastic strain rate in the formation of center cracks during the start-up phase of direct-chill cast aluminum extrusion ingots. *Metallurgical and Materials Transactions A*, 34(9):1941–1952, 2003.

[24] John Campbell. *Castings*. Elsevier, 2003.

[25] Ivar Farup. *Thermally induced deformations and hot tearing during direct chill casting of aluminium*. PhD thesis, University of Oslo, Department of Mathematics, 2000.

[26] P-D Grasso, J-M Drezet, and M Rappaz. Hot tear formation and coalescence observations in organic alloys. Technical report, TMS Publ., 2002.

[27] DG Eskin, L Katgerman, et al. Mechanical properties in the semi-solid state and hot tearing of aluminium alloys. *Progress in materials science*, 49(5):629–711, 2004.

[28] M Kiuchi and R Kopp. Mushy/semi-solid metal forming technology–present and future. *Cirp annals*, 51(2):653–670, 2002.

[29] Mohammed M'Hamdi, Asbjørn Mo, and Christophe L Martin. Two-phase modeling directed toward hot tearing formation in aluminum direct chill casting. *Metallurgical and materials transactions a*, 33(7):2081–2093, 2002.

[30] JF Grandfield, CJ Davidson, and JA Taylor. Light metals 2001, 2001. *The Metals, Minerals and Materials Society*, pages 911–917.

[31] TW Clyne and GJ Davies. Influence of composition on solidification cracking susceptibility in binary alloy systems. *British Foundryman*, 74:65–73, 1981.

[32] M Rappaz, I Farup, and J-M Drezet. Study and modeling of hot tearing formation. Technical report, 2000.

[33] Brian G Thomas and Michel Bellet. Modeling of stress, distortion, and hot tearing, 2008.

[34] F Körber and G Schitzkowski. Determination of the contraction of cast steel. *Stahl Und Eisen*, 15:128–135, 1928.

[35] S Li and D Apelian. Hot tearing of aluminum alloys. *International Journal of Metalcasting*, 5(1):23–40, 2011.

[36] J Verö. The hot-shortness of aluminum alloys. *The Metals Industry*, 48:431–434, 1936.

[37] WI Pumphrey. A consideration of the nature of brittleness at temperatures above

the solidus in castings and welds in aluminium alloys. *J. of the Inst. of Metals*, 75:235–256, 1948.

[38] WS Pellini. Strain theory of hot tearing. *Foundry*, 80(11):125–133, 1952.

[39] RA Rosenberg, MC Flemings, and HF Taylor. Nonferrous binary alloys hot tearing. *AFS Trans*, 69:518–528, 1960.

[40] E Niyama. Japan-us joint seminar on solidification of metals and alloys. *Tokyo (Japan Society for Promotion of Science)*, pages 271–282, 1977.

[41] U Feurer. Quality control of engineering alloys and the role of metals science. *Delft University of Technology, Delft, The Netherlands*, pages 131–45, 1977.

[42] NN Prokhorov. Resistance to hot tearing of cast metals during solidification. *Russian castings production*, 2(2):172–175, 1962.

[43] Hasse Fredriksson, Mohsen Haddad-Sabzevar, K Hansson, and Jani Kron. Theory of hot crack formation. *Materials science and technology*, 21(5):521–530, 2005.

[44] M Haddad-Sabzevar and H Fredriksson. Rapidly solidified ribbons of fe 2c 13cr 1si mo alloys produced by the planar flow melt spinning process. *Materials Science and Engineering: A*, 173(1-2):401–405, 1993.

[45] Guo-ping Cao and Sin-do Kou. Hot cracking of binary mg–al alloy castings. *Materials Science and Engineering: A*, 417(1-2):230–238, 2006.

[46] Benoît Commet and André Larouche. An integrated approach to control hot tearing in sheet ingot casting. *Light Metals. TMS*, 152, 2006.

[47] D Warrington and DG McCartney. Hot-cracking in aluminium alloys 7050 and 7010—a comparative study. *Cast metals*, 3(4):202–208, 1990.

[48] John F Grandfield, Cameron J Davidson, and John A Taylor. The columnar to equiaxed transition in horizontal direct chill cast magnesium alloy az91. *Continuous Casting*, pages 245–250, 2000.

[49] WI Pumphrey and JV Lyons. Cracking during the casting and welding of the more common binary aluminium alloys. *Journal of the Institute of Metals*, 74(9):439, 1948.

[50] G Upadhya, S Cheng, and U Chandra. A mathematical model for prediction of hot tears in castings. *Light Metals 1995, Las Vegas NV, USA*, 12(16), 1995.

[51] John Campbell. *Complete casting handbook: metal casting processes, metallurgy, techniques and design*. Butterworth-Heinemann, 2015.

[52] Mark Easton, John F Grandfield, David H StJohn, and Barbara Rinderer. The effect of grain refinement and cooling rate on the hot tearing of wrought aluminium alloys. In *Materials science forum*, volume 519, pages 1675–1680. Trans Tech Publ, 2006.

[53] WH Kool, Laurens Katgerman, et al. Micro-mechanical model of hot tearing at triple junctions in dc casting. In *Materials Science Forum*, volume 396, pages 179–184. Trans Tech Publications Ltd., Zurich-Uetikon, Switzerland, 2002.

[54] Charles Willers Briggs. *The metallurgy of steel castings*. McGraw-Hill book Company, Incorporated, 1946.

[55] J-M Drezet, M Rappaz, G-U Grün, and M Gremaud. Determination of thermophysical properties and boundary conditions of direct chill-cast aluminum alloys using inverse methods. *Metallurgical and Materials Transactions A*, 31(6):1627–1634, 2000.

[56] XW Zheng, J Dong, N Zhou, PH Fu, SS Yao, and WJ Ding. Effect of process parameters on structure and macrosegregation upon direct chill casting of mg–nd–zn–zr alloy. *Materials Science and Technology*, 27(1):275–281, 2011.

[57] TW Clyne and GJ Davies. Comparison between experimental data and theoretical predictions relating to dependence of solidification cracking on composition. In *Solidification and Casting of Metals\ Proc. Conf.\, Sheffield, England, July 1977,*, pages 275–278, 1979.

[58] L Katgerman. A mathematical model for hot cracking of aluminum alloys during dc casting. *JOM*, 34(2):46–49, 1982.

[59] Ilya I Novikov. Hot-shortness of nonferrous metals and alloys. 1968.

[60] M Rappaz, J-M Drezet, and Met Gremaud. A new hot-tearing criterion. *Metallurgical and materials transactions A*, 30(2):449–455, 1999.

[61] J Ampuero, Ch Charbon, AFA Hoadley, M Rappaz, VR Voller, MS Stachowicz, and BG Thomas. Modeling of microporosity evolution during the solidification of metallic alloys. Technical report, TMS Publ., 1991.

[62] Charles Monroe and Christoph Beckermann. Prediction of hot tearing using a dimensionless niyama criterion. *Jom*, 66(8):1439–1445, 2014.

[63] Kent D Carlson and Christoph Beckermann. Prediction of shrinkage pore volume fraction using a dimensionless niyama criterion. *Metallurgical and Materials Transactions A*, 40(1):163–175, 2009.

[64] E Niyama. A method of shrinkage prediction and its application to steel casting practice. *Imono*, 54(8):507–517, 1982.

[65] Stéphane Vernede, Philippe Jarry, and Michel Rappaz. A granular model of equiaxed mushy zones: Formation of a coherent solid and localization of feeding. *Acta Materialia*, 54(15):4023–4034, 2006.

[66] M Rappaz. Modeling and characterization of grain structures and defects in solidification. *Current Opinion in Solid State and Materials Science*, 20(1):37–45, 2016.

[67] DJ Lahaie and M Bouchard. Physical modeling of the deformation mechanisms of semisolid bodies and a mechanical criterion for hot tearing. *Metallurgical and materials Transactions B*, 32(4):697–705, 2001.

[68] Stéphane Vernède, Jonathan A Dantzig, and Michel Rappaz. A mesoscale granular model for the mechanical behavior of alloys during solidification. *Acta Materialia*, 57(5):1554–1569, 2009.

[69] J-M Drezet, M Sistaninia, and M Rappaz. Modeling of hot tearing: two-phase models, coalescence and mesoscale granular models. *Matériaux & Techniques*, 98(4):261–267, 2010.

[70] M Sistaninia, AB Phillion, J-M Drezet, and M Rappaz. Three-dimensional granular model of semi-solid metallic alloys undergoing solidification: Fluid flow and localization of feeding. *Acta materialia*, 60(9):3902–3911, 2012.

[71] Sofiane Terzi, Luc Salvo, Michel Suéry, Nathalie Limodin, Jérôme Adrien, E Maire, Y Pannier, Michel Bornert, Dominique Bernard, M Felberbaum, et al. In situ x-ray tomography observation of inhomogeneous deformation in semi-solid aluminium alloys. *Scripta Materialia*, 61(5):449–452, 2009.

[72] Andre Phillion. *Hot tearing predictions in direct chill cast aluminum AA5182 ingots*. PhD thesis, University of British Columbia, 2004.

[73] Savran VI Suyitno, VI Savran, and L Katgerman. Effects of alloy composition and casting speed on structure formation and hot tearing during direct-chill casting of al-cu alloys. *Metallurgical and Materials Transactions A*, 35(11):3551–3561, 2004.

[74] M Sistaninia, AB Phillion, J-M Drezet, and M Rappaz. A 3-d coupled hydromechanical granular model for simulating the constitutive behavior of metallic alloys during solidification. *Acta Materialia*, 60(19):6793–6803, 2012.

[75] J-M Drezet and AB Phillion. As-cast residual stresses in an aluminum alloy aa6063 billet: neutron diffraction measurements and finite element modeling. *Metallurgical and Materials Transactions A*, 41(13):3396–3404, 2010.

[76] Meisam Sistaninia, AB Phillion, J-M Drezet, and Michel Rappaz. Simulation of semi-solid material mechanical behavior using a combined discrete/finite element method. *Metallurgical and Materials Transactions A*, 42(1):239–248, 2011.

[77] M Sistaninia, S Terzi, AB Phillion, J-M Drezet, and M Rappaz. 3-d granular modeling and in situ x-ray tomographic imaging: a comparative study of hot tearing formation and semi-solid deformation in al–cu alloys. *Acta Materialia*, 61(10):3831–3841, 2013.

[78] S Thompson, SL Cockcroft, and MA Wells. Effect of cooling rate on solidification characteristics of aluminium alloy aa 5182. *Materials science and technology*, 20(4):497–504, 2004.

[79] Lucio F Mondolfo. *Aluminum alloys: structure and properties*. Elsevier, 2013.

[80] Alankar Alankar and Mary A Wells. Constitutive behavior of as-cast aluminum alloys aa3104, aa5182 and aa6111 at below solidus temperatures. *Materials Science and Engineering: A*, 527(29-30):7812–7820, 2010.

[81] AB Phillion, SL Cockcroft, and PD Lee. Predicting the constitutive behavior of semi-solids via a direct finite element simulation: application to aa5182. *Modelling and Simulation in Materials science and Engineering*, 17(5):055011, 2009.

[82] Mark Alan Easton and David H StJohn. Improved prediction of the grain size of aluminum alloys that includes the effect of cooling rate. *Materials Science and Engineering: A*, 486(1-2):8–13, 2008.

[83] Mats Johnsson and L Bäckerud. The influence of composition on equiaxed crystal growth mechanisms and grain size in al alloys. *Zeitschrift fur Metallkunde*, 87(3):216–220, 1996.

[84] AB Phillion, J-L Desbiolles, and M Rappaz. A 3d granular model of equiaxed-granular solidification. Technical report, Minerals, Metals & Materials Soc, 184 Thorn Hill Rd, Warrendale, Pa 15086 ..., 2009.

[85] M Rappaz, A Jacot, and William J Boettinger. Last-stage solidification of alloys: theoretical model of dendrite-arm and grain coalescence. *Metallurgical and Materials Transactions A*, 34(3):467–479, 2003.

[86] V Mathier, S Vernede, P Jarry, and M Rappaz. Two-phase modeling of hot tearing in aluminum alloys: applications of a semicoupled method. *Metallurgical and Materials Transactions A*, 40(4):943, 2009.

[87] Olivier Ludwig, J-M Drezet, P Ménésès, CL Martin, and Michel Suéry. Rheological behavior of a commercial aa5182 aluminum alloy during solidification. *Materials Science and Engineering: A*, 413:174–179, 2005.

[88] Martin Syvertsen. Oxide skin strength on molten aluminum. *Metallurgical and Materials Transactions B*, 37(3):495–504, 2006.

[89] Ruifeng Dou and AB Phillion. Application of a pore fraction hot tearing model to directionally solidified and direct chill cast aluminum alloys. *Metallurgical and Materials Transactions A*, 47(8):4217–4225, 2016.

[90] Philip Crosbie Carman. Fluid flow through granular beds. *Trans. Inst. Chem. Eng.*, 15:150–166, 1937.